

**GMTSAR:**  
**An InSAR Processing System**  
**Based on Generic Mapping Tools**  
(Second Edition)

David Sandwell\*      Rob Mellors<sup>†</sup>      Xiaopeng Tong<sup>\*‡</sup>  
Xiaohua Xu\*      Matt Wei<sup>§</sup>      Paul Wessel<sup>¶</sup>

May 1, 2011; Revised: June 1, 2016

---

\*Scripps Institution of Oceanography, University of California, San Diego, La Jolla, CA

<sup>†</sup>Lawrence Livermore National Laboratory, Livermore, CA

<sup>‡</sup>Department of Earth and Space Sciences, University of Washington, Seattle, WA

<sup>§</sup>Graduate School of Oceanography, University of Rhode Island, Narragansett, RI

<sup>¶</sup>Department of Geology and Geophysics, University of Hawaii at Manoa, HI

# Contents

<b>1</b>	<b>Introduction</b>	<b>5</b>
1.1	Objectives and limitations of GMTSAR . . . . .	5
1.2	Algorithms: SAR, InSAR, and the need for precise orbits . . . . .	6
1.2.1	Proper focus . . . . .	7
1.2.2	Transformation from geographic to radar coordinates . . . . .	8
1.2.3	Image alignment . . . . .	9
1.2.4	Flattening interferogram - no trend removal . . . . .	10
<b>2</b>	<b>Software</b>	<b>11</b>
2.1	Standard Products . . . . .	11
2.2	Software Design . . . . .	12
<b>3</b>	<b>Processing Examples</b>	<b>14</b>
3.1	Two-pass processing . . . . .	15
3.2	Stacking for time series . . . . .	18
3.3	ScanSAR Interferometry . . . . .	26
<b>4</b>	<b>Problems</b>	<b>32</b>
<b>A</b>	<b>Principles of Synthetic Aperture Radar</b>	<b>33</b>
A.1	Introduction . . . . .	33
A.2	Fraunhofer diffraction . . . . .	34
A.3	2-D Aperture . . . . .	37
A.4	Range resolution (end view) . . . . .	38
A.5	Azimuth resolution (top view) . . . . .	39
A.6	Range and Azimuth Resolution of ERS SAR . . . . .	40
A.7	Pulse repetition frequency . . . . .	40
A.8	Other constraints on the PRF . . . . .	40
A.9	Problems . . . . .	42
<b>B</b>	<b>SAR Image Formation</b>	<b>44</b>
B.1	Overview of the range-doppler algorithm . . . . .	44
B.2	Processing on board the satellite . . . . .	44
B.3	Digital SAR processing . . . . .	45
B.4	Range compression . . . . .	49
B.5	Azimuth compression . . . . .	51
B.6	Example with ALOS L-band orbit . . . . .	58
B.7	Problems . . . . .	61
<b>C</b>	<b>InSAR</b>	<b>62</b>
C.1	Forming an interferogram . . . . .	62
C.2	Contributions to Phase . . . . .	63
C.3	Phase due to earth curvature . . . . .	64
C.4	Look angle and incidence angle for a spherical earth . . . . .	65
C.5	Critical baseline . . . . .	67

C.6	Persistent point scatterer and critical baseline . . . . .	68
C.7	Phase due to topography . . . . .	69
C.8	Altitude of ambiguity . . . . .	70
C.9	Phase due to earth curvature and topography – exact formula . . . . .	70
C.10	Problems . . . . .	74
<b>D</b>	<b>ScanSAR Processing and Interferometry</b>	<b>75</b>
D.1	Problems . . . . .	80
<b>E</b>	<b>Sentinel TOPS-mode processing and interferometry</b>	<b>81</b>
E.1	Introduction . . . . .	81
E.2	Traditional Image Alignment Fails with TOPS-Mode Data . . . . .	83
E.3	Geometric Image Registration . . . . .	84
E.4	Enhanced Spectral Diversity . . . . .	86
E.5	Elevation Antenna Pattern (EAP) Correction (IPF version change) . . . . .	87
E.6	Examples of TOPS Interferogram processing . . . . .	87
E.7	Processing setup and commands: . . . . .	97
E.8	Problems . . . . .	99
<b>F</b>	<b>Geolocation accuracy for Pinon corner reflectors</b>	<b>100</b>
<b>G</b>	<b>Installation of GMTSAR</b>	<b>107</b>

## Preface to Second Edition

This technical report provides an update to the original GMTSAR report published in 2011. The significant changes to the software and documentation include:

- preprocessors for new data types including TerraSAR-X, COSMO-SkyMed, Radarsat-2, ALOS-2, and Sentinel-1;
- the addition of a coherence-based SBAS time series program;
- full integration of GMTSAR with GMT5;
- geometric image alignment based only on orbits and topography; and
- full support for Sentinel-1 TOPS-mode data.

The addition of the TOPS-mode processing involved a refinement of the algorithm for transforming between geographic and radar coordinates that is now accurate to a few centimeters. Pure geometric image alignment of all slaves to a single master enables a whole new approach to data preparation for InSAR time series. GMTSAR is still focussed on the basic aspects of InSAR processing to prepare large stacks of images for more advanced time series method such as persistent scatterer analysis. We have avoided constructing tools that can hide fundamental limitations in the data or software (e.g., *baseline re-estimation*). Our objective is to keep the core software small and only dependent on Generic Mapping Tools. GMTSAR also uses a published phase unwrapping code called *Snaphu* (Chen and Zebker 2000). The user can use GMT or other packages for post processing (e.g., combining InSAR with GPS point data). This software is completely open under a GNU General Public License so users should feel free to modify and redistribute codes. The best way to learn to use GMTSAR is to install it and run the test examples. In addition, for the past several years we have offered a short course sponsored by UNAVCO. The instructional material is posted at the UNAVCO short course site.

# 1 Introduction

GMTSAR is an open source (GNU General Public License) InSAR processing system designed for users familiar with Generic Mapping Tools (GMT). The code is written in C and will compile on any computer where GMT and NETCDF are installed. The system has three main components: 1) a preprocessor for each satellite data type to convert the native format and orbital information into a generic format; 2) an InSAR processor to focus and align stacks of images, map topography into phase, and form the complex interferogram; 3) a postprocessor, mostly based on GMT, to filter the interferogram and construct interferometric products of phase, coherence, phase gradient, and line-of-sight displacement in both radar and geographic coordinates. GMT is used to display all the products as postscript files and kml-images for Google Earth. A set of C-shell scripts has been developed for standard 2-pass processing as well as image alignment for stacking and time series. Users are welcome to contribute to this effort.

GMTSAR differs from other InSAR systems such as ROI\_PAC, Gamma, and DORIS because it relies on sub-meter orbital accuracy to greatly simplify the SAR and InSAR processing algorithms. Moreover large batches of SAR images can be automatically processed with no human intervention. The down side of this approach is that SAR satellites having less accurate orbits ( $> 10$  m, e.g., RADARSAT-1 and JERS-1) cannot be easily processed using GMTSAR. Reliance on precise orbits also greatly simplifies the code so only 5 essential programs (*llt2rat*, *esarp*, *xcorr*, *phasediff*, *conv*) are needed beyond the GMT package. Moreover, geometric and phase accuracy ensures that mosaics of many frames along a long swath or combinations of ScanSAR subswaths will abut seamlessly in geographic coordinates. This document contains three main sections and 7 appendices. Section 1 is an introduction to GMTSAR and the geometric model used to create SAR and InSAR products without using ground control or applying orbital adjustments. Section 2 is a description of the overall software design as well as the standard output products. Section 3 provides recipes for the most common types of InSAR processing including 2-pass InSAR, stacking/time series, and ScanSAR interferometry. Appendix A is an overview of principles of SAR processing. Appendix B is a detailed description of the range-Doppler SAR processor and the parameter file. Appendix C provides the theory for InSAR processing on a spherical Earth with no approximations. Appendix D describes the algorithm that we use for ALOS-1 ScanSAR interferometry. Appendix E describes the geometric image alignment algorithms developed for the TOPS-mode data from Sentinel-1. Appendix F provides data on the geolocation accuracy of SAR imagery. Appendix G provides instructions for installation and testing the GMTSAR package.

## 1.1 Objectives and limitations of GMTSAR

Creating synthetic aperture radar (SAR) images and interferograms (InSAR) from satellite radar measurements requires specialized front-end computer codes for focusing imagery and computing interferometric phase. However, much of the back-end processing and display can be accomplished with existing generic codes. We have developed a SAR/InSAR processing system that starts with raw (or SLC) SAR data in radar coordinates, along with precise orbital information, and computes interferomet-

ric products in geographic coordinates. Our design goals are to have a modular and portable system based on a minimum set of new software. The system relies on precise orbital information, as discussed below, and a consistent geometric model to achieve proper focus and image alignment. The SAR processor code was originally derived from the Stanford/JPL FORTRAN and re-written in the C programming language ensuring compilation on many platforms using the standard *gcc* compiler. The remainder of the front-end code has been developed and refined over the past decade as part of the SIOSAR and ALOS\_preprocess packages.

For the back-end processing we use the Generic Mapping Tools (GMT), which is an open source collection of programs designed for manipulating and displaying geographic data sets (Wessel and Smith 1998; Wessel, Smith, et al. 2013). It is widely used among the geophysical community, well documented, and continuously updated. GMT includes efficient and robust programs for regridding, filtering, and trend removal, which makes it highly useful for some aspects of InSAR processing. GMT uses the NETCDF file format that allows the exchange of files among computers having different architectures. The combined front- and back-end processing is done using the c-shell scripting language which is available on all UNIX platforms. We encourage the development of new modules and InSAR processing recipes from the broader InSAR community. The GMTSAR package also includes the capability for ScanSAR processing and is flexible enough for performing time series analysis on stacks of interferograms.

## 1.2 Algorithms: SAR, InSAR, and the need for precise orbits

Synthetic aperture radar (SAR) satellites collect swaths of side-looking echoes at a sufficiently high range resolution and along-track sampling rate to form high resolution imagery (Appendix A). The range resolution of the raw radar data is determined by the pulse length (or  $1/\text{bandwidth}$ ) and the *incidence angle*; a typical range resolution is 20 m. For real aperture radar, the along-track or *azimuth* resolution of the outgoing microwave pulse is diffraction limited to an angle corresponding to the wavelength of the radar (e.g. 0.05 m) divided by the length of the aperture (e.g. 10 m). When this beam pattern is projected onto the surface of the earth at a range of say 850 km, it illuminates 4250 m in the along-track dimension so the raw radar data are horribly out of focus in azimuth. Using the synthetic aperture method, the image can be focused on a point reflector on the ground by coherently summing thousands of consecutive echoes thus creating a synthetic aperture perhaps 4250 m long. Proper focus is achieved by summing the complex numbers along a constant range. The focused image contains both amplitude (backscatter) and phase (range) information for each pixel. In GMT-SAR, the SAR processor computer code is called *esarp*; proper focus relies on having an accurate orbital trajectory for the satellite (Appendix B). For example the image will be out of focus if the range between the antenna and reflector has an error greater than about  $1/4$  wavelength (e.g. 0.01 m) over a distance of the synthetic aperture (4250 m).

A complex radar interferogram (InSAR) is created by multiplying the reference image by the complex conjugate of the repeat image (Appendix C). For the ideal case where the trajectories of the reference and repeat images are exactly coincident, the phase difference between the two images will reflect differences in range between the

antenna and a target pixel. This could be due to line-of-sight motion of the target pixel or a travel time change due to the atmosphere or ionosphere. Normally there is an offset between the trajectories of the reference and repeat orbits. In this case the phase of the complex interferogram has an additional component due to the shape of the earth. The corrections for the curvature and topography of the earth are combined into one formula in the code *phasediff* (Appendix C). This topographic phase can be removed from the interferogram if independent topography information is available (e.g., SRTM (Farr et al. 2004)). An accurate orbit is needed to project the topography model from a latitude, longitude, and ellipsoidal height coordinate system into the range and azimuth coordinates of the radar image. An accurate orbit is also needed to correct the phase of the repeat image for the non-zero interferometric baseline since orbital error maps directly into interferometric phase. The GMTSAR software will only provide reliable output for interferometric satellites where precise orbital information (<1 m precision) is available. Today this includes (ERS-1, ERS-2, Envisat, ALOS-1, and TerraSAR-X, COSMO-SkyMed, Radarsat-2, ALOS-2, and Sentinel-1). Note that Radarsat-1 and JERS-1 cannot be easily processed with this software because their orbits are not accurate enough. The precise orbital information is used in 4 aspects of the InSAR processing discussed in the following text and is the key to robust and efficient software.

### 1.2.1 Proper focus

First proper focus of the SAR image involves the coherent summation of range-aligned echoes over the length of the synthetic aperture as shown in Figure 1. Therefore we need to calculate the range as a function of slow time  $s$ . First consider the case of a straight line orbit passing over a fixed point reflector. The range to the reflector would vary as a hyperbola with slow time. In the actual case the orbital path is elliptical and the earth is rotating so the range versus time function is a more complicated function. However, because the synthetic aperture is short (<5 km) compared with the nominal range from the satellite to the reflector ( 800 km), a 3-parameter parabolic approximation is commonly used to model range versus time (Curlander and McDonough 1991, Appendix B).

$$R(s) = R_o + \dot{R}(s - s_o) + \frac{\ddot{R}}{2}(s - s_o)^2 + \dots \quad (1)$$

where  $R_o$  is the closest approach of the spacecraft to the point reflector and  $s_o$  is the time of closest approach. These three parameters  $R_o$ ,  $\dot{R}$ , and  $\ddot{R}$  are needed to focus an image (Appendix B). In terms of the SAR processor, these are called the near range  $R_o$ , the Doppler centroid  $f_{DC}$  and the Doppler frequency rate  $f_R$  which are related to the coefficients of this polynomial

$$f_{DC} = \frac{-2\dot{R}}{\lambda} \quad \text{and} \quad f_R = \frac{-2\ddot{R}}{\lambda}, \quad (2)$$

where  $\lambda$  is the wavelength of the radar. When a SAR image is focused at zero Doppler, the range rate at position  $s_o$  is by definition zero.

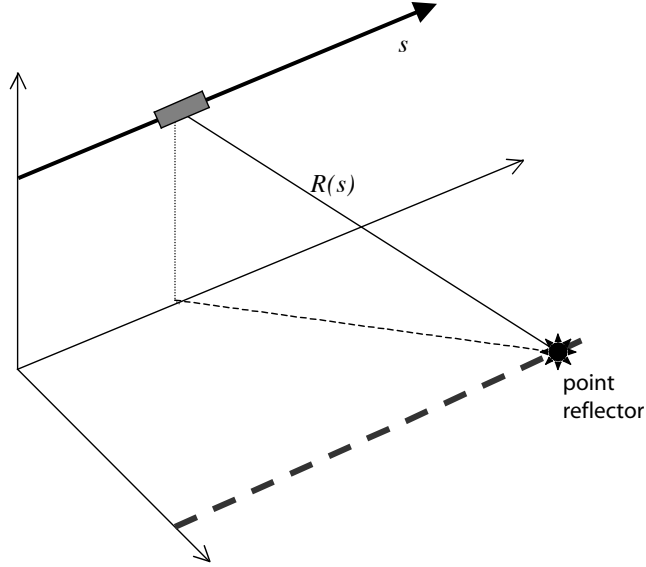


Figure 1: Geometry of SAR antenna flying over a point reflector on the ground. The range  $R$  varies with slow time  $s$  as measured by the precise orbit provided in an earth-fixed coordinate system.

### 1.2.2 Transformation from geographic to radar coordinates

The second use of precise orbital information is to map every point on the surface of the earth (lon, lat, topography) into the range and azimuth coordinates of the radar. This mapping provides a lookup table for transforming between geographic and radar coordinates. The algorithm for creating this mapping is conceptually simple but can be computationally expensive. The precise orbital information is used to determine the range from the satellite to a topography grid cell. The time of the minimum range is found using a Golden section search algorithm (Press et al. 1992). A second order polynomial is fit to this range versus time function about the time of minimum range (equation (1)). If the SAR image is focused at zero Doppler then the range coordinate of the mapping is simply the minimum range and the azimuth coordinate is the time of the minimum range. Of course, by definition the range-rate, or Doppler, is zero at this azimuth position. If the radar image was focused at a Doppler centroid other than zero then equation (2) can be used to calculate the non-zero range-rate at this Doppler.

$$\dot{R} = -\frac{\lambda f_{DC}}{2} \quad (3)$$

Next by taking the derivative of the parabolic approximation one can determine the along-track time shift that will be produced by focusing at a non-zero Doppler. This is

given by

$$\Delta s = -\frac{\lambda f_{DC}}{2\dot{R}} \quad (4)$$

The corresponding range correction is given by

$$\Delta R = \frac{\dot{R}}{2} \Delta s^2. \quad (5)$$

This mapping from earth to radar coordinates described in equations 1-5 is perhaps the only really new aspect of GMTSAR and it allows a large simplification of the front-end processing code with respect to a more tolerant package such as ROI.PAC.

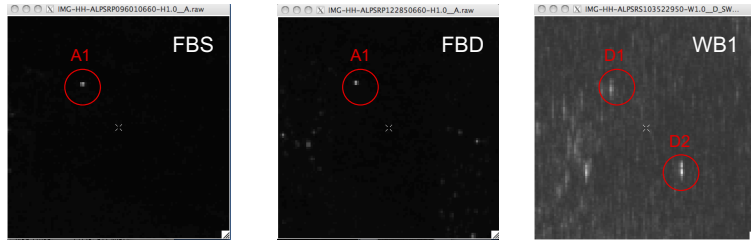
These two corrections are needed in the transformation from geographic to radar coordinates when the image is focussed at a Doppler other than zero. The accuracy of this approach where no ground control points are used has been determined using corner reflectors at Pinon Flat Observatory (Table 1). We have verified the accuracy of our approach using raw and SLC SAR imagery from a variety of satellite radars and modes (Table 2 and Appendix F). The L-band results show a systematic range bias perhaps related to the ionosphere and troposphere delays (i.e., the dry troposphere should be -5.8 m). The rms variation is typically 6 m in range and 4 m in azimuth. For the ScanSAR data the azimuth positions are 5 times less accurate due to the lower sampling density in each of the 5 subswaths. Since the highest resolution global topography data for the Earth has a pixel size of 30 m, the mapping from lon, lat, topography into the range, azimuth, and topographic phase can be applied to non-zero baseline interferograms without any positional or phase adjustments. This provides a great simplification to the code because the topographic phase does not need to be spatially warped to match the master image of the interferogram. Although in some cases a range shift of up to one pixel is needed to account for the propagation delay through the atmosphere and ionosphere.

Position			Orientation	
<i>lat</i>	<i>lon</i>	<i>height</i>	<i>elev.</i>	<i>azi.</i>
33.612246	-116.456768	1258.990	39°	257.5°
33.612253	-116.457893	1257.544	39°	102.5°
33.607373	-116.451836	1254.537	39°	102.5°

Table 1: Coordinates of Radar Reflectors. Latitude and longitude in decimal degrees and height in meters relative to the WGS-84 co-ordinate system and ellipsoid. The survey point is the apex (lowest corner) of each reflector. There should be a correction for the offset between the phase center of the reflector and the apex.

### 1.2.3 Image alignment

The third use of the precise orbital information is to align the reference and repeat image to sub-pixel accuracy in order to form the interferogram. The corner reflector



	<b>FBS</b>	<b>FBD</b>	<b>WB1</b>
$N$	18	9	8
<i>Ground-range</i>	$-11.5 \pm 5.5$ m	$-14.9 \pm 5.8$ m	$-5.6 \pm 8.4$ m
<i>Azimuth</i>	$1.3 \pm 3.7$ m	$2.4 \pm 4.2$ m	$-9.55 \pm 18.3$ m

Table 2: Comparison between the position of radar corner reflectors predicted from ALOS orbital data and position seen in 35 focused SAR images. Three types of ALOS PALSAR data were used - fine beam single polarization (FBS), fine beam dual polarization (FBD) and 5-subswath ScanSAR (WB1). The mean and rms differences are consistent with all the error being due to propagation delays. The rms differences are consistent with point reflector resolution of the imagery. Orbital errors are probably much less than 1 meter.

analysis above suggests that the geolocation based on the satellite orbit is only accurate to about 2 pixels in range and 1 pixel in azimuth so it is not accurate enough for subpixel image registration. Nevertheless this accuracy provides a very good starting point for a 2-dimensional image cross correlation algorithm (*xcorr*). Indeed our software *xcorr*, described below, uses a search window size of 64 pixels and has never failed to provide accurate co-registration even in cases where the interferometric coherence is close to zero.

#### 1.2.4 Flattening interferogram - no trend removal

The fourth use of the precise orbit is for calculating the parallel and perpendicular components of the interferometric baseline that are needed for removing the interferometric phase for the range differences to every pixel in the image. This correction depends on both the orbital trajectory and the shape of the earth including the ellipsoidal, geoidal, and topographic components given in Appendix C. Another unique aspect of

GMTSAR is that interferograms for long swaths of data can be calculated on a frame-by-frame basis and seamlessly reassembled in geographic co-ordinates. This is only possible because the baselines, orbital heights, and topographic data are all seamless at the frame boundaries. This seamless recombination of interferograms requires that the user select a common earth radius and near range for the entire swath in the file *configure.txt*. This feature is especially useful for ScanSAR-to-ScanSAR interferometry because each of the ScanSAR subswaths can be processed independently at their original azimuth sampling rate (i.e. PRF) and then re-assembled in geographic coordinates without adjustment. Frame-by-frame processing also has an advantage because the file size of one complex SAR image and its interferometric products can be far less than the 2 Gbyte file limit on 32-bit computers. Secondly, one can easily take advantage of multiple processors that are available on many computers to process multiple frames of interferometric products simultaneously, without having to rewrite any computer code.

## 2 Software

### 2.1 Standard Products

Before introducing the main software components it is useful to describe the standard products created by the GMTSAR system using the script *p2p\_SAT.csh*.

*name.PRM* Ascii file generated by the pre-processing software. It contains all the information needed to focus and align a single look complex (SLC) image with a master image. This file contains all the important SAR and InSAR processing parameters and is more completely described in Appendix B.

*name.LED* Ascii file generated by the pre-processing software to contain the orbital information as a state vector.

*name.raw* File contains the raw signal data. Each row of signal data has a 412 byte header record containing timing and other information followed by the radar echo stored as unsigned 2-byte complex numbers (1 byte real and 1 byte imaginary).

*name.SLC* File contains the focused single look complex (SLC) image. The signed 4-byte complex numbers are stored as unsigned short integers (2-bytes real and 2-bytes imaginary). The numbers are scaled to utilize the full dynamic range of a short integer. (An 8-byte complex output option is also provided by the SAR processor.)

*trans.dat* File contains the mapping between range, azimuth coordinates and longitude, latitude, topography coordinates. The topography is calculated with respect to a local spherical approximation to the earth (Appendix C) and therefore large negative and positive numbers are possible.

The format is: range azimuth topography longitude latitude and numbers are stored as double precision floating point.

11301.587587 18451.999997 -272.883315 -115.156667 32.373333  
11308.909450 18451.999997 -273.413527 -115.156111 32.373333

*topo\_ra.grd* Grid of range, azimuth, and topography.

*real.grd* or *imag.grd* Grids of range, azimuth, and the real or imaginary part of the complex interferogram (files are deleted when no longer needed).

*phase.grd* Grid of range, azimuth, and interferometric phase modulus  $2\pi$ .

*corr.grd* Grid of range, azimuth, and interferometric coherence (0-1).

*xphase.grd* Grid of range, azimuth, and phase gradient in the range direction in units of radians per pixel (optional).

*yphase.grd* Grid of range, azimuth, and phase gradient in the azimuth direction in units of radians per pixel (optional).

*mask.grd* Grid of range, azimuth, and NaN or 1. NaN signifies data should be masked.

*unwrap.grd* Grid of unwrapped interferometric phase in radians (optional).

All the files with suffix *.grd* are in NetCDF format. When the interferometric products have been transformed back to geographic coordinates the file names include an *.ll*. For example, *phase.ll.grd* is a netcdf file of longitude, latitude, and interferometric phase modulus  $2\pi$ .

Files having a *.ps* suffix are postscript plots of the quantity. For example, *phase\_mask.ll.ps* is a postscript plot of masked phase in geographic coordinates.

Files having a *.kml/png* suffix are Google Earth images. For example, *phase\_mask.ll.kml/png* is a Google Earth image of masked phase in geographic coordinates.

(Note that the GMT command `grd2xyz phase.grd -Zf > phase` will produce a flat file of floats with a size of  $4 * nrow * ncol$  bytes.)

## 2.2 Software Design

The overall design of the software is illustrated in Figure 2. There is a set of preprocessing code for each of the satellites. Example data sets are available at <http://topex.ucsd.edu/gmtsar>. Data, leader, and orbit files provided by the space agency are normally in CEOS format and are converted into generic *\*.raw* and *\*.PRM* files. The pre-processing code checks for missing lines in the CEOS data file and aligns the radar echoes on a common near range or sample window start time (SWST). The output is a raw file (*\*.raw*) that is ready to be focused in the SAR processor. The relevant parameters are extracted from the various leader and orbit files and used to prepare a parameter file (*\*.PRM*) as fully described in Appendix B. After selecting the master image, a user-supplied topography grid of the area (*dem.grd*) is projected into radar coordinates to create a transformation file (*trans.dat*).

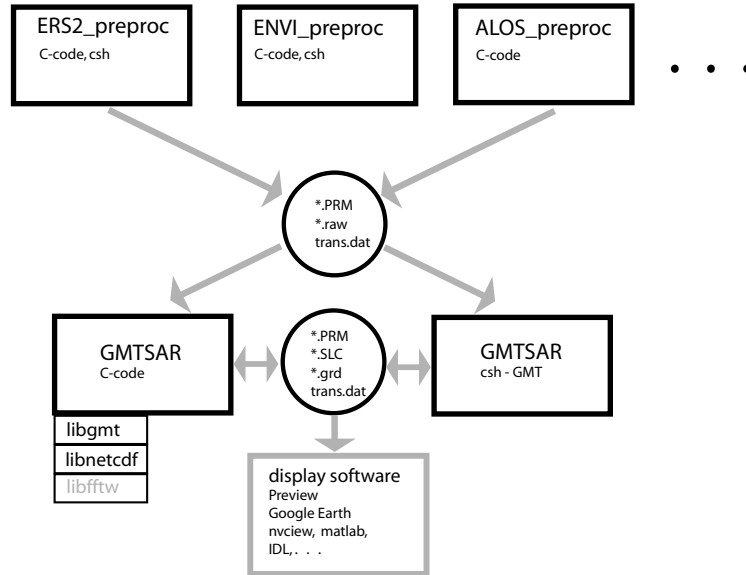


Figure 2: Design of GMTSAR and preprocessors.

The GMTSAR code is the same for all the satellite data types. There are 4 essential programs written in C called *esarp*, *xcorr*, *phasediff*, *conv*. The programs *esarp* and *xcorr* make extensive use of a 1-dimensional fast fourier transform (FFT) routine built into GMT. In the original GMTSAR codes, the user needed to select the most appropriate FFT code for optimal performance. That task is now done automatically during the installation of GMT5. The three options are: the default option uses FFT routines from *fftpack.c* code (Swarztrauber 1982); the fastest option uses the Accelerate Framework included in the Mac OS X system; the third option uses the *fftw* code that is distributed by <http://www.fftw.org/>. The optimized FFT codes will reduce the runtime of these programs by about 20-40%. The programs *phasediff*, and *conv* read/write GMT *grd*-files in *netcdf* format and therefore require that the user link with the libraries *libgmt.a* and *libnetcdf.a*. These programs, as well as many standard GMT routines, are called from shell scripts. A list of the current scripts is found by executing the command `gmtsar.csh`.

<i>align.csh</i>	align a pair of SAR images
<i>align_batch.csh</i>	align a stack of SAR images
<i>align_tops.csh</i>	geometric alignment of TOP-mode data
<i>baseline_table.csh</i>	make baseline vs time table
<i>cleanup.csh</i>	cleanup the directories
<i>dem2topo_ra.csh</i>	transform a dem into range and azimuth coordinates
<i>filter.csh</i>	filter the interferogram and make amp, phase and corr
<i>fitoffset.csh</i>	solve for the affine parameters
<i>geocode.csh</i>	convert range/azimuth to lon/lat
<i>grd2kml.csh</i>	make a kml file for google earth
<i>intf.csh</i>	make the interferogram from a single pair of SLCs
<i>intf_batch.csh</i>	make interferograms for a set of aligned SLCs
<i>make_a_offset.csh</i>	make azimuth offsets
<i>make_dem.csh</i>	construct a dem from tiles
<i>pre_proc.csh</i>	preprocess the raw SAR data for a pair of images
<i>pre_proc_batch.csh</i>	preprocess raw SAR data for a stack of images
<i>p2p_SAT.csh</i>	process an SAT interferogram from end-to-end (many p2p scripts)
<i>proj_ll2ra.csh</i>	project a grd file from lon/lat to range/azimuth
<i>proj_ll2ra_ascii.csh</i>	project points from lon/lat to range/azimuth
<i>proj_ra2ll.csh</i>	project a grd file from range/azimuth to lon/lat
<i>proj_ra2ll_ascii.csh</i>	project points from range/azimuth to lon/lat
<i>sarp.csh</i>	focus a single SAR image
<i>slc2amp.csh</i>	make a amplitude image from a SLC
<i>snaphu.csh</i>	unwrap phase using snaphu
<i>stack.csh</i>	compute mean and standard deviations of a stack of images
<i>update_PRM.csh</i>	replace a value in a PRF-file

Executing one of the commands will provide its usage:

```
% sarp.csh
```

```
Usage: sarp.csh file.PRM
```

```
Example: sarp.csh IMG-HH-ALPSRP049040660-H1.0...A.PRM
```

### 3 Processing Examples

The modules of the GMTSAR package can be connected in a variety of ways to do specialized SAR and InSAR processing. The foundation of the code is all optimized, written in C, and we hope is functionally stable. For example, the SAR processor `esarp.c` has remained stable for more than a decade. We expect this C-code as well as the GMT code, will be stable on a time frame of years. New preprocessor code will need to be written as new satellite data becomes available but everything downstream should not change significantly.

The flexible aspect of the package is the c-shell scripts to perform different types of InSAR processing. Indeed, c-shell is not a particularly good language for writing large scripts and we hope this part of the system will evolve based on input from knowledgeable users. So far we have developed three standard InSAR recipes. They are 2-pass processing, stacking for time series analysis, and ScanSAR to strip-mode interferometry. We will outline the processing stages in these three examples. The first example is also used for testing the installation (Appendix G) so we will step through the InSAR processing for a pair of ALOS SAR images spanning the 2010 M7.2 Baja, Mexico Earthquake.

### 3.1 Two-pass processing

A common approach to InSAR processing is to form an interferogram using two SAR images and a digital elevation model. A flow diagram of a script called `p2p_SAT.csh` is shown in Figure 3. Selecting a pair of images having the desired perpendicular baseline and time span characteristics is an important issue that will be discussed in the next section under stacking and time series. This example recovers the coseismic displacement from an earthquake so the ALOS PALSAR images are selected as the pair spanning the M7.2 Baja, Mexico Earthquake having the minimum time span. To prepare for the processing one needs to generate a digital elevation grid of the area in longitude and latitude coordinates spanning an area greater than the SAR coverage (e.g., longitude -116.25 to -115.16 and latitude 32.16 to 33.16). The heights should be referenced to the WGS84 ellipsoid and not the geoid. The command `make_dem.csh` will make the grid but only if it has access to the tiles of SRTM or ASTER topography data as well as the EGM96 geoid model. A topographic grid of any land area can be created using the website <http://topex.ucsd.edu/gmtsar>. The user places this topography grid (`dem.grd`) in a directory called `/topo` and the two scenes of raw SAR data in L1.0 CEOS format in the directory called `/raw`. The first scene is the reference image and the second scene is the repeat image. (Later when discussing the alignment of large stacks of SAR images we will use additional terminology of a single master image and many slave images.) After modifying a file called `configure.txt` the user uses the command `p2p_ALOS.csh IMG-HH-ALPSRP207600640-H1.0..A IMG-HH-ALPSRP227730640-H1.0..A configure.txt` and waits for the results.

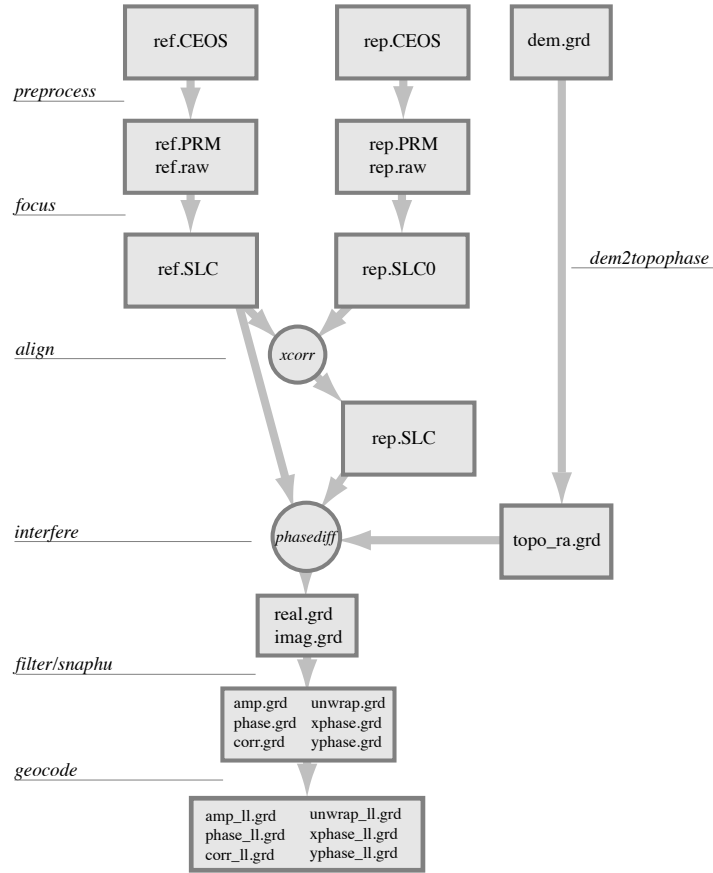


Figure 3: Flow diagram of 2-pass processing beginning with raw SAR and orbital data and a digital elevation grid (`dem.grd`) and ending with geocoded grids of interferometric products.

An overview of the 7 main processing steps is shown in Figure 3 and the modules are provided in Table 3. The first step is to preprocess raw SAR data and orbital information, usually in L1.0 CEOS format, to create an ascii parameter file (e.g. Table B1) and a raw data file (e.g., Figure B3). This preprocessing involves specialized code to extract orbital position and velocity information from the leader files, align the raw radar echoes on a common near range, align the repeat image to the reference image, and estimate the Doppler centroid of the raw data. The second step is to focus each image to create two single look complex images as described in Appendix B. The third step is to align the repeat image to the reference image. This is accomplished by first using the orbital information to estimate the shift in range and azimuth needed to align the upper left corner of the images. Then many small patches (e.g., 64x64) are extracted from each image and cross correlated to determine 6 affine parameters needed to warp the repeat image to match the second image. The repeat image is refocussed using these 6 parameters

resulting in sub-pixel alignment between the reference and repeat images. Smaller scale pixel shifts due to large amplitude surface topography are corrected at the *interfere* step. The fourth step (*dem2topo\_ra*) is to transform the digital elevation model from longitude, latitude, and topography into range, azimuth, and topography. This is done using the precise orbital information of the reference image. Sometimes a -1 pixel range shift (i.e., derived from a cross correlation between the amplitude image of the master and the range gradient of the topographic phase, *offset\_topo*) is needed to improve the alignment. The fifth step is to interfere the reference and repeat SLC's using the *topo\_shift.grd* to both refine the image alignment of the repeat image due to topography parallax, and to remove the baseline-dependent topographic phase from the repeat image prior to cross multiplication (*phasediff*). Thus all the position and phase corrections are applied at the full resolution of the SLC's. The sixth step *filter/snaphu* is to low-pass filter (*conv*) and decimate (4 in azimuth and 1 or 2 in range) the real and imaginary components of the interferogram and compute standard products of amplitude, phase, and coherence. The Gaussian filter wavelength is selected by the user in the *config.txt* file. A second set of filtered interferograms is also created using a modified Goldstein filter algorithm (*phasefilt*) (Goldstein and Werner 1997; Baran et al. 2003). Optionally one can compute unwrapped phase using the *snaphu* program of Chen and Zebker (Chen and Zebker 2000) as well as phase gradients Sandwell and Price 1998 in the range (*xphase*) and azimuth (*yphase*) directions. To this point all the processing is done in the radar coordinates where the spacing of the range pixels before decimation is  $c\tau/2$  and the spacing of the azimuth pixels before decimation is  $V/PRF$ . These parameters can be found in the parameter files (See Appendix B).

The final step is to *geocode* all the products by transforming from the range/azimuth coordinate system of the master image to longitude and latitude. The c-shell scripts also produce postscript images and kml-images of relevant products using the capabilities of GMT. An image of the sample interferogram superimposed on the dem is shown in Figure 4.

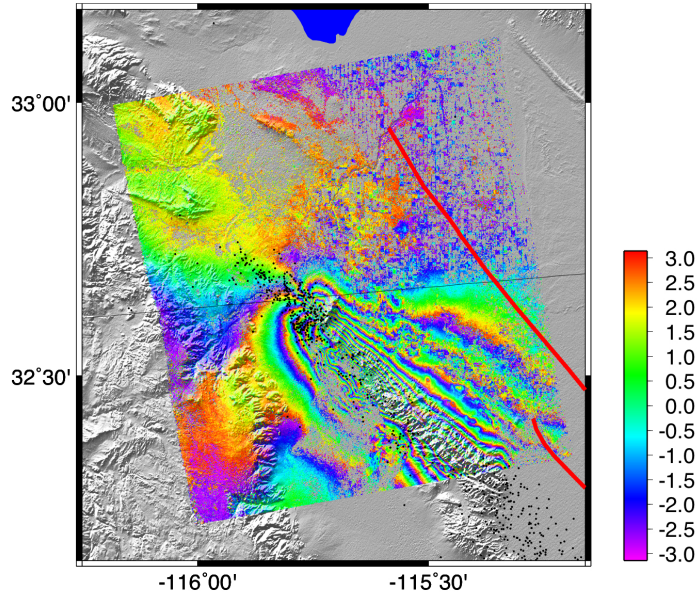


Figure 4: Interferometric phase for an ascending track (T211, F0640) of ALOS PAL-SAR data over the April 4, 2010, El Major-Cucapah earthquake, Baja Mexico. One fringe represents 11.8 cm displacement away from the radar. The phase is superimposed on the gradient of the topography and other components such as faults and earthquake epicenters are easily added.

### 3.2 Stacking for time series

A second common approach to InSAR processing is to form a time series of deformation from a stack of images. There are a variety of methods ranging from averaging to small baseline subsets to time series to persistent scattering. The practical, and sometimes most challenging issue related to these approaches is to geometrically align a large stack of images and align this stack with a topographic phase model. (Note a new purely geometric approach to image alignment is presented in Appendix E.) A diagram of a stack of SAR images is shown in Figure 5. To achieve interferometric phase coherence, the alignment must have subpixel accuracy in the radar coordinates of range and azimuth. In addition, there should be greater than 20% overlap in the Doppler centroid or bursts in ScanSAR images. We use the terminology that many *slave* images are geometrically aligned with one *master* image. Once the alignment is done, an interferogram can be constructed from any pair of images in the stack. We use the terminology of *reference* and *repeat* images for the first and second acquisition of the interferometric pair, respectively.

1 – preprocess	<i>update_PRM.csh</i> <i>ALOS_pre_process.csh</i>	
<b><i>pre_proc.csh</i></b>	<i>ALOS_fbd2fbs.c</i> <i>ALOS_fbs2fbd.c</i>	
2 – align and focus	<i>sarp.csh</i> <i>SAT_baseline.c</i> <i>xcorr.c</i> <i>fitoffset.csh</i>	<i>esarp.c</i>   <i>trend2d.c</i>
3 – topo_ra	<i>grd2xyz.c</i> <i>SAT_1lt2rat.c</i> <i>blockmedian.c</i> <i>surface.c</i> <i>topo2phase.c</i> <i>grdimage.c</i>	
4 – interfere and filter	<i>SAT_baseline.c</i> <i>phasediff.c</i> <i>conv.c</i> <i>grdmath.c</i> <i>grdimage.c</i> <i>phasefilt.c</i>	
5 – unwrap phase	<i>grdcut.c</i> <i>grdmath.c</i> <i>snaphu.csh</i> <i>grd2xyz.c</i> <i>snaphu.c</i> <i>xyz2grd.c</i> <i>grdimage.c</i>	
6 – geocode	<i>grdmath.c</i> <i>proj_ra2ll.csh</i>      <i>grd2kml.csh</i>	<i>grd2xyz.c</i> <i>gmtconvert.c</i> <i>blockmedian.c</i> <i>surface.c</i> <i>grdtrack.c</i>   <i>grdimage.c</i> <i>ps2raster.c</i>

Table 3: Algorithm and codes for 2-pass processing – p2p\_SAT.csh

GMTSAR commands are italic. *black*: *c-shell script*, *red*: *GMTSAR C-code*, *blue*: *GMT C-code*, *green*: *snaphu phase unwrapper* (Chen and Zebker 2000).

Note this example if for processing an *ALOS* interferogram. For another satellite (e.g. Envisat) replace the characters *ALOS* by *ENVI*. Also note TOPS-mode data are processed slightly differently since the *align.csh* step is performed using orbital data rather than *xcorr* and *fitoffset*.

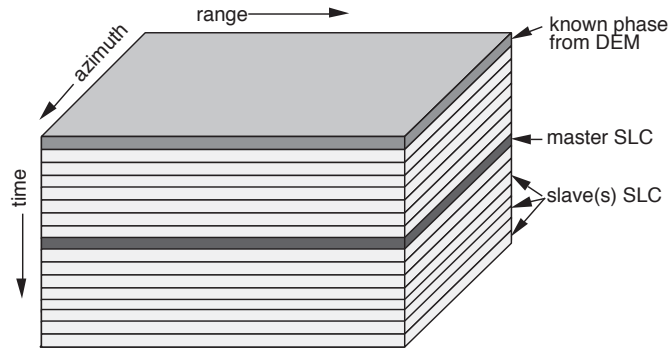


Figure 5: Schematic diagram of a stack of SAR images and a topographic phase image.

Image alignment is problematic if the perpendicular baseline between the master image and one of the slave images is greater than about  $3/4$  of the critical baseline because the images will be *baseline decorrelated* (Appendix C). *Temporal decorrelation* can also occur when the scattering surface of the earth changes between the master and slave acquisitions because of vegetation, snow, or other small-scale surface disturbances. As discussed above, our image alignment algorithm begins with a guess at the range and azimuth shift based on the precise orbit and then uses 2-dimensional cross correlation on small patches. If there are no areas in the images that are correlated then this cross correlation approach can fail to achieve subpixel correlation. A plot of perpendicular baseline versus time can be used to identify images that lie far from the master and therefore may not be suitable for subpixel alignment. An example of a baseline vs. time plot for an ALOS stack (Track 213, Frame 0660, Coachella Valley, California) is shown in Figure 6. Temporal decorrelation is less of an issue in this desert area. However in this case the baseline of ALOS drifts by more than 5 km over a time span of 2 years. The critical baseline for the lower bandwidth (FBD) data is 6 km so, for example the acquisition on orbit number 12285 lies more than 4 km from acquisition on orbit 13627.

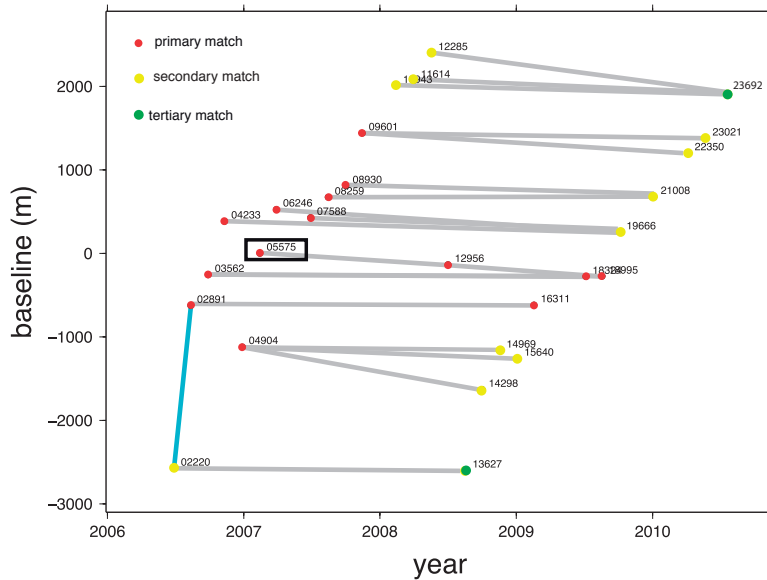


Figure 6: Baseline versus time plot partly created by the `pre_proc_batch.csh` command. Colored dots were added by user and represent the intended primary (red), secondary (yellow) and tertiary (green) image alignment. The grey lines were added and represent candidate interferograms. The interferometric pair marked by a blue line is used in Appendix C for assessing the accuracy of the earth curvature and topographic phase corrections.

We perform the image alignment using the following steps:

1. Preprocess all the images independently and examine the PRM files for median values of Doppler centroid (`fd1`), near range (`near_range`), and earth radius (`earth_radius`). An example command is:

```
ALOS_pre_process IMG-HH-ALPSRP022200660-H1.0...A LED-ALPSRP022200660-H1.0...A
```

In this case there are 27 images so one creates a script to pre-process all 27 images.

2. Based on this analysis one preprocesses all the images using the batch processing command.

```
pre_proc_batch.csh ALOS data.in
```

The file `data.in` defines the zero-baseline image and the common parameters for the stack.

```
IMG-HH-ALPSRP055750660-H1.0...A -near 846567 -radius 6371902.401705 -fd1 100
IMG-HH-ALPSRP022200660-H1.0...A
IMG-HH-ALPSRP028910660-H1.0...A
MG-HH-ALPSRP035620660-H1.0...A
```

This command will also create a baseline versus time plot as shown in Figure 6.

3. The next step is to select the master image somewhere in the center of the baseline versus time plot. The objective in this case is to form long time span interferograms having relatively short baselines so the user connects candidate interferograms as shown in the grey lines on Figure 6. The correlation of an interferogram deteriorates as the image alignment degrades so optimally one would cross correlate each interferometric pair. However, since we would like to be able to stack interferograms and apply a uniform topographic phase correction it is advantageous to have all the images in the stack at least crudely ( $< 2$  pixels) aligned. In this case we only plan to make interferograms among images that are nearby in baseline so image alignment only needs to be accurate locally. Our approach is to have a multi-step alignment process where a set of images near the master in baseline vs. time space are aligned directly to the master (*primary match* red dots in Figure 6). Once this set is aligned we can treat them each as surrogate masters and align images on the periphery of the baseline versus time plot to one of the nearby surrogates. We call this a *secondary match* (yellow dots in Figure 6). For images very far from the master we can perform a *tertiary match*.
4. The user puts this alignment information into a file *align.in* and executes the command:  
`align_batch.csh ALOS align.in`  
 All of the information on primary, secondary, and tertiary alignment is contained in the *align.in* file which is constructed by the user based on the baseline versus time plot. The example for the set shown in Figure 6 follows.

```

IMG-HH-ALPSRP055750660-H1.0__A:IMG-HH-ALPSRP028910660-H1.0__A:IMG-HH-ALPSRP055750660-H1.0__A
IMG-HH-ALPSRP055750660-H1.0__A:IMG-HH-ALPSRP035620660-H1.0__A:IMG-HH-ALPSRP055750660-H1.0__A
IMG-HH-ALPSRP055750660-H1.0__A:IMG-HH-ALPSRP042330660-H1.0__A:IMG-HH-ALPSRP055750660-H1.0__A
IMG-HH-ALPSRP055750660-H1.0__A:IMG-HH-ALPSRP049040660-H1.0__A:IMG-HH-ALPSRP055750660-H1.0__A
IMG-HH-ALPSRP055750660-H1.0__A:IMG-HH-ALPSRP062460660-H1.0__A:IMG-HH-ALPSRP055750660-H1.0__A
IMG-HH-ALPSRP055750660-H1.0__A:IMG-HH-ALPSRP075880660-H1.0__A:IMG-HH-ALPSRP055750660-H1.0__A
IMG-HH-ALPSRP055750660-H1.0__A:IMG-HH-ALPSRP082590660-H1.0__A:IMG-HH-ALPSRP055750660-H1.0__A
IMG-HH-ALPSRP055750660-H1.0__A:IMG-HH-ALPSRP089300660-H1.0__A:IMG-HH-ALPSRP055750660-H1.0__A
IMG-HH-ALPSRP055750660-H1.0__A:IMG-HH-ALPSRP096010660-H1.0__A:IMG-HH-ALPSRP055750660-H1.0__A
IMG-HH-ALPSRP055750660-H1.0__A:IMG-HH-ALPSRP129560660-H1.0__A:IMG-HH-ALPSRP055750660-H1.0__A
IMG-HH-ALPSRP055750660-H1.0__A:IMG-HH-ALPSRP163110660-H1.0__A:IMG-HH-ALPSRP055750660-H1.0__A
IMG-HH-ALPSRP055750660-H1.0__A:IMG-HH-ALPSRP183240660-H1.0__A:IMG-HH-ALPSRP055750660-H1.0__A
IMG-HH-ALPSRP055750660-H1.0__A:IMG-HH-ALPSRP189950660-H1.0__A:IMG-HH-ALPSRP055750660-H1.0__A
IMG-HH-ALPSRP049040660-H1.0__A:IMG-HH-ALPSRP022200660-H1.0__A:IMG-HH-ALPSRP055750660-H1.0__A
IMG-HH-ALPSRP049040660-H1.0__A:IMG-HH-ALPSRP142980660-H1.0__A:IMG-HH-ALPSRP055750660-H1.0__A
IMG-HH-ALPSRP049040660-H1.0__A:IMG-HH-ALPSRP149690660-H1.0__A:IMG-HH-ALPSRP055750660-H1.0__A
IMG-HH-ALPSRP049040660-H1.0__A:IMG-HH-ALPSRP156400660-H1.0__A:IMG-HH-ALPSRP055750660-H1.0__A
IMG-HH-ALPSRP075880660-H1.0__A:IMG-HH-ALPSRP196660660-H1.0__A:IMG-HH-ALPSRP055750660-H1.0__A
IMG-HH-ALPSRP082590660-H1.0__A:IMG-HH-ALPSRP210080660-H1.0__A:IMG-HH-ALPSRP055750660-H1.0__A
IMG-HH-ALPSRP096010660-H1.0__A:IMG-HH-ALPSRP109430660-H1.0__A:IMG-HH-ALPSRP055750660-H1.0__A
IMG-HH-ALPSRP096010660-H1.0__A:IMG-HH-ALPSRP116140660-H1.0__A:IMG-HH-ALPSRP055750660-H1.0__A
IMG-HH-ALPSRP096010660-H1.0__A:IMG-HH-ALPSRP122850660-H1.0__A:IMG-HH-ALPSRP055750660-H1.0__A
IMG-HH-ALPSRP096010660-H1.0__A:IMG-HH-ALPSRP223500660-H1.0__A:IMG-HH-ALPSRP055750660-H1.0__A
IMG-HH-ALPSRP096010660-H1.0__A:IMG-HH-ALPSRP230210660-H1.0__A:IMG-HH-ALPSRP055750660-H1.0__A
IMG-HH-ALPSRP022200660-H1.0__A:IMG-HH-ALPSRP136270660-H1.0__A:IMG-HH-ALPSRP055750660-H1.0__A

```

The first image is the name of the master or surrogate master, the second image is the slave to be aligned, and the third image is the supermaster that is common to all images. Note that the order of the alignment is sometimes important since the surrogate master needs to be aligned to the master before it can serve as a surrogate. Aligning a stack of

27 images can take quite a bit of computer time so it is best to do this in a batch mode and head home for the evening.

5. While waiting for the image alignment, one can construct the topographic phase using the master image. Generate a *dem.grd* using the web site (<http://topex.ucsd.edu/gmtsar>) and place it in a subdirectory */topo* at the same level as */raw* and */SLC*.
6. Make a set of interferograms using the command

```
int_batch.csh ALOS intf.in intf.config
```

The an example file for *intf.config* can be copied from the location

```
GMTSAR/gmtsar/csh/example.intf.config
```

and edited for this particular data set. The file *intf.in* contains a list of the interferometric pairs. In this case we make 22 interferograms (Figure 7).

```
IMG-HH-ALPSRP022200660-H1.0...A: IMG-HH-ALPSRP136270660-H1.0...A  
IMG-HH-ALPSRP028910660-H1.0...A: IMG-HH-ALPSRP163110660-H1.0...A  
IMG-HH-ALPSRP035620660-H1.0...A: IMG-HH-ALPSRP183240660-H1.0...A  
IMG-HH-ALPSRP035620660-H1.0...A: IMG-HH-ALPSRP189950660-H1.0...A  
IMG-HH-ALPSRP042330660-H1.0...A: IMG-HH-ALPSRP196660660-H1.0...A
```

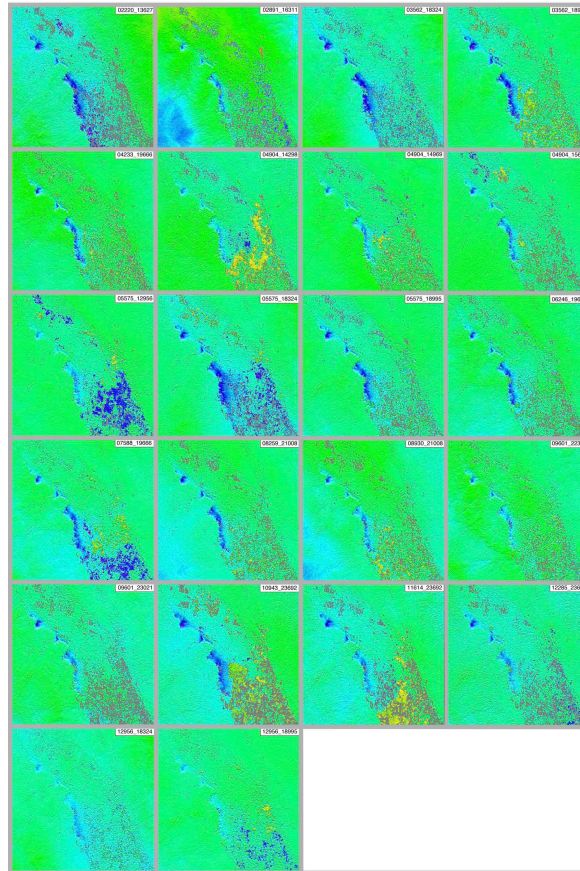


Figure 7: Twenty-two interferograms of a small area in Coachella Valley where ground subsidence is prominent. Cold color denotes ground moves away from the radar. Color scale saturates at +/- 10 cm. A linear trend was removed from each interferogram. Projection is radar coordinates.

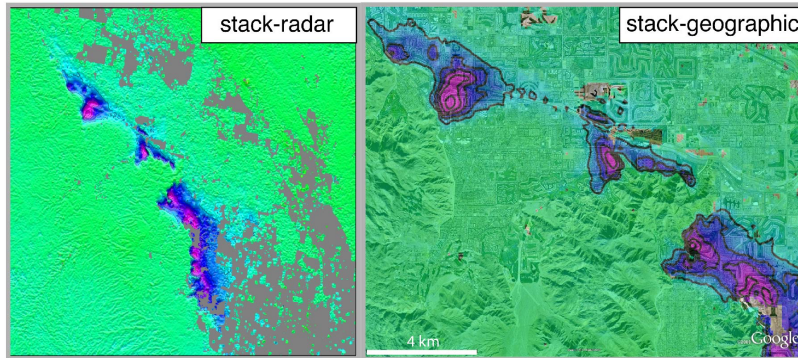


Figure 8: Stack of 22 interferograms spanning a total interval of 48 years. Contours are 1 cm/yr LOS displacement toward radar (mostly vertical in this case). (left) radar coordinates and (right) geographic coordinates. The command `grd2kml.csh` is used to create a kml-file for Google Earth. Subsidence rates exceeding 4 cm/y occur in Palm Desert, Indian Wells, and La Quinta areas due to groundwater pumping (Sneed, Brandt, and Solt 2014).

#### 7. Use SBAS to make a time series

```
sbas intf.tab scene.tab 88 28 700 1000 -smooth 1
```

For this example the user has prepared 88 files of unwrapped phase as well as 88 files of coherence derived from 28 SAR images. Each file has 700 columns and 1000 rows. The user must also prepare the `intf.tab` and `scene.tab` files as follows.

##### ***intf.tab***

```
(format: unwrap.grd corr.grd ref_id rep_id B_perp)
cut_02220_13627.grd corcut_02220_13627.grd 02220 13627 -19.387899
cut_02891_03562.grd corcut_02891_03562.grd 02891 03562 369.671332
cut_02891_04904.grd corcut_02891_04904.grd 02891 04904 -496.279669
cut_02891_05575.grd corcut_02891_05575.grd 02891 05575 627.184879
cut_02891_16311.grd corcut_02891_16311.grd 02891 16311 6.788277
cut_02891_18324.grd corcut_02891_18324.grd 02891 18324 348.590674
```

##### ***scene.tab***

```
(format: scene_id number_of_days)
02220 176
02891 222
03562 268
04233 314
04904 360
05575 406
```

The output is 28 files of displacement time series `disp_###.grd` in mm as well as a single mean velocity `vel.grd` in mm/yr.

### 3.3 ScanSAR Interferometry

(These notes are *ONLY* for ALOS-1 ScanSAR. ALOS-2 ScanSAR and Sentinel-1 wide swath data are supplied as SLCs and can be treated just like normal swath-mode data so *you can probably skip this section.*)

GMTSAR can perform two types of ScanSAR interferometry as more fully described in Appendix D. ScanSAR to ScanSAR interferometry is possible when the reference and repeat bursts overlap by more than about 20% but one must be very lucky to have more than 20% overlap. The second approach, that is always possible, is ScanSAR to strip mode interferometry. The only difference between Scan to strip processing and strip to strip processing is the preprocessing steps to convert one of the subswaths of the ScanSAR data into a file that looks like a standard strip-mode raw data file. Here we provide a step-by-step example of processing a ScanSAR to strip (FBD) interferogram over Los Angeles Basin (Figure 9). This interferogram has a perpendicular baseline of 108 m and time span of 184 days. The track number is 538 and the frame number is 2930 for FBD and 2950 for ScanSAR.

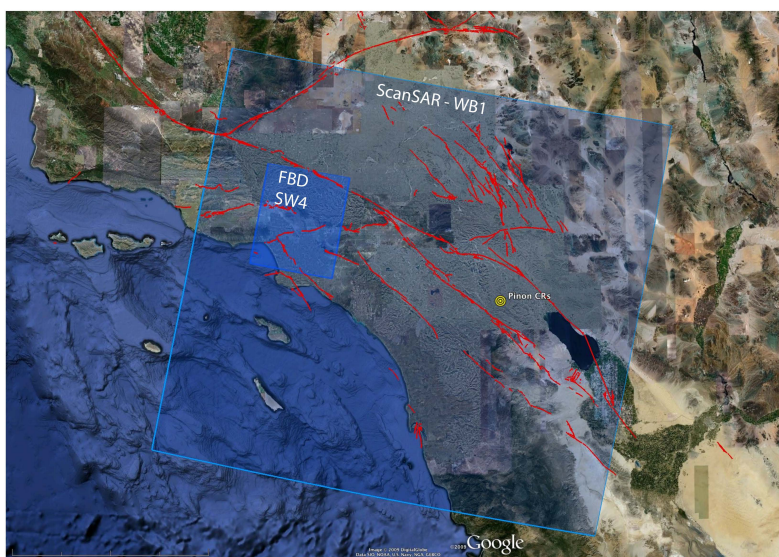


Figure 9: Location of ALOS Scansar and FBD acquisition over Los Angeles for track 538. Subswath 4 (SW4) has the same look angle as standard strip-mode data and also a similar PRF.

The processing steps are:

1. Preprocessing FBD raw data is done by *ALOS\_pre\_process*. Unlike the above case where we convert all the lower bandwidth (FBD) data to the higher bandwidth (FBS) mode, we keep the strip data in the FBD mode because this matches the bandwidth of the ScanSAR data. Preprocessing a subswath of ScanSAR raw data is done using the program *ALOS\_pre\_process\_SS*. This preprocessor has many options as shown next.

	SW1	SW2	SW3	SW4	SW5
<i>near range (m)</i>	730097	770120	806544	848515	878195
<i>PRF (Hz)</i>	1692	2370	1715	2160	1916
<i>nburst</i>	247	356	274	355	327
<i><math>\Delta t(s)</math></i>	0.146	0.150	0.160	0.164	0.171
<i>nsamples</i>	4976	4720	5376	4432	4688
<i>off nadir (deg)</i>	20.1	26.1	30.6	34.1	36.5

Table 4: Nominal radar parameters for each ScanSAR sub swath. The number of echoes in a burst *nburst* is the only fixed parameter.

```
% ALOS_pre_process_SS
Usage: ALOS_pre_process_SS imagefile LEDfile [-near near_range] [-radius RE] [-swath swath#] [-burst_skip] [-num_burst] [-swap] [-V] [-debug] [-quiet]
creates data.raw and writes out parameters (PRM format) to stdout
imagefile ALOS Level 1.0 complex file (CEOS format):
LEDfile ALOS Level 1.0 LED file (CEOS leaderfile format):
options:
-near near_range    specify the near_range (m)
-radius RE         specify the local earth radius (m)
-swath             specify swath number 1-5 [default 4]
-burst_skip       number of burst to skip before starting output (1559 lines/burst)
-num_burst        number of burst to process [default all]
                  there are 72 bursts in a WB1 frame
-swap             do byte-swap (should be automatic)
-fd1 [DOPP]       sets doppler centroid [fd1] to DOPP
-V               verbose write information)
-debug           write even more information
-quiet          don't write any information
```

Example:

```
ALOS_pre_process_SS IMG-HH-ALPSRS049842950-W1.0_D LED-ALPSRS049842950-W1.0_D
-near 847916 -radius 6371668.872945 -burst_skip 5 -num_burst 36
```

burst #	look_angle	#lines_burst
1	20.1	247
2	26.1	356
3	30.6	274
4	34.1	355
5	36.5	327

By default the `ALOS_pre_process_SS` uses subswath 4, which naturally overlaps the swath mode imagery along the same track. The `num_burst` parameter represents the number of burst that will be extracted from a long subswath of ScanSAR. The `burst_skip` parameter controls the number of burst to skip before preprocessing raw data and it is determined by trial and error. After PRM files of both the ScanSAR mode and FBD mode are generated, the user runs `ALOS_baseline` to see if the `ashift` value is reasonable.

If not, the user chooses another *burst\_skip* parameter and repeats this process until the *a\_shift* is less than 1703. For this LA example the following command was used.

```
ALOS_pre_process_SS IMG-HH-ALPSRS049842950-W1.0_D LED-ALPSRS049842950-W1.0_D
-nodopp -near 847916 -radius 6371729.321330 -num_burst 18 -burst_skip 5
```

Note that 18 bursts were extracted which will match the length of a single FBD frame. As described above frame-by-frame processing is usually more reliable than processing very long swaths. The *ALOS\_pre\_process\_SS* terminates when it reaches the end of the data file or the PRF changes in any of the subswaths. With some experimentation one can set the *burst\_skip* to skip over the PRF change and start a fresh swath.

- As described in Appendix D, the *ALOS\_pre\_process\_SS* simply inserts zero for the missing lines in each subswath to create a standard strip-model file. To achieve optimal correlation between the scan and strip combination, one needs to zero the matching lines in the FBD data (Bertran-Ortiz and Zebker 2007). This step is performed by the *ALOS\_fbd2ss* which simply replaces real data with zeroes! The next task is to determine where to insert the zeros into the FBD data. Two parameters are needed to account for the shift and stretch between the two acquisitions. The *ashift* is the azimuth shift needed to align the first row of the FBD raw data to the subswath of ScanSAR data and the *a\_stretch\_a* accounts for the PRF difference. These parameters can be obtained by aligning the ScanSAR SLC with the FBD SLC images using *align.csh*. Essential (but not complete) steps in this alignment are listed below to guide the reader.

```
update_PRM.csh IMG-HH-ALPSRS049842950-W1.0_D.SW4.PRM num_valid_az 10224
(note that 10224 is the length of 6 bursts of length 1704)
```

```
update_PRM.csh IMG-HH-ALPSRP076682930-H1.0_D.PRM num_valid_az 10224
(use the same synthetic aperture length for the FBD.)
```

```
sarp.csh IMG-HH-ALPSRP076682930-H1.0_D.PRM IMG-HH-ALPSRP076682930 H1.0_D.SLC
(focus the FBD)
```

```
sarp.csh IMG-HH-ALPSRS049842950-W1.0_D.SW4.PRM IMG-HH-ALPSRS049842950-W1.0_D.SW4.SLC
(focus the WB1)
```

```
ALOS_baseline IMG-HH-ALPSRS049842950-W1.0_D.SW4.PRM IMG-HH-ALPSRP076682930-H1.0_D.PRM
(get a guess for the rshift and ashift to align the upper left corner of the FBD to the WB1. Update the ashift and rshift in the PRM-file of the FBD image then do a cross correlation.)
```

```
xcorr IMG-HH-ALPSRS049842950-W1.0_D.SW4.PRM IMG-HH-ALPSRP076682930-H1.0_D.PRM
```

```
fitoffset.csh freq_xcorr.dat
(find the exact ashift and a_stretch_a parameter for the zeroing program ALOS_fbd2ss)
```

```
ALOS_fbd2ss IMG-HH-ALPSRP076682930-H1.0_D.PRM IMG-HH-ALPSRP076682930-H1.0_D.ss.PRM
733 1704 0.00437308
(finally do the zeroing ashift = 733, num_valid_az/6, a_stretch_a)
```

Note the *rshift* and *ashift* of the *IMG-HH-ALPSRP076682930-H1.0\_D.ss.PRM* should be reset to zero after *ALOS\_fbd2ss*.

- After the *ALOS\_fbd2ss* the special preprocessing steps are completed, the data are processed as one would normally process two strip-mode acquisitions similar to the steps found in *process2pass.csh*. The essential (but not complete) steps are listed below. Note *p2p\_SAT.csh* can't be used directly because of the non standard filenames; some creative scripting or links could fix solve this issue.

```

align.csh ALOS IMG-HH-ALPSRS049842950-W1.0_D_SW4 IMG-HH-ALPSRP076682930-H1.0_D_ss

dem2topo_ra.csh master.PRM dem.grd
intf.csh IMG-HH-ALPSRS049842950-W1.0_D_SW4.PRM IMG-HH-ALPSRP076682930-H1.0_D_ss.PRM -topo
topo_ra.grd

filter.csh IMG-HH-ALPSRS049842950-W1.0_D_SW4.PRM IMG-HH-ALPSRP076682930-H1.0_D_ss.PRM
gauss_alos_300m 2

geocode.csh 0.1

```

The processed interferogram is shown in Figure 10. To make the interferogram more interesting we did not apply the topographic phase correction. During this analysis we also processed a standard FBD to FBD interferogram. For these two interferograms of the same area and about the same time interval, the average coherence of the ScanSAR to FBD interferogram was lower (0.38) than the FBD to FBD interferogram (0.67). Therefore there are really no advantages to ScanSAR to strip-mode interferometry except that it provides more interferometric opportunities in case of events. For ScanSAR processing we commonly use a longer wavelength filter (300 or 500 m) to improve the visibility of the fringes.

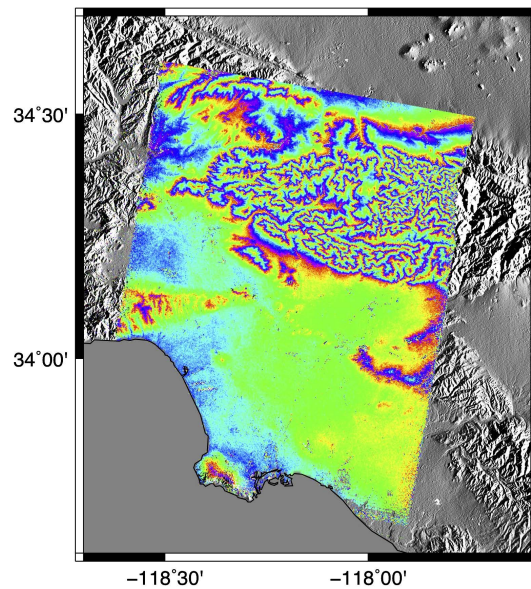


Figure 10: An example of ScanSAR to FBD mode interferogram over Los Angeles Basin where the topographic phase has not been removed.

ScanSAR to ScanSAR processing is very similar to the sequence described above although one must be lucky to find a pair having sufficient burst overlap. For each WB1 data file one creates 5 independent interferograms for each of the 5 subswaths. As shown in 4, each subswath has a very different PRF so the interferograms are not easily mosaicked in the radar coordinates. However, if the data are processed with a consistent earth radius, the interferograms will abut seamlessly when they are projected back into geographic coordinates as shown in Figure 11.

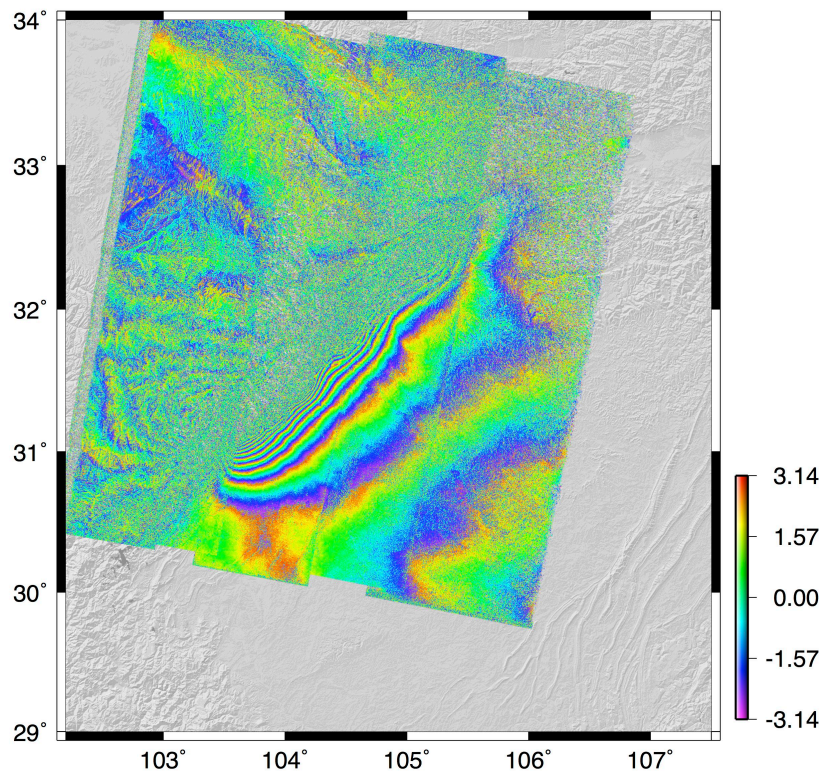


Figure 11: Descending ScanSAR to ScanSAR interferogram spanning the Mw 7.9 2008 Wenchuan earthquake (11.8 cm per fringe). The interferogram consists of 5 sub-swaths across look direction that abut almost seamlessly with no position or phase adjustment. The decorrelation in the mountainous area to the left of the red surface rupture line is due to the rather long baseline (920m) and high relief.

### Acknowledgements

GMTSAR was developed over a period of 19 years by many people. Howard Zebker provided the original FORTRAN code for the SAR processor. Evelyn Price translated the SAR processor into C which greatly simplified the code although the SAR focusing algorithm remained unchanged. Price and Sandwell expanded this into a complete InSAR package by adding cross correlation and phase modules. Paul Jamason wrote the original preprocessors for ERS (CCRS and DPAF). Remko Sharro's (Delft University) getorb routines were originally used to compute precise orbits for proper focus, geolocation, and baseline estimation. The GIPS package, written by Peter Ford at MIT, was used to develop an overall system called SIOSAR which remained stable for 11 years. Sean Buckley's Envisat decoder is used in the Envisat preprocessor. In 2010 the GIPS software was replaced by GMT modules. Rob Mellors rewrote the ALOS preprocessing code developed by Sandwell into a robust package which was later translated by Matt Wei into the ERS and ENVISAT preprocessors. Rob also wrote completely new software for image cross correlation as well as for Goldstein/Werner interferogram filtering. Xiaopeng Tong did extensive testing and

refinement of the phase module to remove some of the approximations built into SIOSAR. He also developed the shell scripts for two-pass processing, stacking and the sbas C-code. The Snapu phase unwrapping code, written by Chen and Zebker, is used without modification in GMTSAR. Paul Wessel provided several enhancements to GMT to deal with processing of large binary tables. He also modified all of the code to interface with GMT API routines during his sabbatical leave at Scripps. In addition he developed code to create kml output. GMTSAR makes extensive use of the GMT routines blockmedian and surface which were developed by Walter Smith and Paul Wessel. These lie at the heart of the GMT-SAR algorithms for transforming between geographic and radar coordinates. We believe these routines are responsible for the ability of GMTSAR to maintain phase coherence in areas of rugged terrain where other InSAR packages sometimes fail. Kahlid Soofi supported this effort through funding from Conoco/Phillips as well as testing and development of the software. Most recently Xiaohua Xu and Sandwell co-developed the pre-processing and alignment codes needed for TOPS-mode interferometry under the guidance of Pablo Gonzalez. Many users provided feedback and bug reports to achieve a relatively robust and stable set of software. The entire 19-year development was done as an effort to improve the resolution and accuracy of interferograms. Each iteration provided incremental improvements over the original Stanford/JPL code. The latest package was designed to move to the next level of processing thousands of wide-swath interferograms with minimal human intervention. San Diego State University and Scripps Institution of Oceanography provided salary support for Mellors and Sandwell during the last 2 years of code development. In addition, Mellors was partially supported under the auspices of the U.S. Department of Energy by Lawrence Livermore National Laboratory under Contract DE-AC52-07NA27344. Recent development was supported by the NSF Geoinformatics Program 1347204.

## References

- Baran, I. et al. (2003). "A modification to the Goldsetin Radar interferogram filter." In: *IEEE Trans. Geoscience Rem. Sens.* 41.9, pp. 2114–2118.
- Bertran-Ortiz, A. and H. A. Zebker (2007). "ScanSAR-to-Stripmap Mode Interferometry Processing Using ENVISAT/ASAR Data". In: *IEEE Trans. Geoscience Rem. Sens.* 45.11, pp. 3468–3480.
- Chen, C. and H. A. Zebker (2000). "Network approaches to two-dimensional phase unwrapping: intractability and two new algorithms". In: *Journal of the Optical Society of America A* 17, pp. 401–414.
- Curlander, J. C. and R. N. McDonough (1991). *Synthetic Aperture Radar: Systems and Signal Processing*. Chapter 4. New York City: John Wiley & Sons.
- Farr, T.G. et al. (2004). "The Shuttle Radar Topography Mission". In: *Rev. Geophys.* 17. doi:10.1029/2005RG000183.
- Goldstein, R.M. and C.L. Werner (1997). "Radar ice motion interferometry". In: *Proc. 3rd ERS Symp.* Vol. 2:11. Florence, Italy, pp. 969–972.
- Press, W.H. et al. (1992). *Numerical recipes in C*. Second Edition. 994 pp. New York City: Cambridge University Press.
- Sandwell, D.T. and E.J. Price (1998). "Phase gradient approach to stacking interferograms". In: *J. Geophys. Res.* 103, pp. 30183–30204.
- Sneed, M. and J. Brandt (2007). *Detection and Measurement of Land Subsidence Using GPS Surveying and InSAR, Coachella Valley, California, 1996-2006*. Tech. rep. 2007-5251. New York City: USGS Scientific Investigations Report.

- Sneed, M., J. Brandt, and M. Solt (2014). *Land subsidence, groundwater levels, and geology in the Coachella Valley, California, 1993-2010*. Tech. rep. US Geological Survey.
- Swarztrauber, P.N. (1982). *Vectorizing the FFTs, in Parallel Computations (G. Rodrigue, ed.)* Cambridge, MA: Academic Press, pp. 51–83.
- Wessel, P. and W.H.F. Smith (1998). “New, improved version of Generic Mapping Tools released”. In: *EOS Trans. Amer. Geophys. U.* 79(47). 579 pp.
- Wessel, P., W.H.F. Smith, et al. (2013). “Generic Mapping Tools: Improved version released”. In: *EOS Trans. Amer. Geophys. U.* 94, pp. 409–410.

## 4 Problems

1. Precise orbital information is used in 4 areas of InSAR processing. Describe the 4 uses.
2. The natural coordinates of a radar image have range or time along one axis and azimuth or slow time along the other axis. Why is the term slow time used?
3. Describe an algorithm to transform a point on the surface of the earth (longitude, latitude, elevation) into radar coordinates.
4. When a SAR image is focussed at zero Doppler, the radar coordinates of a point reflector correspond to the minimum range. Why? Derive the equations (4) and (5) for adjusting the range and azimuth coordinates when an image is focussed at a non-zero Doppler.
5. GMTSAR uses a quadratic function to approximate the changes in baseline (horizontal and vertical) along the image frame. The quadratic formula is:

$$B(s) = a + bs + cs^2$$

where  $s$  is slow time ranging from the start to the end of the frame  $[0, T]$ . Suppose the actual baseline is measured at three times along the frame  $0, \frac{T}{2}, T$  and the values are  $B_1, B_2, B_3$ . Derive an expression for the parameters  $a, b, c$ . The forward model is

$$\begin{pmatrix} B_1 \\ B_2 \\ B_3 \end{pmatrix} = \begin{pmatrix} 1 & 0 & 0 \\ 1 & \frac{T}{2} & \frac{T^2}{4} \\ 1 & T & T^2 \end{pmatrix} \begin{pmatrix} a \\ b \\ c \end{pmatrix}$$

6. Satellite orbital information is commonly provided as state vectors of position and velocity at regular intervals (e.g., 1 minute). Hermite polynomial interpolation is often used to interpolate the orbit to the full sampling rate of the radar (e.g., 2000 Hz). What are the strengths and weaknesses of this approach? (This may require a literature search.)
7. Explain the terminology, master and slaves, reference and repeat.

# A Principles of Synthetic Aperture Radar

## A.1 Introduction

Synthetic aperture radar (SAR) satellites collect swaths of side-looking echoes at a sufficiently high range resolution and along-track sampling rate to form high resolution imagery (see Figure A1). As discussed in this appendix, the range resolution of the raw radar data is determined by the pulse length (or  $1/\text{bandwidth}$ ) and the *incidence angle*. For real aperture radar, the along-track or *azimuth* resolution of the outgoing microwave pulse is diffraction limited to an angle corresponding to the wavelength of the radar (e.g. 0.05 m) divided by the length of the aperture (e.g. 10 m). When this beam pattern is projected onto the surface of the earth at a range of say 850 km, it illuminates 4250 m in the along-track dimension so the raw radar data are horribly out of focus in azimuth. Using the synthetic aperture method, the image can be focused on a point reflector on the ground by coherently summing thousands of consecutive echoes thus creating a synthetic aperture perhaps 4250 m long. Proper focus is achieved by summing the complex numbers along a constant range. The focused image contains both amplitude (backscatter) and phase (range) information for each pixel.

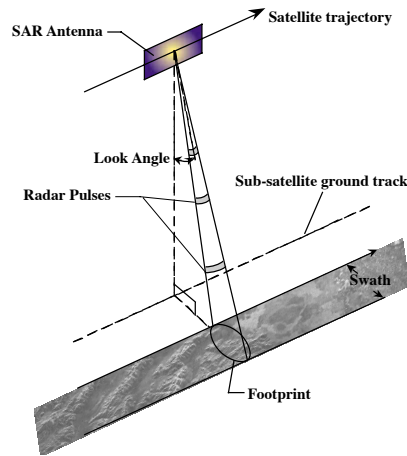


Figure A1: Schematic diagram of a SAR satellite in orbit. The SAR antenna has its long axis in the flight direction also called the *azimuth* direction and the short axis in the *range* direction. The radar sends pulses to one side of the *ground track* that illuminate the earth over a large elliptical footprint. The reflected energy returns to the radar where it is recorded as a function of *fast time* in the range direction and *slow time*, or echo number, in the azimuth direction.

## A.2 Fraunhofer diffraction

To understand why a synthetic aperture is needed for microwave remote sensing from orbital altitude one must understand the concepts of diffraction and resolution. Consider the projection pattern of coherent radiation after it passes through an aperture (see Figure A2). First we'll consider a 1-D aperture and then go on to a 2-D rectangular aperture to simulate a rectangular SAR antenna. The 2-D case provides the shape and dimension of the footprint of the radar. Although we will develop the resolution characteristics of apertures as transmitters of radiation, the resolution characteristics are exactly the same when the aperture is used to receive radiation. These notes were developed from Rees 2001 and Bracewell 1978.

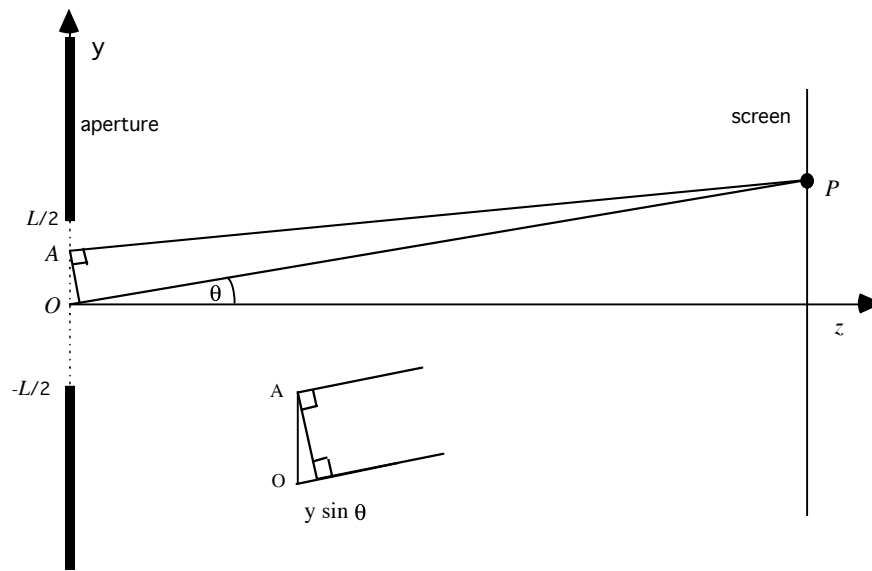


Figure A2: Diagram for the projection of coherent microwaves on a screen that is far from the aperture of length  $L$ .

We simulate coherent radiation by point sources of radiation distributed along the aperture between  $-L/2$  and  $L/2$ . For simplicity we'll assume all the sources have the same amplitude, wavelength  $\lambda$ , and phase. Given these sources of radiation, we solve for the illumination pattern on the screen as a function of  $\theta$ . We'll assume that the screen is far enough from the aperture so that rays  $AP$  and  $OP$  are parallel. Later we'll determine how far away the screen needs to be in order for this approximation to hold. Under these conditions, the ray  $AP$  is slightly shorter than the ray  $OP$  by an amount  $-y \sin \theta$ . This corresponds to a phase shift of  $\frac{-2\pi}{\lambda} y \sin \theta$ . The amplitude of the illumination at point  $P$  is the integral over all of the sources along the aperture

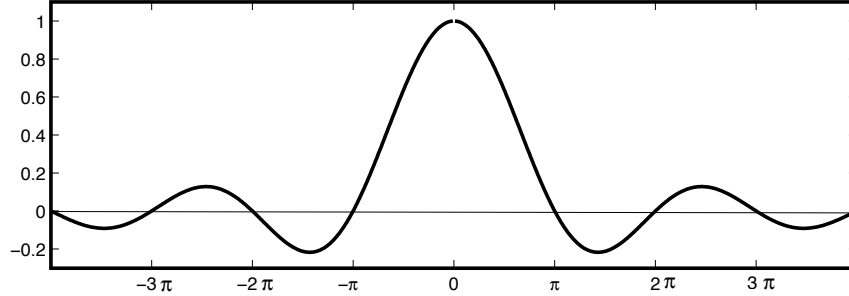


Figure A3: Sinc function illumination pattern for the aperture shown in Figure A2.

multiplied by their complex phase value

$$P(\theta) = \int_{-L/2}^{L/2} A(y)e^{-i2\pi yk \sin \theta} dy \quad (\text{A1})$$

where  $k = 1/\lambda$ . This is called the Fraunhofer diffraction integral. The illumination across the aperture is uniform in both amplitude and phase so we set  $A(y) = 1$ . Now let  $s = 2\pi k \sin \theta$  so the fourier integral is easy to evaluate.

$$P(s) = \int_{-L/2}^{L/2} e^{-isy} dy = \frac{e^{-isL/2} - e^{isL/2}}{-is} = \frac{2}{s} \sin(sL/2) = L \text{sinc}(sL/2) \quad (\text{A2})$$

Replacing  $s$  with  $2\pi \sin \theta/\lambda$  we arrive at the final result.

$$P(\theta) = L \text{sinc}\left(\frac{L\pi \sin \theta}{\lambda}\right) \quad (\text{A3})$$

The illumination pattern on the screen is shown in Figure A3.

The first zero crossing, or angular resolution  $\theta_r$  of the sinc function occurs when the argument is  $\pi$  so  $\sin \theta_r = \frac{\lambda}{L}$  and for small angles  $\theta_r \cong \frac{\lambda}{L}$  and  $\tan \theta_r \cong \sin \theta_r$ . Note that one could modify the screen illumination by changing the strength of the illumination across the aperture. For example, a Gaussian aperture would produce a Gaussian illumination function on the screen. This would eliminate the sidelobes associated with the sinc function but it would also broaden the projection pattern. In addition, one could vary the phase along the aperture to shift the point of maximum illumination away from  $\theta = 0$ . Such a phased array aperture is used in some radar systems to continuously illuminate a feature as the satellite passed over it. This is called spotlight mode SAR and it is a favorite technique for military reconnaissance.

One can perform the same type of analysis with any 2-D aperture; many analytic examples are given in Figure 12.4 from Bracewell 1978. Below we'll be using a rectangular aperture when we discuss synthetic aperture radars. For now, consider a uniform circular aperture has an angular resolution given by  $\sin \theta_r = 1.22 \frac{\lambda}{L}$ .

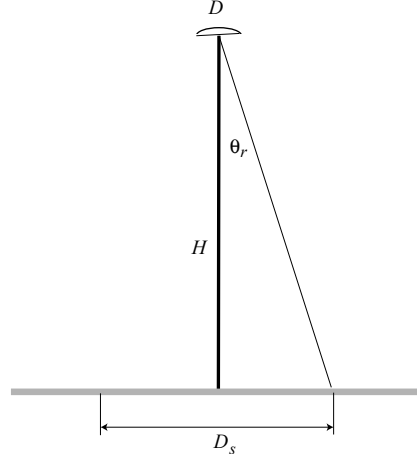


Figure A4: Beam-limited footprint  $D_s$  of a circular aperture (radar altimeter or optical telescope) at an altitude of  $H$ .

The Geosat radar altimeter orbits the Earth at an altitude of 800 km and illuminates the ocean surface with a 1-m parabolic dish antenna operating at Ku band (13.5 GHz,  $\theta = 0.022$  rad) (Figure A4). The diameter of the beam-limited footprint on the ocean surface is  $D_s = 2H \tan \theta_r \cong 2.44H \frac{\lambda}{D}$  or in this case 43 km.

An optical system with the same 1 m diameter aperture, but operating at a wavelength of  $\lambda = 5 \times 10^{-7}$  m, has a footprint diameter of 0.97 m. The Hubble space telescope reports an angular resolution of 0.1 arcsecond, which corresponds to an effective aperture of 1.27 m. Thus a 1-m ground resolution is possible for optical systems while the same size aperture operating in the microwave part of the spectrum has a 44,000 times worse resolution. Achieving high angular resolution for a microwave system will require a major increase in the length of the aperture.

Before moving on to the 2-D case, we should check the assumption used in developing the Fraunhofer diffraction integral that the rays  $AP$  and  $OP$  are parallel. Suppose we examine the case when  $\theta = 0$ ; the ray path  $AP$  is slightly longer than  $OP$  (Figure A5). This parallel-ray assumption breaks down when the phase of ray path  $AP$  is more than  $\pi/2$  radians longer than  $OP$  which corresponds to a distance of  $\frac{\lambda}{4}$ . Let's determine the conditions when this happens.

The condition that the path length difference is smaller than  $1/4$  wavelength is

$$\left[ \frac{L^2}{4} + z^2 \right]^{\frac{1}{2}} - z < \frac{\lambda}{4} \quad (\text{A4})$$

or can be rewritten as

$$\left[ \left( \frac{L}{2z} \right)^2 + 1 \right]^{\frac{1}{2}} - 1 < \frac{\lambda}{4z} \quad (\text{A5})$$

Now assume  $L \ll z$  so we can expand the term in bracket in a binomial series.

$$1 + \frac{L^2}{8z^2} - 1 < \frac{\lambda}{4z} \quad (\text{A6})$$

and we find  $z_f > \frac{L^2}{2\lambda}$  where  $z_f$  is the Fresnel distance. So when  $z < z_f$  we are in the near field and we need to use a more rigorous diffraction theory. However when  $z \gg z_f$  we are safe to use the parallel-ray approximation and the Fraunhofer diffraction integral is appropriate. Next consider some examples:

$$\text{Geosat:} \quad L = 1 \text{ m}, \lambda = 0.022 \text{ m} \quad z_f = 23 \text{ m}$$

At an orbital altitude of 800 km the parallel-ray approximation is valid.

$$\text{Optical telescope:} \quad L = 1 \text{ m}, \lambda = 5 \times 10^{-7} \text{ m} \quad z_f = 4000 \text{ km.}$$

So we see that an optical system with an orbital altitude of 800 km will require near-field optics.

What about a synthetic aperture radar (discussed below) such as ERS with a 4000 m long synthetic aperture?

$$\text{ERS SAR:} \quad L = 4000 \text{ m}, \lambda = 0.058 \text{ m} \quad z_f = 140,000 \text{ km.}$$

Thus near-field optics are also required to achieve full SAR resolution for ERS. This near-field correction is done in the SAR processor by performing a step called range migration and it is a large factor in making SAR processing so CPU-intensive.

### A.3 2-D Aperture

A 2-D rectangular aperture is a good approximation to a typical spaceborne strip-mode SAR. The aperture is longer in the flight direction (length  $L$ ) than in the flight perpendicular direction (width  $W$ ) as shown in Figure A6. As in the 1-D case, one uses a 2-D Fraunhofer diffraction integral to calculate the projection pattern of the antenna. The integral is

$$P(\theta_x, \theta_y) = \int_{-L/2}^{L/2} \int_{-W/2}^{W/2} A(x, y) \exp\left[i\frac{2\pi}{\lambda}(x \sin \theta_x + y \sin \theta_y)\right] dx dy \quad (\text{A7})$$

where  $\lambda$  is the wavelength of the radar. As in the 1-D case we'll assume the aperture  $A(x, y)$  has uniform amplitude and phase. In this case the projection pattern can be

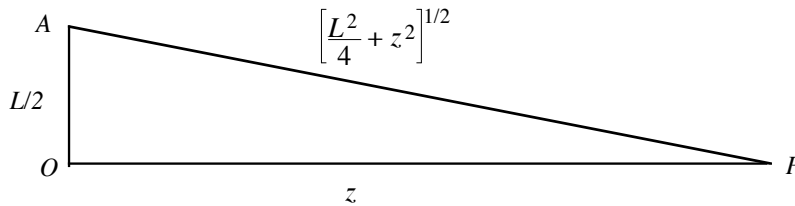


Figure A5: Diagram showing the increases length of path AP with respect to OP due to an offset of  $L/2$ .

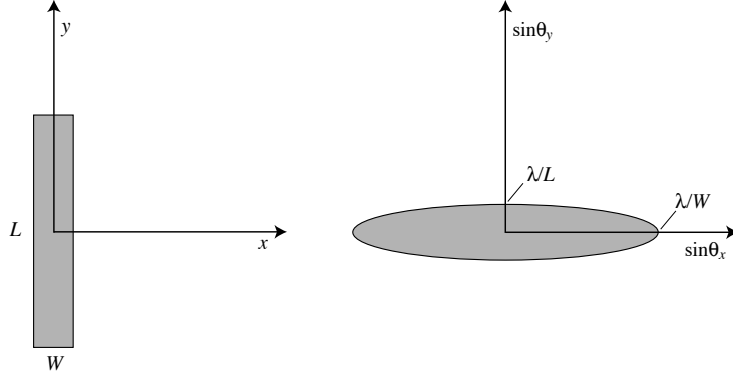


Figure A6: Diagram showing the projection pattern (right) for a rectangular SAR antenna (left).

integrated analytically and is

$$P(\theta_x, \theta_y) = LW \operatorname{sinc}\left(\frac{\pi W \sin \theta_x}{\lambda}\right) \operatorname{sinc}\left(\frac{\pi L \sin \theta_y}{\lambda}\right). \quad (\text{A8})$$

The first zero crossing of this 2-D sinc function is illustrated in Figure A6 (right).

The ERS radar has a wavelength of 0.05 m, an antenna length  $L$  of 10 m, and an antenna width  $W$  of 1 m. For a nominal look angle of  $23^\circ$  the slant range  $R$  is 850 km. The footprint of the radar has an along-track dimension  $D_a = 2R\lambda/L$ , which is 8.5 km. As discussed below this is approximately the length of the synthetic aperture used in the SAR processor. The footprint in the range direction is 10 times larger or about 85 km.

#### A.4 Range resolution (end view)

The radar emits a short pulse that reflects off the surface of the earth and returns to the antenna. The amplitude versus time of the return pulse is a recording of the reflectivity of the surface. If adjacent reflectors appear as two distinct peaks in the return waveform then they are resolved in range. The nominal *slant range resolution* is  $\Delta r = C\tau/2$  where  $\tau$  is the pulse length,  $C$  is the speed of light and  $\theta$  is the look angle. The factor of 2 accounts for the 2-way travel time of the pulse. Figure A7 shows how the *ground range resolution* is geometrically related to the slant range resolution  $R_r = \frac{C\tau}{2 \sin \theta}$ .

Note the ground range resolution is infinite for vertical look angle and improves as look angle is increased. Also note that the range resolution is *independent of the height* of the spacecraft  $H$ . The range resolution can be improved by increasing the bandwidth of the radar. Usually the radar bandwidth is a small fraction of the carrier frequency so shorter wavelength radar does not necessarily enable higher range resolution. In

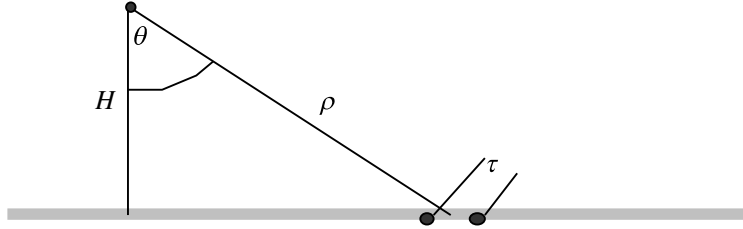


Figure A7: Diagram of radar flying into the page emitting a pulse of length  $\rho$ . That reflects from two points on the surface of the earth.

many cases the bandwidth of the radar is limited by the speed at which the data can be transmitted from the satellite to a ground station.

### A.5 Azimuth resolution (top view)

To understand the azimuth resolution, consider a single point reflector on the ground that is illuminated as the radar passes overhead (Figure A8). From the Fraunhofer diffraction analysis we know the length of the illumination (twice the angular resolution) is related to the wavelength of the radar divided by the length of the antenna. As discussed above the along-track dimension of the ERS footprint is 8.5 km so the nominal resolution  $R_a$  is 4.25 km, which is very poor. This is the azimuth resolution of the *real-aperture radar*

$$R_a = \rho \tan \theta_r \cong \frac{\rho \lambda}{L} = \frac{\lambda H}{L \cos \theta} \quad (\text{A9})$$

where  $L$  is the length of radar antenna,  $\rho$  is the slant range, and  $\lambda$  is the wavelength of the radar.

If the scatterer on the ground remains stationary as the satellite passes overhead, then one can assemble a synthetic aperture with a length equal to the along-track beamwidth of length which is  $2R_a$ . This much longer aperture of 8.5 km results in a dramatic improvement in azimuth resolution given by

$$R'_a = \frac{\lambda \rho}{2R_a} = \frac{L}{2} \quad (\text{A10})$$

which is the theoretical resolution of a *strip-mode SAR*. Note the synthetic aperture azimuth resolution is *independent of spacecraft height* and improves as the antenna length is *reduced*. One could form a longer synthetic aperture by steering the transmitted radar beam so it follows the target as the spacecraft (aircraft) flies by. This is called *spotlight-mode SAR*.

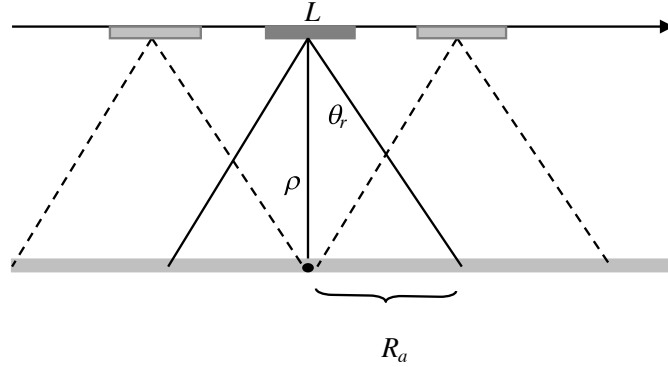


Figure A8: Top view of SAR antenna imaging a point reflector. The reflector remains within the illumination pattern over the real aperture length of  $2R_a$ .

## A.6 Range and Azimuth Resolution of ERS SAR

The ERS SAR has a bandwidth of 15.6 MHz, an antenna length of 10 m and a look angle of  $23^\circ$ . Accordingly the ground range resolution is about 25 m and the maximum azimuth resolution is 5 m. In practice, one averages several “looks” together to improve the quality of the amplitude (backscatter) image. In the case of ERS, one could average 5 looks for a resolution cell of 25 m by 25 m.

## A.7 Pulse repetition frequency

The discussion above suggests that we should make the antenna length  $L$  as short as possible to improve azimuth resolution. However, to form a complete aperture without aliasing longer wavelengths back into shorter wavelengths we must pulse the radar at an along-track distance of  $L/2$  or shorter. To understand why such a rapid pulse rate is necessary, consider the maximum Doppler shift from a point that is illuminated at a maximum distance ahead of the radar (Figure A9) where  $\nu_o$  is the carrier frequency  $= C/\lambda$  and  $V$  is the velocity of spacecraft relative to the ground.

The maximum Doppler shift occurs at a maximum angle of

$$\sin \theta_a = \frac{\lambda}{L}$$

$$\Delta\nu = 2\nu_o \frac{V}{C} \sin \theta_a = \frac{2C}{\lambda} \frac{V}{C} \frac{\lambda}{L} = \frac{2V}{L}$$
(A11)

This corresponds to a maximum along-track distance between samples of  $L/2$ . For ERS this corresponds to a minimum pulse repetition frequency (PRF) of 1400 Hz. The actual PRF of ERS is 1680 Hz.

## A.8 Other constraints on the PRF

The PRF cannot be too large or the return pulses from the near range and far range will overlap in time as shown in Figure A10.

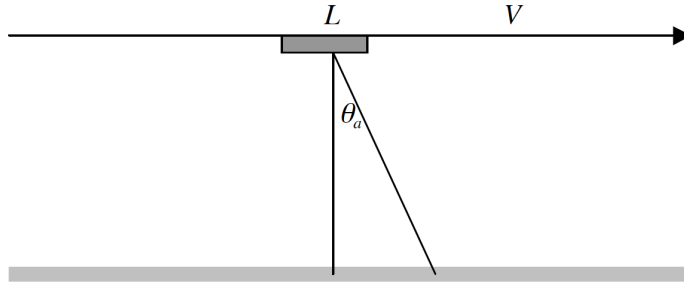


Figure A9: Diagram showing the angle between broadside to the antenna and the point where a reflector first enters the illumination of the antenna.

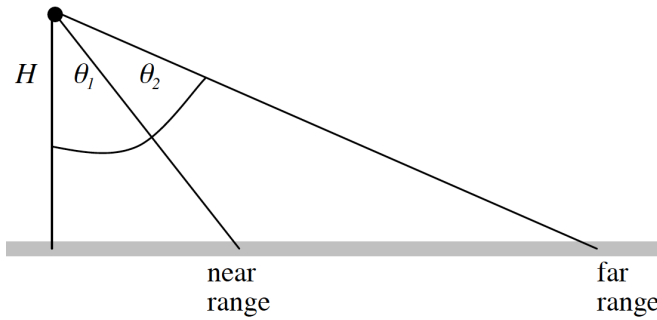


Figure A10: End view of the distance to the near range and far range of the radar illumination pattern.

$$\begin{aligned}
 PRF &< \frac{1}{t_2 - t_1} \\
 t_1 &= \frac{2H}{C \cos \theta_1} & t_2 &= \frac{2H}{C \cos \theta_2} \\
 \Delta t &= \frac{2H}{C} (\sec \theta_2 - \sec \theta_1) \\
 \frac{2V}{L} &< PRF < \frac{C}{2H} (\sec \theta_2 - \sec \theta_1)^{-1}
 \end{aligned} \tag{A12}$$

For ERS the look angles to the rear range and far range are  $18^\circ$  and  $24^\circ$ , respectively. Thus the maximum PRF is 4777 Hz. The actual PRF of 1680 is safely below this value and the real limitation is imposed by the speed of the data link from the spacecraft to the ground. A wider swath or a higher PRF would require a faster data link than is possible using a normal X-band communication link of 105 Mbps.

## References

- Bracewell, R.N. (1978). *The Fourier Transform and Its Applications*. Second Edition. New York City: McGraw-Hill Book Co.
- Curlander, John C. and Robert N. McDonough (1991). *Synthetic Aperture Radar: Systems and Signal Processing*. Chapter 4. John Wiley & Sons.
- Rees, W.G. (2001). *Physical Principles of Remote Sensing*. Cambridge, UK: Cambridge University Press.

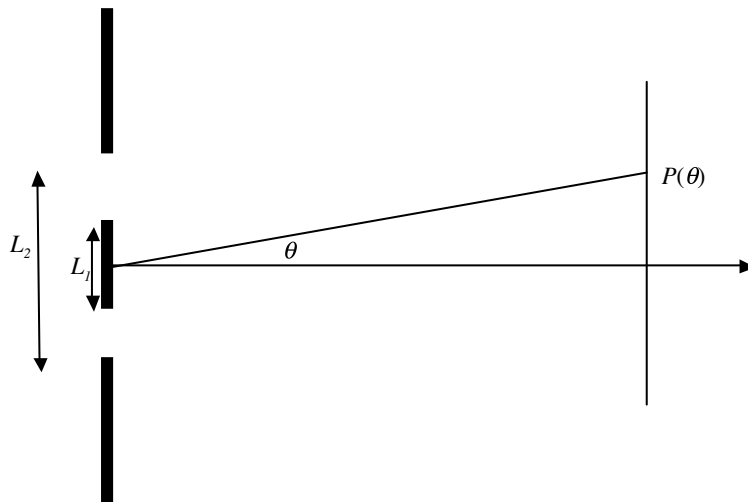
## A.9 Problems

1. What is the illumination pattern for an aperture with a sign reversal at its center? What is  $P(0)$ ? Is the function real or imaginary? Is the function symmetric or asymmetric?

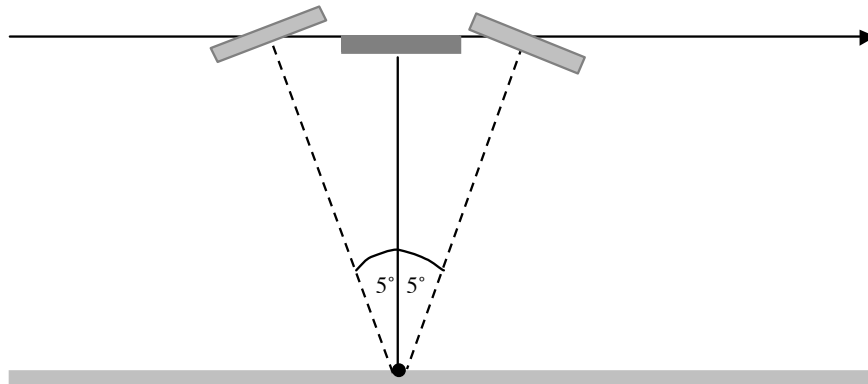
The aperture is

$$A(y) = \begin{cases} 0 & |y| > \frac{L}{2} \\ 1 & 0 < y \leq \frac{L}{2} \\ -1 & -\frac{L}{2} \leq y < 0 \end{cases}$$

2. (a) What is the illumination pattern for the aperture below?  
(b) What is the illumination pattern in the limit as  $L_1$  approaches  $L_2$ ?



3. What is the theoretical azimuth resolution of a spotlight-mode SAR that can illuminate the target over a  $10^\circ$  angle as shown in the diagram below?



4. Derive the projection pattern for a 2-D rectangular aperture of length  $L$  and width  $W$  given in equation (A8).
5. What is the ground-range resolution of side-looking radar with a pulse length of  $6 \times 10^{-8}$ s and a look angle of  $45^\circ$ ?
6. (a) What is the period for a satellite in a circular orbit about the moon where the radius of the orbit is  $1.9 \times 10^6$  m? The mass of the moon is  $7.34 \times 10^{22}$  kg.  
 (b) You are developing a SAR mission for the moon. The length of your SAR antenna is 10 m. What minimum pulse repetition frequency is needed to form a complete aperture? The circumference of the moon is  $1.1 \times 10^7$  m. You will need the orbital period from problem (a).
7. Derive equation (A10).
8. A SAR with a 10 m long antenna is orbiting the earth with a ground speed of  $7000 \text{ ms}^{-1}$ . What is the maximum possible swath width. Use a look angle to the near range of  $45^\circ$  and assume the earth is flat.
9. CryoSat is a nadir-looking altimeter that uses a burst-mode synthetic aperture to reduce the length of the radar footprint in the along-track direction. The radar has a pulse repetition frequency of 18 kHz and uses 64 echoes in one burst to form the synthetic aperture. What is the along-track resolution of the footprint? What is the Fresnel distance for this configuration (ground track velocity  $7000 \text{ ms}^{-1}$ , 700 km altitude)?

## B SAR Image Formation

### B.1 Overview of the range-doppler algorithm

From Curlander and McDonough 1991. The basic SAR theory is conceptually simple (Appendix A) yet when one looks into the inner workings of the SAR processor it appears quite complicated. The most difficult part of the problem is related to the coupling between the azimuthal compression and the orbital parameters. In the old days when the satellite orbits were not known very accurately, one would use techniques such as *clutterlock* and *autofocus* to derive the orbital parameters from the data. This is no longer necessary with the high accuracy orbits available today. A standard processing sequence follows where the first two steps are done on board the satellite while the remaining 4 steps are done by the user with a digital SAR processor. The discussion provided here is for the ERS-1 satellite although the concepts translate to any modern strip-mode SAR satellite.

### B.2 Processing on board the satellite

*Demodulate* The electromagnetic wave consists of a chirp of bandwidth  $B$  ( $\sim 15$  MHz) superimposed on carrier frequency  $\omega_o$  ( $\sim 5$  GHz). To record the return signal, one could simply digitize the amplitude of the electric field  $E(t)$  at a sampling rate of 10 GHz using 1-byte encoding. However, this would generate 10 Gbytes of data every second! We are really only interested in how the chirp has been delayed and distorted by the reflection off the Earth's surface. The trick here is to use the shift theorem (Bracewell 1978, p. 108) to isolate the 15 MHz part of the spectrum containing the chirp. Suppose we multiply the signal  $E(t)$  by  $e^{i2\pi\omega_o t}$ . This will shift the Fourier transform of the signal as shown in Figure B1.

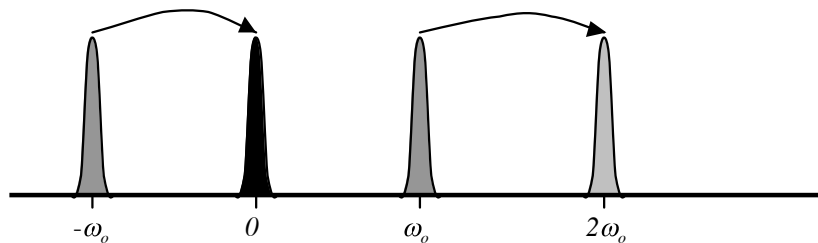


Figure B1: Diagram showing the power spectrum of the radar signal before and after shifting by the carrier frequency.

The function  $E(t)$  is a real-valued function so we know that its Fourier transform has Hermitian symmetry about the origin, that is  $E(-\omega) = E^*(\omega)$ . Because of this symmetry, all of the information in the time series is contained within the bandwidth

of a single spectral peak. Next we low-pass filter the signal to isolate the spectral peak centered at the zero frequency. The original signal  $E(t)$  was a real-valued function but after this shift/filter operation the output complex. No information is lost in this process and now the output can be digitized at the much lower rate of twice the bandwidth of the chirp (~30 MHz).

*Digitize* The complex signal is digitized at 5 bits per pixel so the numbers range from 0 to 31; the mean value is 15.5. Digitizing the data at 8 bits per pixel would seem more convenient but transmitting these extra 3 bits to the ground receiving station exceeds the bandwidth of the telemetry so every effort is made to compress the data before transmission. Once the data are on the ground they are expanded to 8 bits (one byte) for programming convenience. Engineers refer to the real and imaginary parts of the signal as the in-phase (I) and quadrature (Q) components. The raw signal files contain rows of (11644 bytes) that represent a single radar echo (Figure B2). The first 412 bytes are timing and other information while the remaining 11232 bytes contain the 5616 complex numbers of raw signal data.

### Raw Signal Data

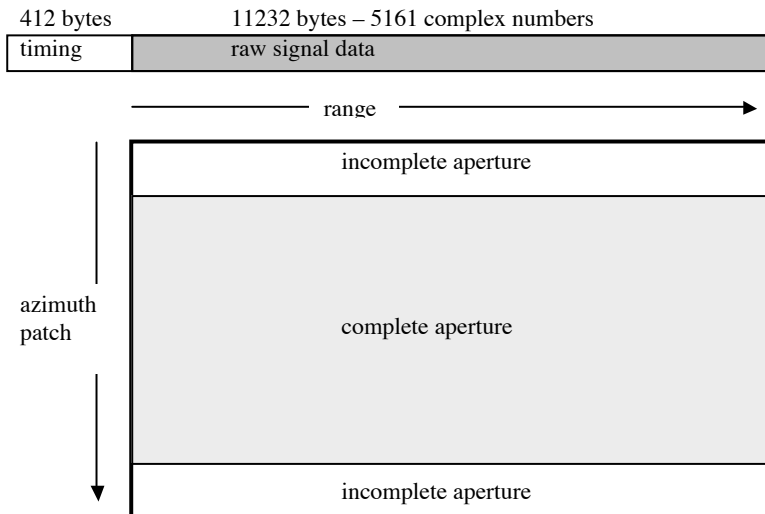


Figure B2: Raw signal data

### B.3 Digital SAR processing

The digital SAR processor is a computer program that converts the raw signal data into a single-look complex (SLC) image. An overview is provided in Figure B3 this is followed by a detailed description of each step.

### Digital SAR Processing Overview

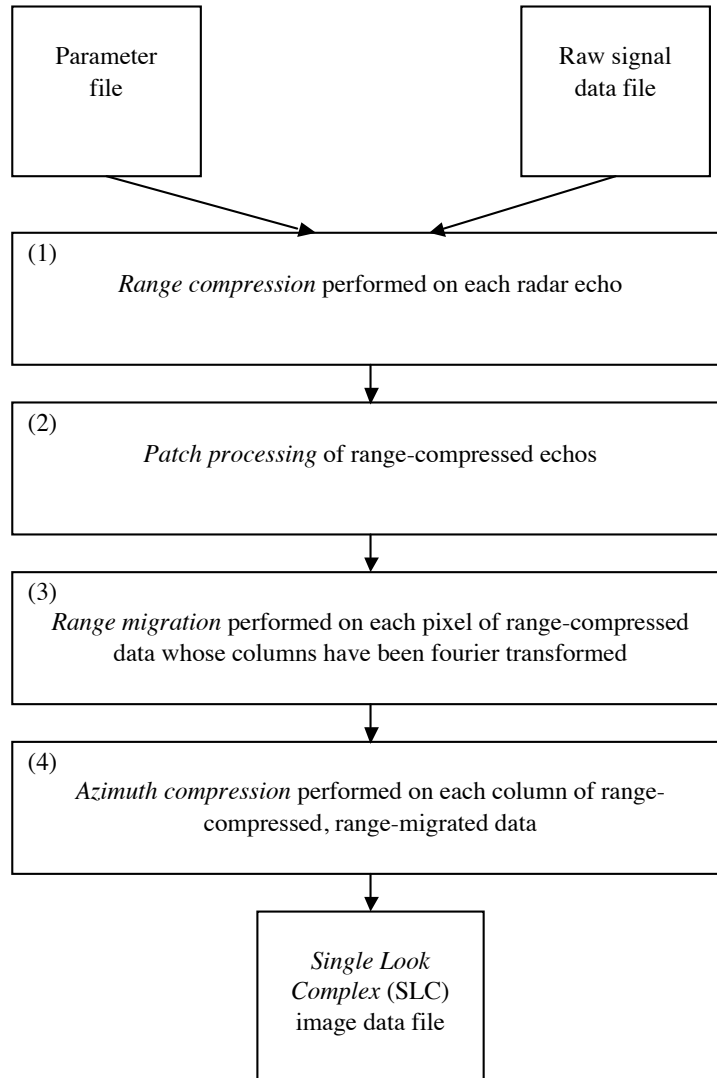


Figure B3: Digital SAR processing overview

Table B1: Example Parameter (PRM) file (e2\_10001\_2925.PRM)

<b>File information/format</b>			
input_file	e2_10001_2925.raw	name of raw data file	
SC_identity	2	(1) – ERS-1 or (2) – ERS-2	
bytes_per_line	11644	number of bytes in row of raw data	
first_sample	206	412 bytes of timing information to skip over	
fdl	248.115	Doppler centroid estimated from data	$f_{Dc}$
L_mean	15.5	mean value of real numbers	
Q_mean	15.5	mean value of imaginary numbers	
icu_start	2576039268.848	spacecraft clock for first sample	
SC_clock_start	1997078.767881851	UTC for first sample YYYYDD.DDDDDDDDD	
SC_clock_stop	1997078.768074699	UTC for last sample YYYYDD.DDDDDDDDD	
<b>Radar characteristics</b>			
PRF	1679.902394	pulse repetition frequency	$PRF$
rng_samp_rate	1.89625e+07	range sampling rate	$f_s$
chirp_slope	4.17788e+11	chirp slope	$k$
pulse_dur	3.712e-05	pulse duration	$\tau_p$
radar_wavelength	0.056666	radar wavelength	$\lambda$
<b>Orbital information</b>			
near_range	829924.365777	distance to first range bin	$R_{near}$
earth_radius	6371746.4379	earth radius 1/2 way into image	$R_e$
SC_height	787955.52	spacecraft height above the earth_radius	$H$
SC_vel	7125.0330	effective speed	$V_e$
<b>Processing information</b>			
num_valid_az	2800	size of patch to process	
num_patches	10	number of patches to process	
first_line	1		
deskew	n	deskew (yes or no)	
st_rng_bin	1	start processing at row number	
num_rng_bins	6144	number of range bins in output file	
chirp_ext	614	extend the chirp to process outside swath	
Flip_iq	n	exchange real and imaginary numbers (yes or no)	
nlooks	1	number of azimuth echoes to average	
<b>Image alignment</b>			
rshift	15.1	range shift to align image to master	
ashift	483.2	azimuth shift to align image to master	
stretch_r	.0014569	range stretch versus range	
stretch_a	-.0019436	azimuth stretch versus range	
a_stretch_r	0.0	range stretch versus azimuth	
a_stretch_a	0.0	azimuth stretch versus azimuth	

1. *Range Compression* A sharp radar pulse is recovered by deconvolution of the chirp. This is done with fast fourier transform. There are 5616 points in the ERS-1 signal data and the chirp is 703 points long. Both are zero-padded to a length of 8192 prior to deconvolution to take advantage of the speed of the radix-2 fft algorithms. Later we keep 6144 points, which enables one to extract the phase beyond the edges of the original swath. Since the chirp really did interact with the ground outside the digitized swath, this is not magic. The number 6144 has small prime factors that may be optimal for later 2-D fft phase unwrapping algorithms.
2. *Patch Processing* The next step is to focus the image in the along-track or azimuth direction. This is also done by fft, but now we need to process columns rather than rows. For the ERS radar, the synthetic aperture is 1296 points long so we need to read at least that many rows into the memory of the computer. Actually 4096 rows is better number since it is a power of 2. A typical ERS raw data file has 28,000 rows so we will need to process many of these *patches*. One problem with this approach is that the synthetic aperture is only complete for the inner 2800 points of the 4096 data patch so the patches must have a 1296-point overlap (Figure B3). A  $4096 \times 5616$  patch requires at least 184 Mbytes of computer memory for single precision real numbers. In the old days before this large memory space was available, each patch was transposed—*corner turning*—using high-speed disks so the data could be processed on a column-by-column basis. The L-band data from ALOS have a much longer synthetic aperture and patch size. Efficient processing of these data require a minimum of 2 Gbytes of computer memory.
3. *Range Migration* As we will see below, a point target will appear as a hyperbolic-shaped reflection as it moves through the synthetic aperture. In addition, there could be a pronounced linear drift due to an elliptical orbit and earth rotation. In other words, the target will migrate in range cell as a linear trend plus a hyperbola. The shape of this migration path is calculated from the precise orbital information and is approximated by a parabola. Prior to focusing the image along a single column, these signals must be migrated back to a constant range cell. This is called *range migration* and the fastest way to do this is by Fourier transforming the columns first. Each Fourier component corresponds to a unique Doppler shift and also a unique value of range migration; for an ideal radar, the first component will have zero Doppler and will correspond to the point on the earth that is perpendicular to the spacecraft velocity vector. The second component will have a small positive Doppler shift and a small migration of the range cells will be needed - and so on all the way through the positive and negative Doppler spectrum.
4. *Azimuth Compression* The final step in the processing is to focus the data in azimuth by accounting for the phase shift of the target as it moves through the aperture. In Appendix A, we calculated the illumination pattern on a screen due to the propagation of a coherent wave from the aperture to the screen. The azimuth compression relies on the same theory although we do the opposite calculation—

given the illumination pattern, calculate the shape of the aperture (reflectivity of the target). This is done by generating a second frequency-modulated chirp where the chirp parameters depend on the velocity of the spacecraft, the pulse repetition frequency (*PRF*), and the absolute range. The chirp is Fourier transformed into Doppler space and multiplied by each column of range-migrated data. The product is inverse Fourier transformed to provide the focused image.

*Single-Look Complex (SLC) Image* As described above, only the inner 2800 rows use the complete synthetic aperture so these are written to an output file (Figure B2). The file-reading pointer is moved back 1296 rows to start the processing of the next patch. Because complete apertures are used for each patch, they will abut seamlessly.

#### B.4 Range compression

To reduce the peak power of the radar transmitter associated with a short pulse, a long frequency-modulated chirp is emitted by the radar. This chirp propagates to the ground where it reflects from a swath typically 100 km wide. When it returns to the radar, the raw signal data consists of the complex reflectivity of the surface convolved with the chirp. Our objective is to recover the complex reflectivity by deconvolution of the chirp. As discussed above, this is the first step in the digital SAR processor. For the ERS-radar, the frequency-modulated chirp is

$$s(t) = e^{i\pi kt^2} \quad |t| < \tau_p/2. \quad (\text{B1})$$

where

- $k$  chirp slope ( $4.17788 \times 10^{11} s^{-2}$ )
- $\tau_p$  pulse duration ( $3.712 \times 10^{-5} s$  or  $\sim 11$  km long)
- $f_s$  range sampling rate ( $1.89625 \times 10^7 s^{-1}$ ).

An example of a portion of the chirp for the ERS- radar as well as its power spectrum and impulse response is shown below.

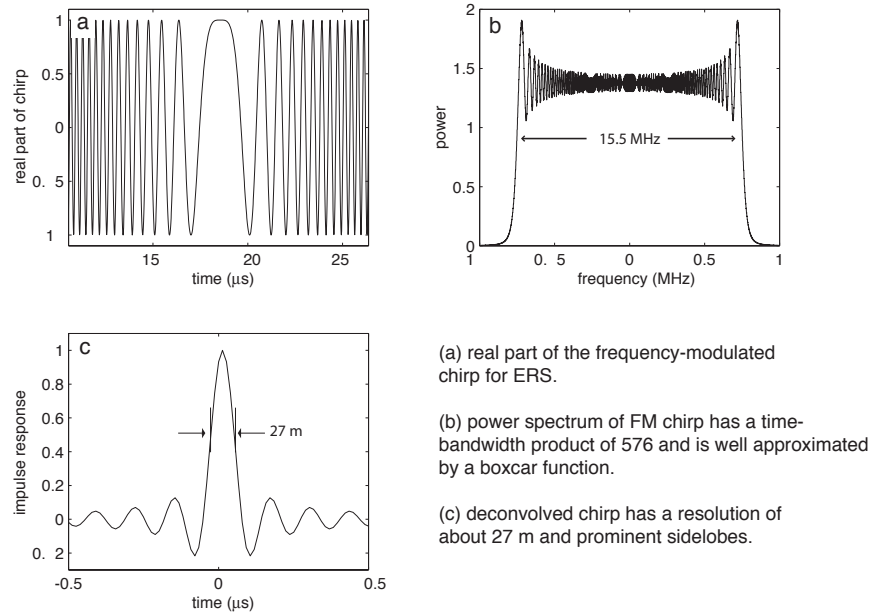


Figure B4: Chirp for ERS-1

The bandwidth of the chirp,  $B = k\tau_p$ , has a value of 15.5 MHz for the ERS radar. A matched filter is used to deconvolve the chirp from the data. In this case, the matched filter is simply the complex conjugate of the chirp or  $s^*(t) = e^{-i\pi kt^2}$ . The convolution of  $s^*(t)$  and  $s(t)$  is shown in Figure B4. The effective range resolution of the radar is about 27 m.

Using computer code and the radar parameters provided above, one can deconvolve the ERS chirp. The figure below is a small patch of ERS-2 data for an area around Pinon Flat, California (track 127, frame 2925, orbit 10001). This area contains two radar reflectors (Figure B5 and Table B2) spaced about 600 m apart that were installed in late 1996. The amplitude of the raw signal data appears as noise with a single horizontal streak due to missing data (Figure B5, left). The range-compressed data (right image) shows two vertical streaks due to the high reflectivity of the reflectors (red circles) as they migrate through the synthetic aperture.

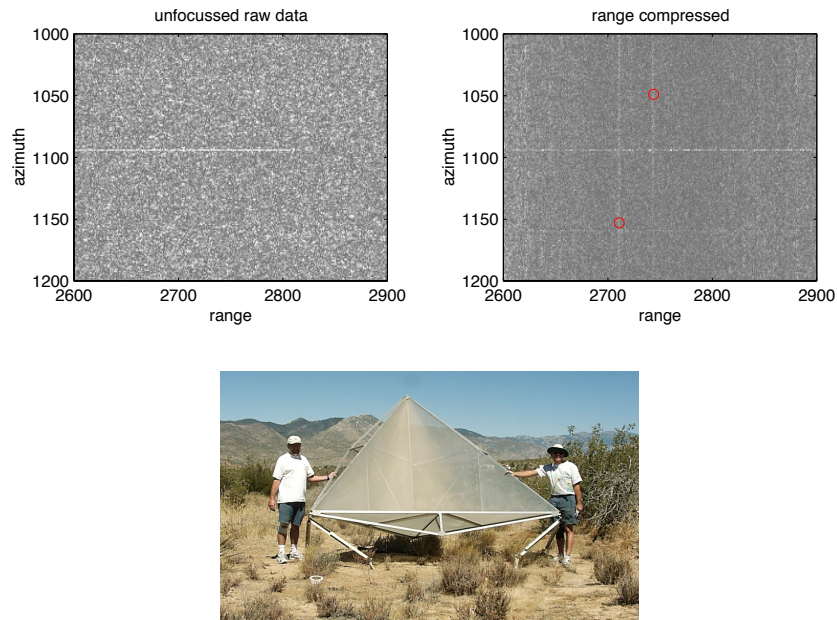


Figure B5: Raw ERS signal data (left) and range compressed data (right) for data over Pinon Flat California where two radar corner reflectors are installed (lower).

position			orientation	
<i>lat.</i>	<i>lon.</i>	<i>height</i>	<i>elev.</i>	<i>azi.</i>
33.612246	-116.456768	1258.990	39°	257.5°
33.612246	-116.457893	1257.544	39°	102.5°
33.607373	-116.451836	1254.537	39°	102.5°

Table B2: Coordinates of Radar Reflectors

Latitude and longitude in decimal degrees and height in meters relative to the WGS-84 coordinate system and ellipsoid. The survey point is the apex (lowest corner) of each reflector. There should be a correction for the offset between the phase center of the reflector and the apex.

## B.5 Azimuth compression

Azimuth compression or azimuth focusing involves coherent summation of echos at a constant range from the point reflector. The geometry of the strip-mode acquisition is shown in Figure B6.

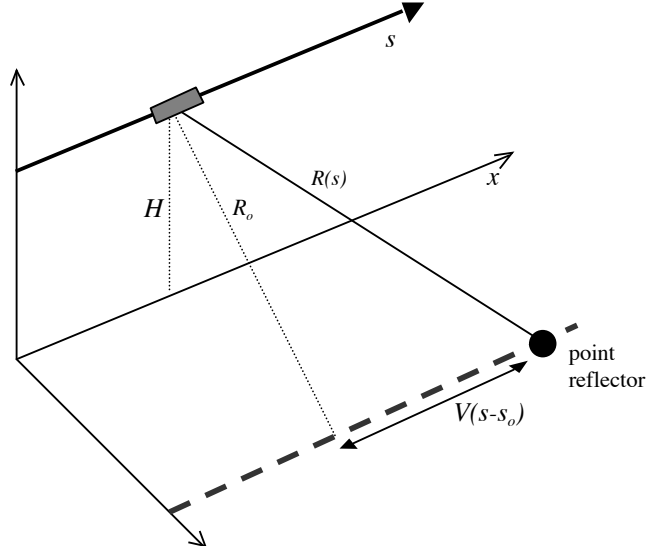


Figure B6: Geometry of radar passing over a point reflector where:

- $V_e$  the effective speed as discussed below
- $s$  slow time along the satellite track
- $s_o$  time when the center of the radar echo passes over the point reflector
- $R_o$   $R_{near} + n * (C/f_s)$  minimum range from the spacecraft to the target
- $R_{near}$  near range to first data sample in the swath

The range to the point reflector evolves with time as

$$R^2(s) = R_o^2 + V_e^2(s - s_o)^2. \quad (B2)$$

The complex phase of the return echo is

$$C(s) = \exp\left[-i \frac{4\pi}{\lambda} R(s)\right] \quad (B3)$$

The range versus slow time is approximately a hyperbola but for mathematical convenience we'll approximate this using a parabola

$$R(s) = R_o + \dot{R}(s - s_o) + \frac{\ddot{R}}{2}(s - s_o)^2 + \dots \quad (B4)$$

where the dot indicates derivative with respect to slow time,  $s$ . Curlander and McDonough [1991] discuss the accuracy of this polynomial approximation and it is also discussed below in terms of the ALOS SAR. The approximation is good enough for strip-mode SAR but may be inadequate for the much longer apertures associated with spotlight-mode SAR. Now we can write the phase of the return signal as a function

range, range rate, and range acceleration.

$$C(s) = \exp \left\{ -i \frac{4\pi}{\lambda} \left[ R_o + \dot{R}(s - s_o) + \ddot{R}(s - s_o)^2/2 \right] \right\} \quad (\text{B5})$$

It is more common to describe the parameters for focusing the SAR image as the Doppler centroid  $f_{Dc}$  and the Doppler frequency rate  $f_R$ . The relationships are:

$$f_{Dc} = \frac{-2\dot{R}}{\lambda} \quad \text{and} \quad f_R = \frac{-2\ddot{R}}{\lambda} \quad (\text{B6})$$

or

$$C(s) = \exp \left\{ -i \frac{4\pi R_o}{\lambda} \right\} \exp \left\{ i2\pi \left[ f_{Dc}(s - s_o) + f_R(s - s_o)^2/2 \right] \right\} \quad (\text{B7})$$

Note that this function is another frequency-modulated chirp where the parameters are the Doppler centroid and the Doppler frequency rate. An example of this azimuthal chirp function for the ERS orbit/radar as well as its power spectrum and impulse response are shown in Figure B7.

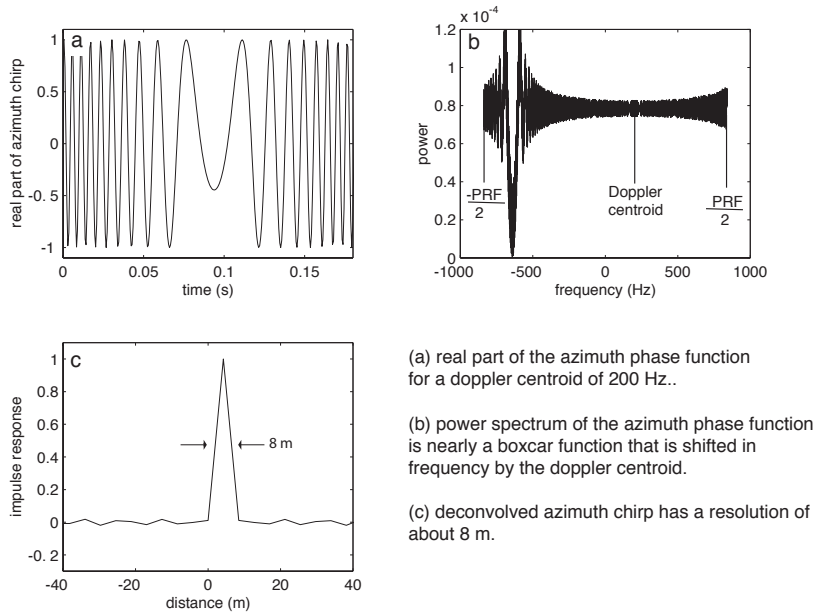


Figure B7: Azimuthal phase for the ERS-1 spacecraft.

The bandwidth of the azimuthal chirp is equal to the pulse repetition frequency (PRF = 1680 Hz). In this case the matched filter is simply the complex conjugate of the azimuthal phase function (B7) or  $C^*(s)$ .

*Doppler Centroid, Doppler Rate, and Effective Speed* Proper focus of the image requires accurate estimates of the three parameters given in (B5) and (B7). Actually

we only need to estimate two parameters because we will sweep through the range cells  $n$  in the raw data file and focus the image at each range  $R_o = R_{near} + n*(C/f_s)$  where  $C$  is the speed of light and  $f_s$  is the range sampling rate. Ideally the beam of the radar would be steered so that it is centered at a point on the ground where the range is minimum so the Doppler centroid is zero or at least small. We follow the approach of Madsen 1989 and calculate the Doppler centroid directly from the raw data file by computing the average change in phase between adjacent rows of the raw data file. This assumes that the Doppler centroid does not vary with slow time although it could vary slightly with increasing range. We use this estimated Doppler centroid to focus the image (or select a similar Doppler centroid that is closest to the mean of a stack of repeated SAR images).

Finally, as discussed below, the precise orbit (i.e., in earth fixed coordinates) can be used to calculate the third parameter, the range acceleration  $\ddot{R}$ . One approach would be to use the precise orbit to calculate range acceleration for each range but this is unnecessary because there is a good formula for range acceleration as a function of range that involves a parameter called the effective speed  $V_e$  of the spacecraft. Indeed the SAR processor code takes effective speed and converts this to  $\ddot{R}$  to focus the image. The derivation of the effective speed parameter follows. We start by taking the first derivative of the range versus slow time given in (B2)

$$\frac{\partial R^2(s)}{\partial s} = 2R\dot{R} = 2V_e^2 s \quad (\text{B8})$$

The second derivative is

$$\dot{R}\dot{R} + R\ddot{R} = V_e^2 \quad (\text{B9})$$

Next we assume that the radar antenna is oriented nearly perpendicular to the velocity vector of the satellite so  $\dot{R} \ll V_e$ . Note that to achieve interferometric coherence the radar beams of the reference and repeat images must overlap spatially which essentially requires that the Doppler centroid be less than half of the pulse repetition frequency (PRF). Given a typical PRF for a spaceborne SAR of 2000 and using equation (B6) and a wavelength of 0.05 m the range rate must be less than 25 m/s. This is much less than the typical spacecraft velocity of 7800 m/s so we can safely ignore the first term on the left hand side of (B9). So the approach is to use the precise orbit to calculate the range acceleration  $\ddot{R}$  at a single range  $R_o$  within the image. These two numbers are used to calculate the effective speed

$$V_e = \sqrt{R_o \ddot{R}} \quad (\text{B10})$$

Finally, this parameter is used by the SAR processing code to calculate the range acceleration

$$\ddot{R} = V_e^2 / R \quad (\text{B11})$$

at all the other ranges in the swath.

The effective speed, which is reported as SC\_vel in the PRF-file, can be used to compute the ground track speed  $V_g$  of the satellite as

$$V_g = \frac{V_e}{\left(1 + \frac{H}{R_e}\right)^{1/2}}. \quad (\text{B12})$$

where  $H$  is the height of the spacecraft and  $R_e$  is the local earth radius. Also note that  $V_g < V_e < V_s$  where  $V_s$  is the velocity of the spacecraft at orbital altitude. Using equation (B12), one can show that

$$V_e = \frac{V_s}{\left(1 + \frac{H}{R_e}\right)^{1/2}}. \quad (\text{B13})$$

Note this is only an approximate formula for computing the effective speed from the spacecraft velocity [Curlander and McDonough 1991]. For C-band radars such as ERS and ENVISAT the effective speed calculated from (B13) provides adequate focus for the SAR image. However, for L-band SARs such as ALOS, the aperture is much longer so other factors must be considered such as the curvature and ellipticity of the orbit.

We bypass this complexity by computing the effective speed from a polynomial fit of range versus time as discussed below but first we discuss the overlength of the synthetic aperture.

*Length of synthetic aperture* The length of the synthetic aperture  $L_a$  depends on the length of the radar ground footprint in the azimuth direction, which is approximately

$$L_a = R_o \frac{\lambda}{L} \quad (\text{B14})$$

where  $L$  is the physical length of the antenna,  $\lambda$  is the wavelength and  $R_o$  is the slant range given above. The length of the aperture in terms of radar echos is given by

$$n_a = \frac{L_a PRF}{V_e} \quad (\text{B15})$$

This is simply the length of the synthetic aperture divided by the along-track sampling distance. The following table provides these quantities for SARs of interest for interferometry today.

	$V_e$ (m/s)	$\lambda$ (m)	$PRF$ (Hz)	$R_o$ (km)	$L$ (m)	$L_A$ (m)	$n_a$ <i>theory</i>	$n_a$ <i>actual</i>
<b>ERS-1/2</b>	7125	0.057	1679	~850	10	4850	1142	1164
<b>Envisat</b>	7125	0.057	2067	~1020	10	5830	1690	1740
<b>ALOS</b>	7125	0.236	2159	~1020	9	26,830	8128	9216

Table B3: Length of synthetic aperture for three satellites.

*Focused image* Using the azimuth compression formulas and parameters provided above, one can focus the image in the azimuth direction. The figures below show the same small patch of ERS-2 data for an area of Pinon Flat, California. The range-compressed data (left image) shows two vertical streaks due to the high reflectivity of the reflectors (red circles) as they migrate through the synthetic aperture. The fully focused image (right) shows the point-like reflectivity associated with the two radar reflectors.

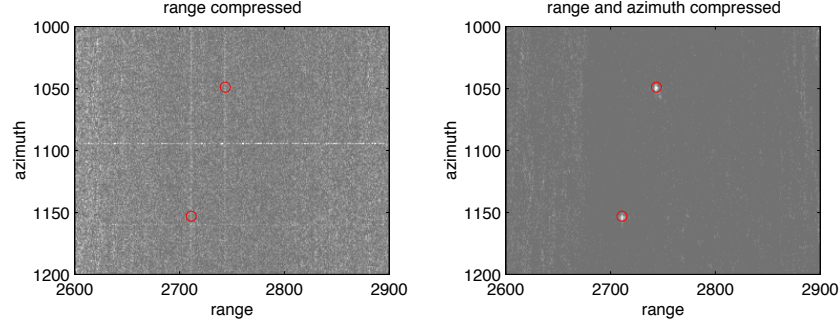


Figure B8: Range compressed (left) and fully focussed image (right). The two bright reflectors are 3-m corner cubes at Pinon Flat observatory. These were deployed in 1996 and therefore provide stable calibration points for ERS-1, ERS-2, Envisat, ALOS and all future satellites.

*Estimating  $\ddot{R}$  when a precise orbit is available* Estimation of the range acceleration from the orbit seems conceptually trivial although there is one complication that requires a bit of geometry. The complication is to find a point on the surface of the earth, at a prescribed range, and convert that location to Cartesian coordinates. Consider the following three vectors which form a triangle:

- $\vec{R}_s$  the vector position of the satellite in the Earth-fixed coordinate system;
- $\vec{R}_e$  the vector position of a point scatterer on the Earth and somewhere in the SAR scene;
- $\vec{R}_o$  the line-of-sight vector between the satellite and the point scatterer.

The three vectors form a triangle such that  $\vec{R}_e = \vec{R}_s + \vec{R}_o$  (Figure B9). The scalar range, which is a function of slow time, is given by

$$R(s) = \left| \vec{R}_s(s) - \vec{R}_e \right| \cong R_o + \dot{R}_o(s - s_o) + \frac{\ddot{R}_o}{2}(s - s_o)^2 + \dots \quad (\text{B16})$$

Measurements of scalar range versus slow time can be used to estimate the coefficients of the parabolic approximation. The algorithm is to:

1. Use the precise orbit to calculate the position vector of the satellite and compute a time series  $R(s)$  over the length of the aperture.
2. Perform a least-squares parabolic fit to this time series to estimate  $R_o, \dot{R}_o, \ddot{R}_o$ .
3. Compute the effective speed as  $V_e^2 = R_o \ddot{R}_o$ .

The only remaining step is to calculate the position of the point target  $\vec{R}_e = \vec{R}_s + \vec{R}_o$ . Actually this can be any point in the image so the selection criteria is that the point lie at the proper radius of the surface of the Earth  $R_e = \left| \vec{R}_e \right|$  and the  $\vec{R}_o$  vector is perpendicular to the velocity vector of the satellite  $\vec{V}$ . If we prescribe the length of the  $R_o$ - vector

then the angle between the satellite position vector and the line-of-sight vector is given by the law of cosines as shown in Figure B9.

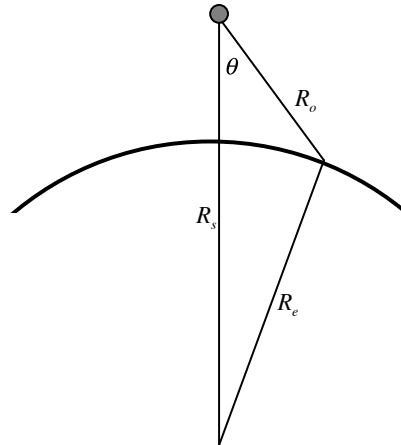


Figure B9: Triangle of earth radius, satellite radius and range to a point on the surface of the earth used to compute look angle  $\theta$ .

This diagram has the satellite at the gray dot with the velocity vector pointing into the page. The cosine of the look angle is

$$\cos \theta = \frac{(R_s^2 + R_o^2 - R_e^2)}{2R_s R_o} \quad (\text{B17})$$

Next consider a local co-ordinate system where the  $q_2$  axis is aligned with the velocity vector of the satellite as shown in the following diagram.

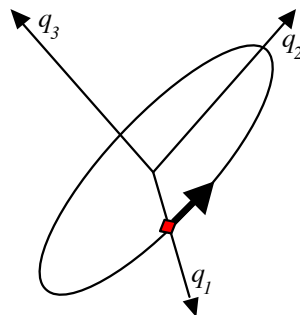


Figure B10: Satellite (red) in circular inclined orbit about the Earth.

In this coordinate system, the  $q_1$ - axis is parallel to  $\vec{R}_s$ , the  $q_2$  axis is parallel to  $\vec{V}$ , and the  $q_3$  axis is perpendicular to both and is given by their cross product

$$q_3 = \frac{\vec{R}_s}{|\vec{R}_s|} \times \frac{\vec{V}}{|\vec{V}|} \quad (\text{B18})$$

The following diagram has the velocity vector of the satellite going into the page and aligned with the  $q_2$  coordinate. The  $q_1$  vector is the radial vector from the center of the earth. The line-of-sight right-look vector is in the  $q_1$ - $q_3$  plane as shown in the diagram.

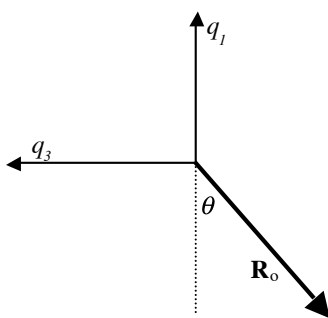


Figure B11: Diagram of satellite-fixed coordinate system where  $q_1$  is the vector from the center of the earth to the spacecraft,  $q_2$  is parallel to the velocity vector of the SC. The bold vector is the look vector of the radar where  $\theta$  is the look angle.

After going through this geometry we find the line of sight (LOS) vector to a point on the surface of the earth at the prescribed range for a right-looking radar is

$$\vec{R}_o = R_o \begin{pmatrix} -\cos \theta \hat{q}_1 & 0 \hat{q}_2 & -\sin \theta \hat{q}_3 \end{pmatrix} \quad (\text{B19})$$

and for a left-looking radar is

$$\vec{R}_o = R_o \begin{pmatrix} -\cos \theta \hat{q}_1 & 0 \hat{q}_2 & \sin \theta \hat{q}_3 \end{pmatrix} \quad (\text{B20})$$

## B.6 Example with ALOS L-band orbit

Now that we have an algorithm for finding a point on the surface of the Earth that is within the SAR scene, we can compute the time-evolution of the range to that point as the satellite orbits above the rotating Earth. We consider data from a descending orbit over Koga Japan where three radar reflectors have been deployed. The image is a fine-beam, single polarization having a nominal look angle of 34.3 degrees. A Hermite polynomial interpolation was used to calculate the x-y-z position of the satellite from 28 position and velocity vectors spaced at 60-second intervals. Thus the entire arc is 28 minutes or a quarter on an orbit. The accuracy of the Hermite interpolator was checked by omitting a central point and performing an interpolation using 6 surrounding points.

The accuracy of the interpolation was found to be better than 0.2 mm suggesting that the 60-s interval provides an accurate representation of the orbital arc.

Next we compute the range to the ground point as a function of time before and after the perpendicular LOS vector  $\vec{R}_o$ . We used a before/after time interval of 3 seconds which is about twice the length of the synthetic aperture for ALOS. A second-order polynomial was fit to the range versus time function and the three coefficients provide estimates of  $R_o$ ,  $\dot{R}_o$ , and  $\ddot{R}_o$ . The range versus time, as well as the residual of the fit, are shown below. One can learn a great deal from this exercise.

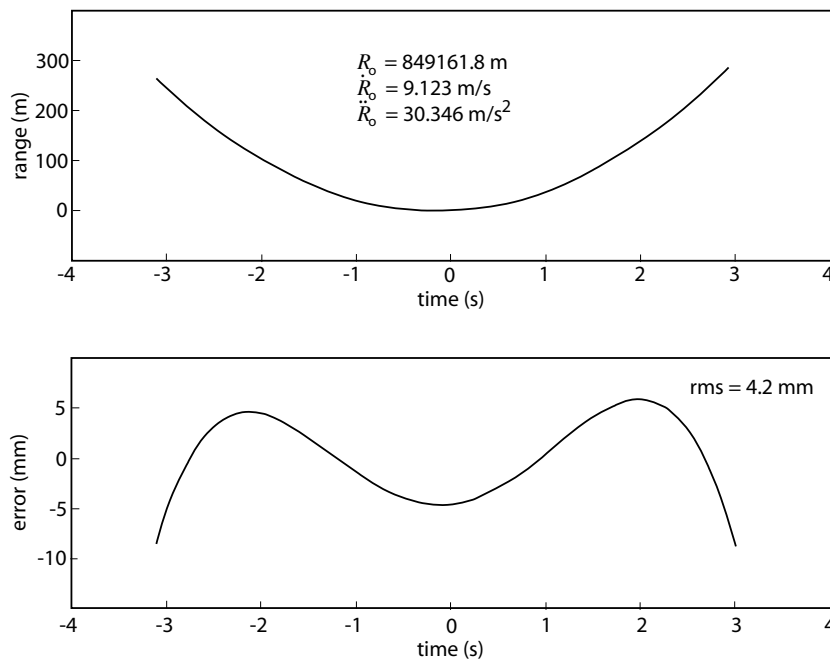


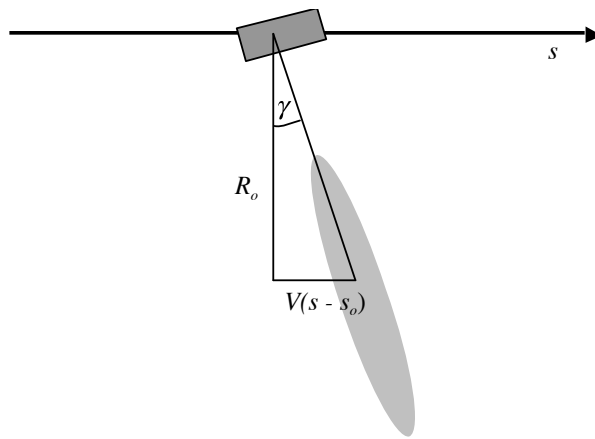
Figure B12: (upper) range versus slow time for ALOS for a 6 second aperture. The actual aperture is 4.2 seconds (Table B3). (lower) deviation from a parabolic fit to this range vs. time function.

1. The first thing learned is that the parabolic approximation to a hyperbola used in the SAR processor has a maximum error of about 1 cm at a time offset of 3 seconds. This corresponds to a small fraction of the 23-cm wavelength. Note that the actual aperture length for ALOS is only  $\pm 2.1$  seconds so this approximation is justified.
2. The range at zero offset has an error of  $-0.24 \text{ m}$ . This is due to approximating the shape of the earth as a sphere having a local radius given by the WGS84 ellipsoid formula. In other words there is a small error in the LOS vector because

it intersects the surface of the Earth at a latitude that is slightly different from the spacecraft latitude so the earth radii will differ slightly.

3. The Doppler shift when the satellite is perpendicular to the target can be calculated from the range rate coefficient using equation (B6).
4. Finally the range acceleration can be used to calculate the effective speed of the satellite  $V_e^2 = R_o \ddot{R}_o$ . For this example we arrive at a speed of 7174 m/s. By trial and error we found the optimal focus parameter corresponds to a speed between 7173 and 7183 so this new estimate is accurate. The simple spherical orbit ground speed approximation (B13) yields an estimate of 7208 m/s which provides poor focus.

*Squint angle* - Finally lets examine the quantity,  $\frac{V(s-s_o)}{R_o}$ . This is related to something called the squint angle,  $\gamma$ , as shown in the following diagram.



The squint angle is simply

$$\gamma = \tan^{-1} \left( \frac{V(s - s_o)}{R_o} \right) \quad (\text{B21})$$

For the ERS, ENVISAT and ALOS satellites, the squint angle is adjusted so the zero Doppler occurs roughly in the center of the antenna beam pattern. If the satellite orbit was circular and the earth was a non-rotating sphere, then the zero Doppler would correspond to a zero squint angle.

For interferometry it is important that the beam patterns of the reference and repeat orbits have a large overlap (>50%) at a given along-track spacecraft position. The requirement is that the Doppler centroid of the reference and repeat passes agree to about 1/2 of the pulse repetition frequency (PRF). In late 1999, the gyroscopes on ERS-2 failed so it became difficult to control the squint angle of the spacecraft. Data acquired after this date may have a Doppler centroid outside of the acceptable range and thus may be useless for interferometry. The squint angle for the ALOS satellite is

well controlled and the Doppler centroid is usually less than 100 Hz so we commonly focus the images at zero Doppler.

## References

- Bracewell, R.N. (1978). *The Fourier Transform and Its Applications*. Second Edition. McGraw-Hill Book Co.
- Curlander, John C. and Robert N. McDonough (1991). *Synthetic Aperture Radar: Systems and Signal Processing*. Chapter 4. John Wiley & Sons.
- Madsen, S.S. (1989). "Estimating the Doppler centroid of SAR data." In: *IEEE Trans. Aerospace and Electronic Systems* AES-25, pp. 134–140.

## B.7 Problems

1. Explain why the raw signal data are provided as complex numbers. Why are the numbers restricted to the range 0–31?
2. Why is the SAR processing done in patches rather than all at once? What is the minimum possible patch size?
3. Most SAR instruments emit a frequency modulated chirp rather than a short pulse. Why? Write a Matlab program to deconvolve the FM chirp for ERS and reproduce the impulse response function shown in Figure B4.
4. Make a plot of the real and imaginary parts of the function given in (B5) for a time interval of  $-2$  to  $2$  seconds. Use  $R_o = 850$  km,  $\dot{R}_o = 0$ ,  $\ddot{R}_o = \frac{V^2}{R_o}$ , where  $V = 7125\text{ms}^{-1}$ .
5. Derive equation (B13).
6. Derive equation (B14). (You may need to look back at Appendix A.)
7. Explain qualitatively how a SAR antenna should be squinted (turned) to keep the Doppler centroid of the return echoes close to zero for the following three cases: (a) an elliptical orbit about a spherical, non-rotating earth; (b) a circular orbit about an elliptical and non-rotating earth; (c) and a circular orbit about a rotating, spherical earth.

## C InSAR

### C.1 Forming an interferogram

Creating an interferogram from two Single Look Complex (SLC) images involves three basic steps. The first step is to align the reference and repeat images to sub-pixel accuracy. This is done by two dimensional cross correlation (*xcorr* in GMTSAR) of hundreds of small sub-patches (e.g.,  $64 \times 64$ ) taken from the master and slave images.

Then a 6-parameter affine transformation is determined using a robust 2-D fit to the offset data (i.e. *trend2d* in GMT). This is used to align the slave image to the master image and the actual alignment is done in the SAR processor (*esarp* in GMTSAR). The second step is to multiply the two SLC images to form the complex interferogram. Of course, the complex number  $C(\mathbf{x})$  in each pixel of the SLC image can be written as an amplitude  $A(\mathbf{x})$  and phase  $\phi(\mathbf{x})$ .

$$C(\mathbf{x}) = A(\mathbf{x})e^{i\phi(\mathbf{x})} \quad (\text{C1})$$

where  $\mathbf{x} = (\rho, a)$  is the position vector consisting of range  $\rho$  and azimuth  $a$ . Their product is

$$C_2 C_1^* = A_1 A_2 e^{i(\phi_2 - \phi_1)} = R(\mathbf{x}) + iI(\mathbf{x}) \quad (\text{C2})$$

The phase of the interferogram is extracted in the usual way.

$$(\phi_2 - \phi_1) = \tan^{-1} \left( \frac{I}{R} \right) \quad (\text{C3})$$

An example of the phase of reference and repeat images and their phase difference is shown in Figure C1.

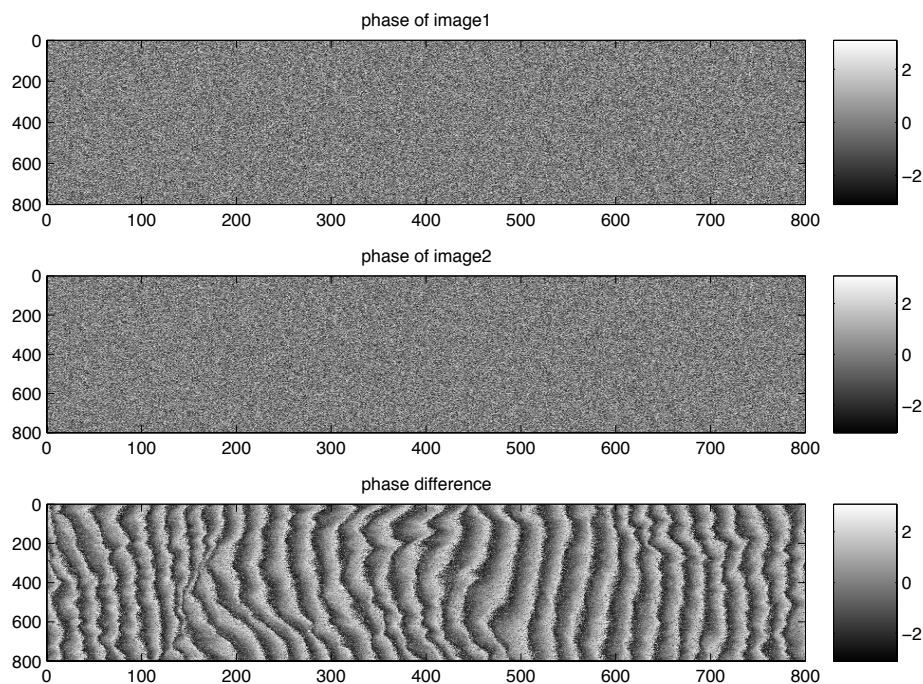


Figure C1: (upper) phase of reference SLC file. (center) phase of repeat SLC file, and (lower) phase difference of repeat - reference calculated using equations C2 and C3. The fringes across the interferogram are mostly due to the curvature of the earth where the fringe rate is proportional to the perpendicular baseline between the reference and repeat images.

## C.2 Contributions to Phase

The phase of the interferogram has many components as described in the following equation.

$$\begin{aligned}
 \textit{phase} = & \textit{earth curvature} \text{ (almost a plane, known)} + \\
 & \textit{topographic phase} \text{ (broad spectrum)} + \\
 & \textit{surface deformation} \text{ (broad spectrum, unknown)} + \\
 & \textit{orbit error} \text{ (almost a plane, largely known)} + \\
 & \textit{ionosphere delay} \text{ (a plane or 40-km wavelength waves)} + \\
 & \textit{troposphere delay} \text{ (power law, unknown)} + \\
 & \textit{phase noise} \text{ (white spectrum, unknown)}
 \end{aligned}
 \tag{C4}$$

Normally one is trying to isolate the phase due to surface deformation from all the other contributions. The largest known contributions come from the irregular shape of the earth which can be divided into an earth curvature component and a topography component. Initially we'll separate these two components but later we'll combine them to

form a complete correction for the earth's shape. In the next sections of this Appendix we derive approximate expressions for the phase and phase gradient due to earth curvature. This is followed by a derivation of the *critical baseline*, *point scatterers*, *phase due to topography*, and *altitude of ambiguity*. These are the standard equations and derivations presented previously (Rosen et al. 1996; Joughlin et al. 1996; Sandwell and Price 1998) and the derivations are useful for exposing concepts such as *parallel* and *perpendicular baseline*. However, this standard geometric model is no longer adequate for achieving high accuracy results, especially for L-band interferometry where long baselines are possible. In the final section of the Appendix we derive the more exact formulas that are implemented in our GMTSAR code in *phasediff*. Actually the more exact formulas are also conceptually and mathematically simpler than the approximate formulas and they should be used routinely.

### C.3 Phase due to earth curvature

The geometry of repeat-pass interferometry is shown in Figure C2.

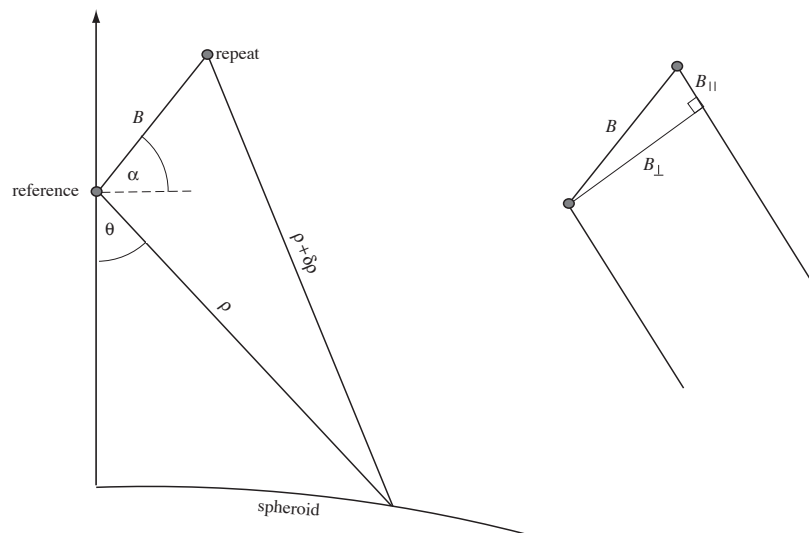


Figure C2

The important parameters are:

- $\rho$  range from reference track to reflector ( $\sim 830\text{km}$  for ERS)
- $B$  total baseline distance between reference and repeat track
- $\theta$  look angle ( $\sim 20^\circ$  for ERS)
- $\alpha$  angle between the baseline vector and the tangent plane

For discussion purposes one can divide the baseline into parallel and perpendicular components given by

$$\begin{aligned} B_{\parallel} &= B \sin(\theta - \alpha) \\ B_{\perp} &= B \cos(\theta - \alpha) \end{aligned} \quad (\text{C5})$$

Note since the look angle  $\theta$  changes across the swath, the notion of a single perpendicular baseline for an interferometric combination is only approximate. The phase difference  $\phi$  to a point on the ground is related to the range difference  $\delta\rho$ .

$$\phi = \frac{4\pi}{\lambda} \delta\rho \quad (\text{C6})$$

where  $\lambda$  is the wavelength of the radar. The law of cosines provides the relationship among the repeat-pass range, the reference-pass range, the baseline length  $B$  and the baseline orientation  $\alpha$ .

$$(\rho + \delta\rho)^2 = \rho^2 + B^2 - 2\rho B \sin(\theta - \alpha) \quad (\text{C7})$$

Next we make two standard approximations that are useful for introducing interferometric concepts but are unnecessary and also lead to inaccurate results. First we assume  $\delta\rho \ll \rho$  so we have

$$\delta\rho = \frac{B^2}{2\rho} - B \sin(\theta - \alpha) \quad (\text{C8})$$

Furthermore since  $B \ll \rho$  the parallel ray approximation yields.

$$\phi = \frac{-4\pi}{\lambda} B \sin(\theta - \alpha) \quad (\text{C9})$$

The phase difference depends on the parallel component of the baseline. The derivative of the phase with respect to range is

$$\frac{\partial\phi}{\partial\rho} = \frac{-4\pi}{\lambda} B \cos(\theta - \alpha) \frac{\partial\theta}{\partial\rho} \quad (\text{C10})$$

This phase gradient depends on two terms, the perpendicular component of the baseline  $B_{\perp} = B \cos(\theta - \alpha)$  and the derivative of look angle with respect to range  $\delta\theta/\delta\rho$ . The perpendicular baseline varies slightly with look angle across a typical SAR image. The change in look angle usually increases with range so  $\delta\theta/\delta\rho > 0$ . However, when the local terrain slope exceeds the look angle (actually the incidence angle), an increase in look angle does not produce a corresponding increase in range. This is the *layover* geometry where  $\delta\theta/\delta\rho \leq 0$ .

#### C.4 Look angle and incidence angle for a spherical earth

In order to calculate the derivative of look angle with respect to range  $\delta\theta/\delta\rho$  we make the approximation that the earth is locally spherical although we will adjust the local radius of the Earth using the WGS84 ellipsoid C11. While this approximation is good locally, there can be large differences between the elliptical earth model and the local radius for long SAR swaths. This difference will produce topographic fringes in long-

strip interferograms depending on the interferometric baseline. We will deal with this issue later by including the ellipsoidal radius minus the local radius into a topographic correction term. The local earth radius is given by

$$r_e(\varphi) = \left( \frac{\cos^2 \varphi}{a^2} + \frac{\sin^2 \varphi}{c^2} \right)^{-1/2} \quad (\text{C11})$$

where  $\varphi$  is latitude, and  $a$  and  $c$  are the equatorial (6378 km) and polar (6357 km) radii, respectively.

The look angle of the radar depends only on the local earth radius  $r_e$ , the range to the sphere  $\rho$ , and the height of the spacecraft above the center of the Earth  $b$  as shown in the following diagram.

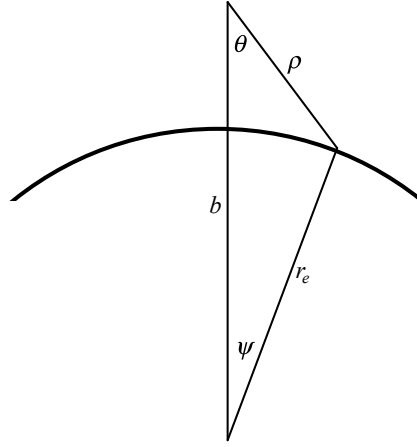


Figure C3: Triangle formed by the range  $\rho$ , radius of the earth  $r_e$  and spacecraft height  $b$ .

Using the Law of cosines one finds

$$\eta = \cos \theta = \frac{(b^2 + \rho^2 - r_e^2)}{2\rho b} \quad (\text{C12})$$

On a sphere, the incidence angle is greater than the look angle by the angle  $\psi$ .

To determine the derivative of the phase (C10) we need to determine the derivative of the look angle with respect to range from equation C12. After a little algebra, we find an expression for the phase gradient due to earth curvature.

$$\frac{\partial \phi}{\partial \rho} = \frac{-4\pi B}{\lambda \rho} \frac{\cos(\theta - \alpha)}{\sin \theta} \left( \cos \theta - \frac{\rho}{b} \right) \quad (\text{C13})$$

Look angle	23°	34°	41°
ERS/ENVISAT 16 MHz	1.1 km	2.0	2.9
ALOS FBD 14 MHz	3.6	6.5	9.6
ALOS FBS 28 MHz	7.3	13.1	18.6

Table C1: Comparison of critical baseline. ERS/ENVISAT – altitude = 790 km, wavelength = 56 mm. ALOS – altitude = 700 km, wavelength = 236 mm. Shaded area is most common mode for interferometry.

Using (C9), one can also derive an expression for total phase versus range.

$$\phi = \frac{-4\pi B}{\lambda} \left[ (1 - \eta^2)^{1/2} \cos \alpha - \eta \sin \alpha \right] \quad (\text{C14})$$

where  $\eta$  given in equation C12. Equation C14 is the approximate earth curvature correction that was used in our older codes.

### C.5 Critical baseline

If the fringe rate across the interferogram due to earth curvature exceeds  $2\pi$  radians per range cell then the reference and repeat images will be completely decorrelated. Consider a single range pixel of length  $\Delta\rho = C\tau/2$ . The phase of this pixel in the reference image is the vector sum of the phase from all of the scatterers in the pixel. The repeat image will have the same scatterers. However if the baseline is critical, there will be an additional  $2\pi$  phase delay across the range cell that will cause the sum of the scatterers to be randomly different from the reference image. This is called baseline decorrelation and the length at which complete decorrelation occurs is the *critical baseline*. For this calculation, we start with equation C13 and make a flat-earth approximation  $\rho/b = 0$ . To avoid baseline decorrelation, change in phase with range must be less than

$$\frac{\partial\phi}{\partial\rho} = \frac{-4\pi B_{\perp}}{\lambda\rho} \frac{\cos\theta}{\sin\theta} < \frac{2\pi}{\Delta\rho} \quad (\text{C15})$$

The baseline where the fringe rate equals the critical value is

$$B_c = \frac{\lambda\rho}{C\tau} \tan\theta \quad (\text{C16})$$

For the parameters of the ERS satellite the critical baseline is 1100 m (Table C1). For topographic recovery, a baseline of about 1/4 critical is optimal. Of course for change detection, a zero baseline is optimal but not usually available.

## C.6 Persistent point scatterer and critical baseline

Consider a ground range resolution of single pixel, which is related to the pulse length and the incidence angle  $R_r = C\tau/(2 \sin \theta)$ . This cell is imaged from two positions separated by a perpendicular baseline (Figure C4). If the resolution cell contains only a single persistent scatterer then the change in the viewing geometry will not change the range to the single scatterer and the pixel will remain coherent. However, if there is a uniform distribution of persistent scatterers in the cell then the scatterers at the edges of the cell will have a change in range of  $\delta\rho = \frac{R_r}{2} \sin \delta\theta \cos \theta$ . If this is less than a quarter of the wavelength then the phase shifts at the ends of the resolution cell will not destroy the correlation in the cell. Note that since the path delay is  $2\delta\rho$ , the phase delay is one half wavelength. Working through the algebra one finds that this critical baseline is the same as found above.

$$B_c = \frac{\lambda\rho}{2R_r \cos \theta} = \frac{\lambda\rho}{C\tau} \tan \theta \quad (\text{C17})$$

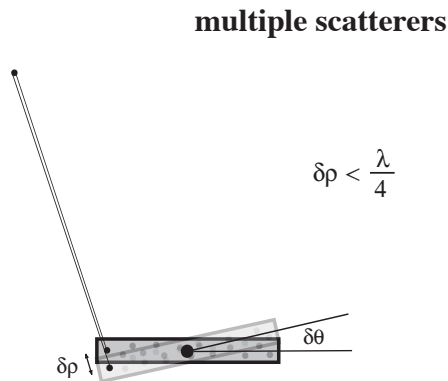
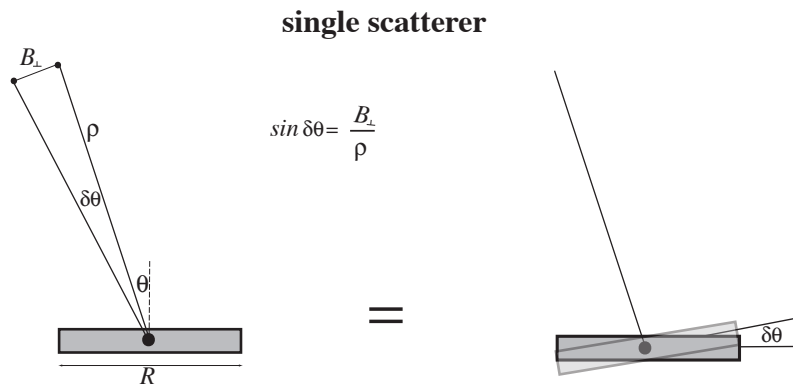


Figure C4: Diagrams showing the effects of changing viewing angle  $\delta\theta$  for a resolution cell of length  $R$ . (upper) point scatterer has no phase change with viewing angle. (lower) has multiple scatterers where the vector sum of the phase will vary with viewing angle in a random way causing decorrelation.

### C.7 Phase due to topography

One can use the approximate formula (C9) for the phase due to earth curvature to also calculate the topographic phase. The actual radius of the earth (land),  $r$ , is usually greater than the radius of the spheroid  $r_e$  and this difference is geometric elevation.

The phase due to the actual topography can be expanded in a Taylor Series about  $r_e$ .

$$\phi(r) = \phi(r_e) + \left. \frac{\partial \phi}{\partial r} \right|_{r_e} (r - r_e) + \left. \frac{1}{2} \frac{\partial^2 \phi}{\partial r^2} \right|_{r_e} (r - r_e)^2 + \dots \quad (\text{C18})$$

Using equations C9 and C12 one can calculate the first two derivatives. It turns out that the second derivative is about  $(r - r_e)/r$  times the first derivative (i.e., 2.7/6371 for our area) so we only need to keep the first two terms in the series. The first term is C12 while the second term is

$$\left. \frac{\partial \phi}{\partial r} \right|_{r_e} = \frac{-4\pi r_e B \cos(\theta_e - \alpha)}{\lambda \rho b \sin \theta_e} \quad (\text{C19})$$

where  $\theta_e$  is the look angle to the spheroid (C12). The mapping of total unwrapped phase into elevation as a function of range is

$$(r - r_e) = \frac{-\lambda \rho b}{4\pi r_e} \frac{\sin \theta_e}{B \cos(\theta_e - \alpha)} (\phi - \phi_e) \quad (\text{C20})$$

One should remember that the unwrapped interferogram does not provide the complete phase difference  $\phi - \phi_e$  since there is an unknown constant of integration. While this formula is useful for demonstrating that the magnitude of the topographic phase correction is proportional to the perpendicular baseline, the formula is only approximate. The more exact approach, discussed next, is used in the GMTSAR code.

## C.8 Altitude of ambiguity

The fringe rate due to topography can be reformulated to provide the error in the elevation model that will produce one fringe ( $2\pi$ ) error in the interferogram. Again we'll use a flat-earth geometry so  $b/r_e = 1$ . From equation C20 we find the altitude of ambiguity is

$$h_a = \frac{\lambda \rho \sin \theta_e}{2B_\perp} \quad (\text{C21})$$

For the case of ERS with a perpendicular baseline of 100 m, this altitude of ambiguity is about 90 m. For change detection, a higher number is better.

## C.9 Phase due to earth curvature and topography – exact formula

The above text describes the standard approximations that are in most InSAR packages such as ROI\_PAC and Gamma. However there is a second order term in the derivation that can become important when the baseline is long. We start the derivation with equation C7 where we have expanded the left side and cancelled the  $\rho^2$  terms.

$$2\rho\delta\rho + \delta\rho^2 = B^2 - 2\rho B \sin(\theta - \alpha) \quad (\text{C22})$$

This can be rewritten as

$$\delta\rho = -B \sin(\theta - \alpha) + \frac{1}{2\rho} (B^2 - \delta\rho^2) \quad (\text{C23})$$

Now in the approximate derivation in the sections above we found a good approximation to the range change is given by  $\delta\rho = -B \sin(\theta - \alpha)$ . If we use this as a guess for the right hand side of equation (C23) we find a second order approximation to the range change is

$$\delta\rho = -B \sin(\theta - \alpha) + \frac{B^2}{2\rho} [1 - \sin^2(\theta - \alpha)]$$

or

$$\delta\rho = -B \sin(\theta - \alpha) + \frac{B^2}{2\rho} \cos^2(\theta - \alpha)$$
(C24)

Note that we could iterate on this substitution to come up with a more accurate correction. The error introduced by neglecting the second order term is proportional to the perpendicular baseline squared and it is inversely proportional to range. Next we estimate the magnitude of the second order term in relation to the first order term

$$\text{ratio} = \frac{B \cos^2(\theta - \alpha)}{2\rho \sin(\theta - \alpha)}$$
(C25)

Note that this ratio is wavelength independent. Setting  $\alpha = 0$  and using a nominal look angle of  $30^\circ$ , the ratio is

$$\text{ratio} = \frac{3B}{4\rho}$$
(C26)

For a nominal range of 750 km and a baseline of 100 m the ratio is  $10^{-4}$  and for a baseline of 2000 m, which is typical for an L-band interferogram, the ratio is  $2 \times 10^{-3}$ . We show below that this corresponds to a 0.6 m phase ramp across an image so this second order term should not be neglected. Moreover the phase ramp from the second order term always has the same sign even when the sign of the perpendicular baseline changes.

Therefore software that performs baseline re-estimation in an effort to reduce phase ramps will have a biased baseline estimate that will consistently amplify the topographic phase correction. For a large stack of interferograms, this could appear as a systematic elevation-dependent error.

The phase correction due to earth shape depends on the look angle as a function of range. In the main section of this document we discussed an algorithm for mapping a topographic grid from longitude, latitude, and topography above the ellipsoid to range, azimuth, and topography  $t(\rho, a)$  above a local spherical shape for the earth. Using this information we can combine the earth curvature correction and the topographic phase correction into a single correction. The algorithm is:

1. Read a row of data from the reference and repeat SLC files so every pixel in the reference image can be assigned a range  $\rho$  and azimuth  $a$ .
2. Using the precise orbital information compute the radius of the spacecraft orbit for the reference image  $b(a)$ , the length of the baseline  $B(a)$ , and the orientation of the baseline  $\alpha(a)$ .

- Interpolate the topography to each range pixel and compute the look angle using the following formula.

$$\theta = \cos^{-1} \left\{ \frac{\left( b^2 + \rho^2 - (r_e + t(\rho, a))^2 \right)}{2\rho b} \right\} \quad (\text{C27})$$

- Now that we have the look angle for each range pixel, we can calculate the phase correction to be applied to the repeat image.

$$\phi = -\frac{4\pi B}{\lambda} \sin(\theta - \alpha) + \frac{2\pi B^2}{\lambda\rho} \cos^2(\theta - \alpha) \quad (\text{C28})$$

- Multiply the repeat image by the complex phase and form the interferogram. Note this phase correction should be applied before any multilook averaging or filtering.

$$R(\mathbf{x}) + iI(\mathbf{x}) = C_2 C_1^* e^{i\phi} \quad (\text{C29})$$

- Extract the interferometric phase that is now corrected for both the earth curvature and the topographic phase.

$$(\phi_2 - \phi_1) = \tan^{-1} \left( \frac{I}{R} \right) \quad (\text{C30})$$

An example of a 1.95 km long baseline interferogram that was constructed both with and without the second order phase correction is shown in Figure C5. The interferogram with the approximate phase correction has a ramp across the image as well as a small phase variation due to topography. Note there is 3200 m of relief within this interferogram and for this baseline the altitude of ambiguity is 27.4 m so there are 120 fringes in the full interferogram (Figure C5(a)) that need to be removed. The residual fringes (b) could be residual topographic phase but also could be tropospheric delay or orbital error.

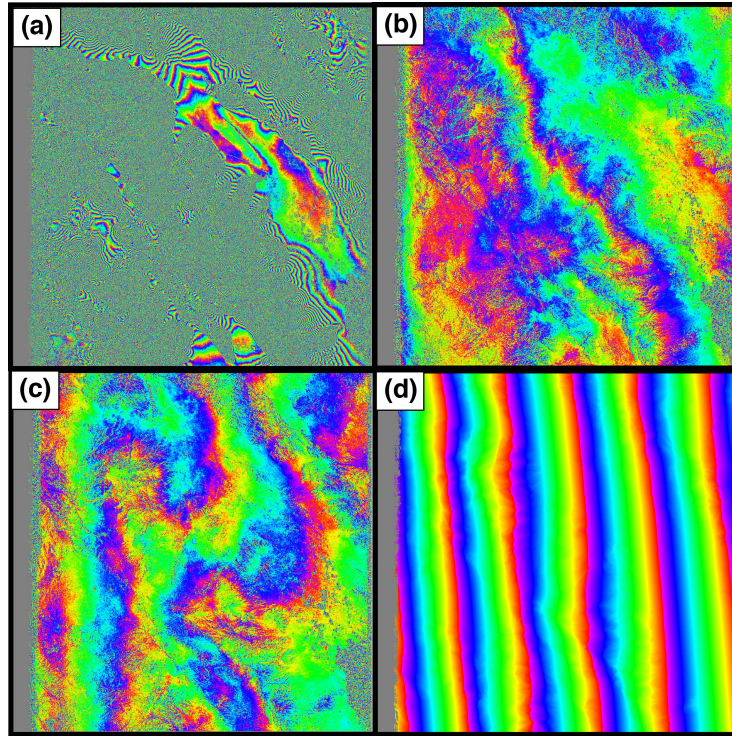


Figure C5: (a) A 1.95 km baseline interferogram with no topography correction has 120 fringes that need to be accurately removed. (b) Same interferogram corrected using the exact formulas (C27) and (C28). (c) Same interferogram corrected using the approximate formulas (C12) and (C14). (d) difference between exact and approximate corrections corresponds to a 0.6 m ramp. The interferogram is marked as the blue baseline shown in Figure 6 (T213, F0660, O 02220 to 02891)

## References

- Joughlin, I. et al. (1996). "Measurement of ice sheet topography using satellite-radar interferometry". In: *J. Glaciology* 42, pp. 10–22.
- Rosen, P.A. et al. (1996). "Surface deformation and coherence measurements of Kilauea Volcano, Hawaii from SIR-C radar interferometry". In: *J. Geophys. Res.* 101.E10, pp. 23109–23125.

Sandwell, D.T. and E.J. Price (1998). “Phase gradient approach to stacking interferograms”. In: 103.B12, pp. 30183–30204.

## C.10 Problems

1. Develop a formula similar to (C12) for the incidence angle as a function of local earth radius  $r_e$ , the range to the sphere  $\rho$  and the height of the spacecraft above the center of the Earth  $b$ .
2. Make an interferogram from two SLC images using Matlab. Online you will find 2 binary SAR image files, \*.SLC, and 2 ascii header files, \*.PRM (download at <http://topex.ucsd.edu/rs/lab8>). The site also contains some Matlab code to read the data and get started (lab8start.m). This is an ERS-1 to ERS-2 tandem pair from the Salton Sea, perpendicular baseline 58 m. The \*.PRM files have been included for your information only and will not be of much use for the problems below. This lab illustrates SAR interferometry. First look at the phase of the reference image. It will look like random noise. Then look at the phase of the repeat image. It will also look like noise. Finally examine the phase difference. This will show interferometric fringes across the image related to the curvature of the Earth.
  - (a) Make the best-looking amplitude image that you can using images 1 and 2. This could involve low-pass filtering and perhaps averaging the two images. I can't provide a recipe for doing this, but note that the pixels are 16 m in the range direction and only 4 m in the azimuth direction (top-to-bottom) so the filter should be taller than it is wide by about 4 times. Remember these are complex numbers so would one construct amplitude then filter or filter the real and imaginary parts and then make amplitude? When and how should the images be averaged?
  - (b) Make the interferogram and filter it to make the best-looking phase map. Should one filter before or after interferogram formation? Should one filter the real and imaginary components or filter the phase?
  - (c) Do the best that you can to remove the phase ramp across the image. How do you estimate the phase ramp and what is the best way to remove it?
  - (d) Try to unwrap the phase using Matlab?
3. Derive equation (C13). What happens when the change in phase with increasing range exceeds  $2\pi$  radians per range resolution cell?
4. Give two reasons why the critical baseline for ALOS is more than 10 times longer than for ERS.
5. What happens to the phase of an interferogram in areas where the slope of the topography facing the radar exceeds the incidence angle of the radar?
6. Derive equation (C27). What is the correct zero level for the topography in this equation?

## D ScanSAR Processing and Interferometry

From Tong, Sandwell, and Fialko 2010.

The systematic observation strategy of ALOS PALSAR provides strip-mode SAR imagery along every ascending orbital track and ScanSAR imagery (Figure D1) along every third descending orbital track. Therefore to obtain a second look direction of PALSAR interferometry sometimes requires processing ScanSAR to ScanSAR mode interferograms. The method is based on the proposal by Bamler and Eineder 1996 that, with proper pre-processing, standard strip-mode software can be used to construct phase-preserving SAR images and ultimately interferograms. The main advantage of using the standard strip-mode approach, instead of the traditional SPECAN approach (Sack and Cumming 1985), is that existing and well tested, strip-mode InSAR processing software can be used. The main disadvantage of this approach is that the zero-padding between the bursts wastes considerable disk space and computer time. Nevertheless the two approaches should provide equivalent results.

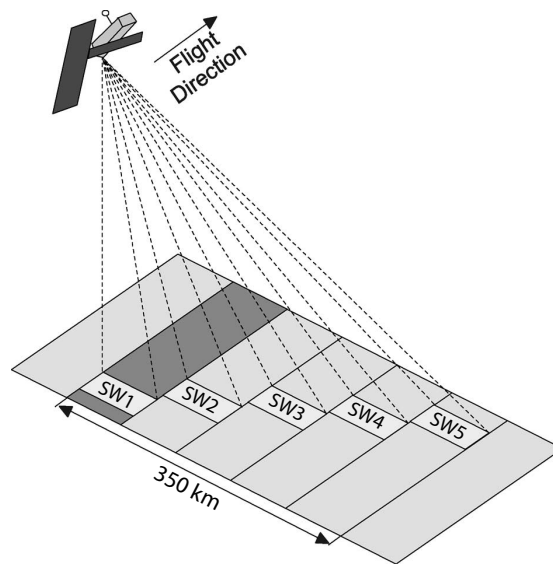


Figure D1: Schematic diagram of ScanSAR imaging. The radar acquires data for short bursts over each of 5 subswaths. Each subswath is illuminated over 1/5 of cycle length in the along-track direction such that 4/5 of each subswath is not illuminated. Modified from Bertran-Ortiz and Zebker 2007.

Our strip-mode preprocessor for ALOS was developed and tested using data along a descending orbital track (T538) over Southern California. This track contains two permanently installed radar corner reflectors that are used by JAXA to provide radiometric and geometric calibration for the lifetime of the mission. JAXA has collect

PALSAR data over these reflectors in a variety of modes on both ascending and descending tracks. We have extended the ALOS preprocessing software to first perform ScanSAR to FBD mode interferometry and second to perform the more challenging ScanSAR to ScanSAR interferometry where a significant burst overlap is needed. Indeed both luck and accuracy are required to achieve a full swath-width ScanSAR to ScanSAR interferogram. The ScanSAR acquisition geometry and parameters for PALSAR are provided in Tables D1 and D2. The 5 subswaths cover an area 350 km wide. Following Bamler and Eineder 1996, the ScanSAR data are zero-padded to construct swath type data. The original WB1 file contains the bursts of all 5 sub-swaths as consecutive rows. The preprocessor separates the data into 5 separate files where missing lines between the bursts are filled with zeros. Zeros are also added to the end of each echo to match the length of a standard FBD data file. In addition, the first 12 lines of each burst are zero-padded because these data are incorrect [Masanobu Shimada, personal communication, 2008]. Since the sub-swaths are processed independently and their amplitude and interferometric phase are recombined in the latitude-longitude coordinate system, an accurate geometric model, precise orbit, and consistent set of processing parameters is required to achieve a seamless recombination. The preprocessing code is rather complex because the pulse repetition frequency (PRF) of the PALSAR echoes varies in three ways. First, as shown in Table D2, each sub-swath has its own PRF optimized to reduce crosstalk. Second, the PRF can change along the satellite track on any one of the sub-swaths. A PRF change on any sub-swath changes the time interval and number of zero-pad lines needed on all the other sub swaths. Finally, when considering reference and repeat images for interferometry, the PRF's on a matching sub-swaths can be different causing the burst alignment to change along the swath as we find in the example below. In addition each sub-swath has its own near range which, varies along the track so rows must be shifted to align the near range to the common prescribed value. Any small error in the preprocessing could result in a poorly focused image and/or low interferometric coherence.

The first step in the software development was to focus the raw sub-swath data to form seamless amplitude imagery. We found that the best image quality (i.e. minimal scalloping) was achieved by setting the length of the synthetic aperture to be exactly 6 bursts. This corresponds to setting the time ( $\sim 4.7$  s) and along-track distance of synthetic aperture to be exactly the same for each sub swath. We have found that by processing the SAR image to zero Doppler, the position of the radar corner reflectors in the image matches the position predicted from the orbit (zero range rate) to within 1 pixel in range and 4 pixels in azimuth. This good match provided confidence that the code is geometrically accurate.

The second step in the software development was to construct ScanSAR to swath mode interferometry. This combination should always provide interference fringes because there is 100% overlap between the sparse bursts of the ScanSAR and the complete coverage of the swath (Bertran-Ortiz and Zebker 2007). The ALOS track 538 over Los Angeles has two FBD acquisitions and 3 ScanSAR WB1 acquisitions. The swath of the FBD data (34.3 incidence angle) overlaps with sub-swath 4 of the WB1 data. We experimented with three interferometric mode combinations, FBD to FBD, FBD to ScanSAR, and ScanSAR to ScanSAR. The FBD to FBD interferogram had a 10 m baseline and 46-day timespan resulting in excellent overall coherence of 0.67.



sus burst overlap fraction (Figure D2c) illustrates that a maximum coherence of about 0.35 occurs where the burst overlap is greater than 50%. The coherences diminishes to below 0.2 at a burst overlap of 18%. The results show that good interferometric results can be achieved when the burst overlap is greater than about 50%.

Assuming there is no control on the burst alignment of reference and repeat images there is a 1-in-5 chance of this occurring from any two ScanSAR images. We used probability theory to show that 5 repeat SAR images are needed to have a 90% chance of half burst overlap for at least one pair (Table D3). One successful alignment with half burst is called an event, of which the probability is 20%. We know these events are independent, but not disjoint with each other. The probability for multiple SAR images can be generalized with calculation on probability of the union.

<b>Number of SAR images</b>	<b>Number of interferometry pairs</b>	<b>Probability of getting at least one pair with half burst alignment</b>
2	1	0.2
3	3	0.488
4	6	0.7379
5	10	0.8926
6	15	0.9648
7	21	0.9908
8	28	0.9981

Table D3: The probability analysis on getting half burst alignment.

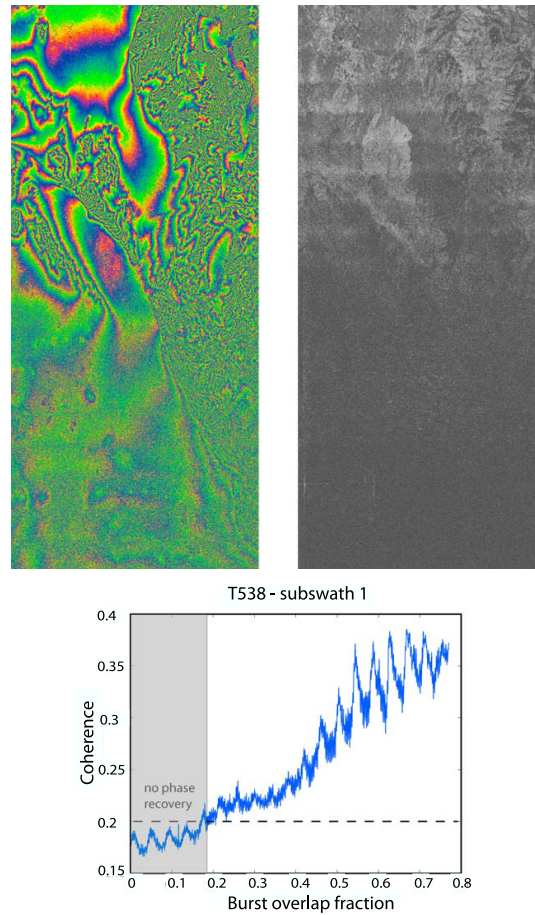


Figure D2: ScanSAR to ScanSAR interferogram for subswath 4 of track 538 across the Los Angeles basin. The perpendicular baseline is 450 m and the time interval is 92 days. No topographic phase has been removed. (a) interferometric phase is high at top of swath where burst overlap is large and lower toward the bottom. (b) coherence also decreases from top to bottom as burst overlap decreases. (c) row-averaged coherence versus burst overlap.

## References

- Bamler, R. and M. Eineder (1996). "ScanSAR processing using standard high precision SAR algorithms". In: *IEEE Trans. Geosci. Remote Sens.* 34.1. doi:10.1109/36.481905, pp. 212–218.

- Bertran-Ortiz, A. and H.A. Zebker (2007). “ScanSAR-to-Stripmap Mode Interferometry Processing Using ENVISAT/ASAR Data”. In: *Geosci. Rem. Sensing* 45.11, pp. 3468–3480.
- Sack, M. and I.G. Cumming (1985). “Application of efficient linear fm matched filtering algorithms to synthetic aperture radar processing”. In: *IEEE Proc. Part F Radar Signal Processing* 132.2, pp. 45–57.
- Tong, X., D.T. Sandwell, and Y. Fialko (2010). “Coseismic slip model of the 2008 Wenchuan earthquake derived from joint inversion of interferometric synthetic aperture radar, GPS, and field data”. In: *J. Geophys. Res.* 115.B04314. doi:10.1029/2009JB006625.

## D.1 Problems

1. ScanSAR is a technique to construct a very wide swath radar image by emitting a burst of  $\sim 300$  radar pulses on a narrow subswath and systematically cycling the near range of each burst to illuminate 5 parallel subswaths ultimately forming a wide swath. Why is it not possible to simply illuminate the wide swath with continuous wide pulses? Hint, see equation A12.
2. How can a standard strip-mode SAR processor be used to focus ScanSAR data? What are the advantages and disadvantages of this approach?
3. Phase coherence for regular swath-mode interferometry is only possible when the baseline between the reference and repeat images is less than the critical baseline and there is significant overlap in the Doppler spectra of the reference and repeat images. What additional attribute is needed to achieve phase coherence for ScanSAR interferometry?
4. How many different interferometric combinations are possible for 10 SAR images? For 100 SAR images? For  $n$  SAR images?

## E Sentinel TOPS-mode processing and interferometry

From Xu et al. 2017

### E.1 Introduction

Two new InSAR satellites Sentinel-1A and B are providing regular 12- or 24-day acquisitions over all tectonically active land areas. Unlike previous SAR data, these data are completely open and sharable. To access these data you register with ESA and then use the Sentinel Data Hub for download. Both can be found at <https://scihub.copernicus.eu/dhus/>. The short 12-day repeat cycle of these satellites requires that they operate in a wide swath mode to provide complete coverage; the swath width must exceed  $\sim 230$  km for full coverage at the equator. As discussed in Appendix A, the width of the swath is limited by the length of the antenna and the standard SAR satellites have a maximum swath width of  $\sim 80$  km. One way to increase the swath width is to operate the radar in a ScanSAR mode as described in Appendix D. One problem with ScanSAR is that the amplitude image created from the focused data can have an along-track modulation or scalloping associated with each bursts of the radar. A more uniform amplitude image can be achieved using a new radar mode called Terrain Observation by Progressive Scans (TOPS) (Meta et al. 2010). In the TOPS mode, the radar scans each of 3 subswaths in succession from the bottom to the top (e.g., SW1) as the radar advances as shown in Figure E1 (Mittermayer et al. 2010). The next subswath (SW2) is scanned in the same manner and finally the third subswath.

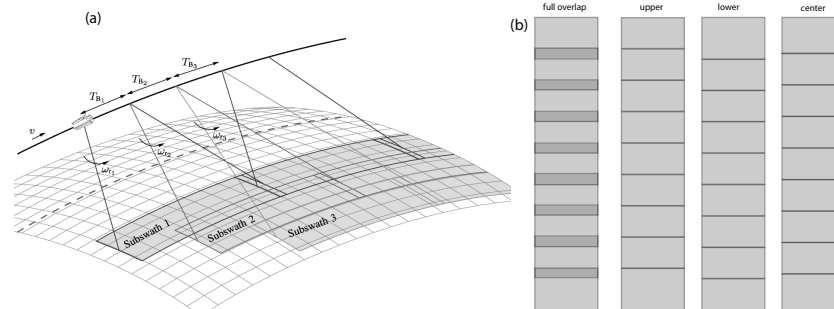


Figure E1: (a) Diagram of the TOPS acquisition geometry where  $v$  is the velocity of the satellite,  $T_B$  is the burst duration and  $\omega_r$  is the steering rate (Mittermayer et al. 2010). Each subswath is about 80 km wide and each burst covers a 20 km distance in the along-track direction. There is some overlap between the subswaths and bursts to provide a seamless mosaic of amplitude and phase. The phase difference in the overlap areas can be used to refine the image alignment. This is called *enhanced spectral diversity*. (b) The overlapping bursts can be *debursted* in three ways to form an SLC having no overlap by extracting the lines in the high, low, and center configurations.

While this approach results in a more uniform amplitude radar image, the squint angle is constantly changing causing large variations in the Doppler rate ( $\pm 2250$  Hz) away from the ideal Doppler rate of zero. Traditional radar interferometry is usually performed using data close to zero Doppler or at a Doppler that is much smaller than the pulse repetition frequency (PRF). Indeed to achieve phase coherence of the interferogram, the Doppler centroids of the reference and repeat image must overlap by at least 20% as described in Appendix D. Data acquired in the TOPS mode sweeps over 9 PRF intervals during one scan as shown in Figure E2a.

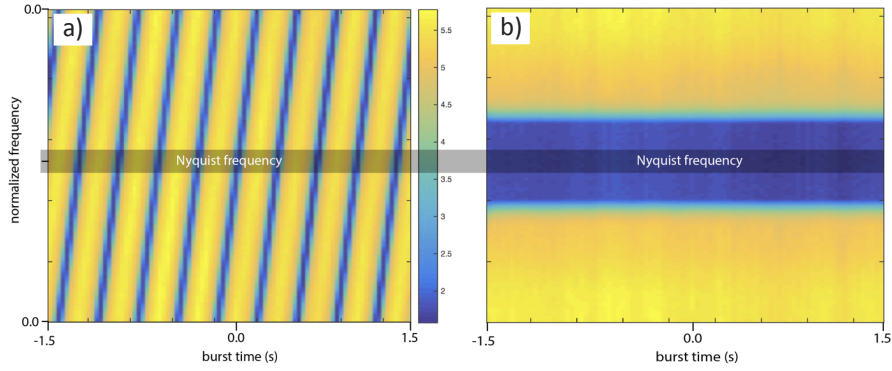


Figure E2: Spectrogram of one burst of TOPS-mode data plotted on a log color scale. (a) Original spectrogram of a single burst of TOPS data wraps around the Nyquist frequency 9 times. (b) Spectrogram after deramping has low power close to the Nyquist, which enables accurate resampling.

As long as the bursts of the reference and repeat images are well aligned in the along-track direction, one can achieve high phase coherence. However because of slight differences in the orbital velocity or burst timing of the reference and repeat acquisitions, there will be small misalignment of the bursts in the azimuth direction. There is a large difference between the Doppler rate at the upper and lower edge of each burst ( $f_u - f_l$ ), so a small azimuth misalignment will result in a significant phase mismatch at burst boundaries. Indeed one can use the phase difference  $\phi$  in the small burst overlap areas to estimate the azimuth shift  $\Delta a$  needed to reduce this phase mismatch. This method is called *enhanced spectral diversity* and the implementation is discussed below.

$$\Delta a = PRF \frac{\phi}{2\pi(f_u - f_l)} \quad (E1)$$

For example for S1A the top-to-bottom Doppler difference is 4500 Hz and the effective PRF is 486 Hz so keeping the phase mismatch below, for example, 0.54 radian (2.8 mm) requires azimuth alignment to 0.01 pixel accuracy.

## E.2 Traditional Image Alignment Fails with TOPS-Mode Data

The traditional approach to InSAR image alignment is done in three steps: (1) First, the orbital information is used to make a rough (1-2 pixel accuracy) estimate of the offset of the master and slave images. (2) Then 2-D cross correlation of sub-patches of data (e.g., 64 by 64 pixels) is used to estimate the affine transformations needed to map the slave image onto the master image. As described in Appendix B, the trajectories of the master and slave images are very smooth so their differences in both the range  $dr$  and azimuth  $da$  coordinates are well described by the following equations

$$\begin{aligned} dr &= c_0 + c_1 r_m + c_2 a_m \\ da &= c_3 + c_4 r_m + c_5 a_m \end{aligned} \tag{E2}$$

where  $r_m$  and  $a_m$  are the range and azimuth coordinates of the master image and there are 6 unknown coefficients  $c_{0--5}$ . The coefficients are determined by fitting planes to the range and azimuth offset data derived from the cross correlation of the sub-patches. It seems reasonable that 6 parameters are sufficient to completely account for the orbital differences because the orbit is well described by a 6-element state vector and the differences in the master and slave state vectors is very small over the time span of the radar acquisition. (3) The final step is to use a 2-dimensional sinc-function interpolator to resample the slave image into the coordinates of the master image. The accuracy of the alignment depends on the coherence between the reference and repeat images. When coherence is high the two images can be aligned to 0.1 pixel accuracy. When the coherence is low, the alignment can be worse than 1.0 pixel. The method fails when the master and slave images have poor correlation.

This standard approach to image alignment works well on swath-mode SAR data as well as ScanSAR data, however it fails with the TOPS-mode data for two reasons. First the traditional method can only achieve 0.1 pixel alignment accuracy but as discussed above, the alignment must be better than 0.01 pixel to keep the phase mismatch between the burst boundaries below 2.8 mm. Second, because the azimuth spectrum of the TOPS-mode data has frequencies well above the Nyquist sampling frequency of the SLC data (Figure E2a), the standard sinc-function interpolation fails.

An example of using this traditional approach to align a master and slave SLC images of S1A TOPS mode is shown in Figure E3. There are two main problems with this interferogram that need to be corrected. The first is that there are large phase mismatches at the 8 boundaries between the 9 bursts. The second problem is that straightforward interpolation of the slave image using a 2-dimensional sinc interpolator results in banding within each burst. The problem is that the SLCs have a spectrum that wraps around the Nyquist frequency 9 times as the radar scans from the bottom to the top of the burst (Figure E2a). The sinc-function interpolator is inaccurate where it crosses the Nyquist boundary. We also attempted to use the shift-property of the Fourier transform to perform the azimuth resampling but it also resulted in banding.

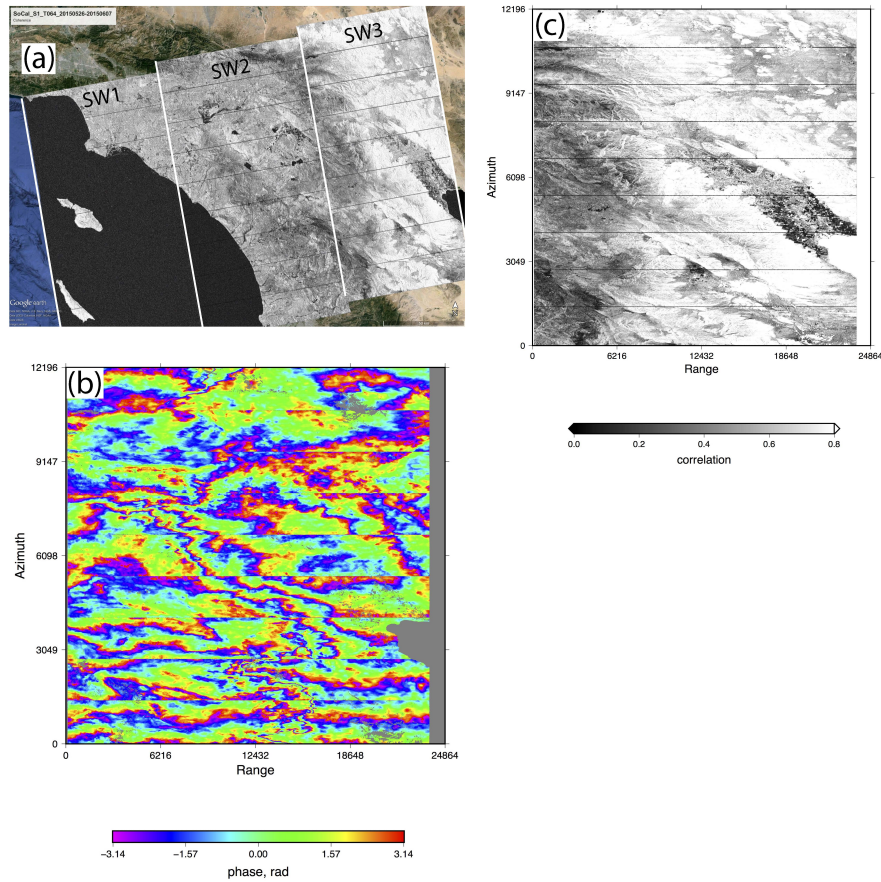


Figure E3: (a) Coherence image of test area for track 064 dates 20150526 and 20150607. The S1A data have three subswaths and 9 bursts. (b) InSAR phase of subswath 3 in radar coordinates shows phase mismatch at burst boundaries as well as banding within each burst. (c) InSAR coherence is generally high with 8 lines of low coherence due to the phase mismatch as well as banding within each burst due to poor performance of the sinc interpolator across the Nyquist frequency.

### E.3 Geometric Image Registration

Overcoming these two issues requires two new approaches: geometric alignment based on a precise orbit (Sansosti et al. 2006) and deramping of the SLC data prior to interpolation. The Sentinel-1 SAR data are provided with a high accuracy orbit ( $\sim 2\text{--}3$  cm radial and cross track,  $\sim 5$  cm along-track (Fernandez et al. 2015)) available at:

[https://www.unavco.org/data/imaging/sar/lts1/winsar/slqc/aux\\_poeorb/](https://www.unavco.org/data/imaging/sar/lts1/winsar/slqc/aux_poeorb/).

This high accuracy enables purely geometric registration to remove almost all the phase mismatch at the burst boundaries. The algorithm for deramping the slave image prior to interpolation is described in the ESA documentation (Miranda 2015) and all the parameters are provided with the XML files that accompany the SAR imagery files. The overall algorithm is:

1. Construct a low-resolution ( $\sim 12$  arc-seconds) digital elevation model covering the area of the SLC images. If no elevation data are available (e.g., Antarctica), a guess at the mean elevation will provide very good results.
2. Use the precise orbital information to map each pixel of longitude, latitude and height into the range and azimuth of the radar pixel coordinates. This is done as described in Section 1.2.2 where one finds the azimuth of closest range on the orbital trajectory to each topography pixel—first using a Golden section search algorithm and then performing a polynomial refinement. This is done for both the master and slave images.
3. Construct a table of slave minus master range differences and slave minus master azimuth differences versus range and azimuth. An example is provided in Table E1. Construct two grids of range offsets versus range/azimuth and azimuth offset versus range/azimuth. These grids provide the pixel-by-pixel mapping of the slave image onto the master image. We call this *point-by-point registration (PBP)*. A second approach is to fit a plane to each of these grids to find the 6 affine parameters described in equation E2. We call this method *6-parameter registration (6-par)*.
4. Deburst the master image to make a continuous SLC. This is done by calculating the boundaries between bursts using the azimuth time for each line in the burst and eliminating overlapping lines. Stitching of the bursts is done using the center of the overlapped area between bursts (Figure E1b, right column).
5. Read a burst of slave SLC data into computer memory.
6. Compute the complex phase ramp following the ESA documentation (Miranda 2015). The deramping and demodulation removes a known ramp that is caused by antenna steering.
7. Multiply the SLC by the complex conjugate of the phase ramp to de-ramp the SLC. An example of the de-ramped spectrum for a slave image is shown in Figure E2b. After this operation the power in azimuth is close to zero at the Nyquist frequency to enable accurate interpolation.
8. Use a 2-D sinc function to interpolate the fractional part of the range and azimuth shift (6-par or PBP) of the slave SLC into the coordinates of the master SLC. For the 6-par, equation E2 is used for mapping, while for PBP, each point in the burst is done using the range-shift and azimuth-shift grids developed in step (3).
9. Re-compute the complex phase ramp in step (6) with the appropriate range and azimuth shift and multiply by the resampled slave SLC.

10. Output the central part of each burst so there is no azimuth overlap with the adjacent burst. This is done for both the master and slave. If the alignment requires enhance spectral diversity, as discussed below, then one should output only the upper and lower portions of each burst (master and slave) that overlap the adjacent burst.
11. Repeat steps (5) through (10) until all the bursts common to the master and slave image are processed.

At this point we have master and slave SLCs that are aligned to the accuracy of the orbit data. Note that this accuracy is far better than 0.1 pixel so the interferometric coherence between the master and slave should be optimal. A remarkable result of this geometric alignment approach is that one can align many slaves to a single master and, after this alignment. Any two of the slave images can be used to form highly coherent interferograms. Below we assess the phase accuracy of the geometrically aligned interferograms, both master-to-slave and slave-to-slave.

$r_m$	$dr$	$a_m$	$da$
21612.658170	68.048382	9.502554	5.581971
21545.310230	68.050767	5.672641	5.582379
21476.796745	68.049944	1.840498	5.582791
21589.753434	68.052334	35.595495	5.582574
21522.753310	68.054712	31.765366	5.582985
21454.950368	68.057071	24.101007	5.583396
21386.133332	68.059421	16.432719	5.583806

Table E1: Example of precisely estimated range ( $r_m$ ) and azimuth ( $a_m$ ) along with range change ( $dr$ ) and azimuth change ( $da$ ) from master image to slave image.

#### E.4 Enhanced Spectral Diversity

In a few cases, the along-track orbit error (or time tag error) may result in an interferogram having an unacceptable phase mismatch at the burst boundaries. If there is adequate coherence between the reference and repeat SAR images, the phase mismatch can be used to refine the azimuth shift of the repeat image (Prats-Iraola et al. 2012). The phase difference  $\phi$  in the overlap zones can be extracted from a double-difference interferogram.

$$s_{sd} = (s_{u,m} \cdot s_{u,s}^*) \cdot (s_{l,m} \cdot s_{l,s}^*)^* \quad (\text{E3})$$

$$\phi = \arg(s_{sd}) \quad (\text{E4})$$

where, for example,  $s_{u,m}$  is the SLC of the upper portion of the overlap zone for the master. In practice, one computes and filters double difference interferograms for all the pixels in perhaps 8 overlap zones. Then the median phase from all the pixels is

used in equation E1 to calculate a single residual azimuth shift to update the azimuth shift  $da$  in Table E1. The problem with this approach is that it would require adequate coherence between every SAR image and the master or even worse, a re-alignment of every interferometric pair. With accurate orbits and software, we believe this step is largely unnecessary.

## E.5 Elevation Antenna Pattern (EAP) Correction (IPF version change)

The EAP correction was initially introduced by Sentinel-1 Image Processing Facility considering the gain of the EAP. Later in March 2015, as an outcome of S-1A commissioning phase, it was decided to upgrade the S-1 IPF to also correct for the EAP phase. As a consequence, any interferogram with acquisitions processed at times spanning the two different IPF versions will have range varying phase offset. The correction was done in GMTSAR according to the document published by ESA:

<https://sentinel.esa.int/documents/247904/1653440/Sentinel-1-IPF-EAP-Phase-correction>

## E.6 Examples of TOPS Interferogram processing

1. Geometric registration with 6-parameter method: see Figure E4.
2. Geometric registration with point-by-point method: see Figure E5.
3. Enhanced spectral diversity correction: see Figure E6.
4. Elevation antenna pattern (EAP) correction: see Figure E7.
5. Batch processing and 6-parameter circuit analysis: see Table E2.

	$1 \leftarrow 2$	$2 \leftarrow 3$	$3 \leftarrow 1$	Sum
$rshift(c_0)$	-3.82993	-7.6185	11.449	5.7E-04
$rstretch(c_1)$	-6.27437E-05	-1.01554E-04	1.64305E-4	7.3E-09
$a\_stretch\_r(c_2)$	5.19112E-05	-5.70248E-05	5.03074E-06	-8.3E-08
$ashift(c_3)$	12.9332	-0.12195	-12.8113	5.0E-05
$astretch(c_4)$	-5.71073E-06	3.56651E-06	2.14558E-06	1.4E-09
$a\_stretch\_a(c_5)$	3.39592E-06	1.17856E-06	-4.57157E-06	2.9E-09

Table E2: Circuit closure test for 6-parameter alignment. Six parameters are derived each interferogram in the circuit. The sum of the parameters (last column) are 2–3 orders of magnitude smaller than the individual parameters. This excellent closure result implies that processing large stacks of interferograms will be very efficient because once all slave images are geometrically aligned with the master, well aligned interferograms can be formed between any two images.

6. Batch processing and point-by-point circuit analysis: see Figure E8.
7. Example of time series at Cerro Prieto Geothermal Field. To illustrate the utility of the geometric alignment method, we processed 32 SAR images for a region containing the Cerro Prieto Geothermal Field where there is a high subsidence rate associated with extraction of geothermal fluids (Sarychikhina et al. 2011). The baseline versus time plot for these data is shown in Figure E9. All the images were aligned to a single master using the point-to-point method described above. From the 32 images we constructed 138 interferograms as shown in the lines connecting the acquisitions. From this set we illustrate the accuracy of the circuit closure as shown in Figure E10. The sum of the three uncorrected and lightly filtered interferograms is near a constant value. Finally the time series and velocity are shown in Figures E11 and E12.

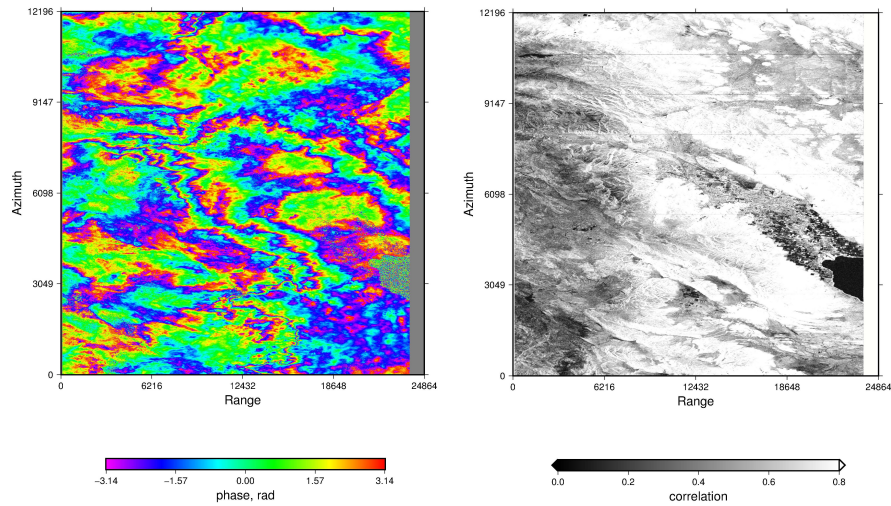


Figure E4: Interferogram and coherence of SW3 of the Southern California pair (20150526-20150607) processed with alignment/registration by 6-parameter affine transformation. The phase mismatch at burst boundaries is no longer visible. There is a slightly lower correlation at the burst boundaries reflecting a slight phase offset.

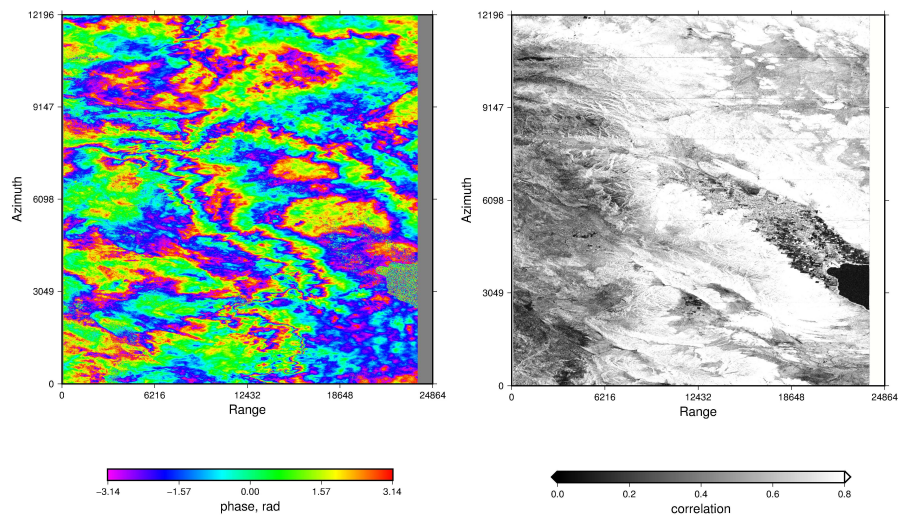


Figure E5: Interferogram and coherence of SW3 of the LA pair (20150526-20150607) processed with point-by-point alignment/registration. The differences between the 6-par method and the PBP method are very small except in cases of long InSAR baseline and high amplitude topography.

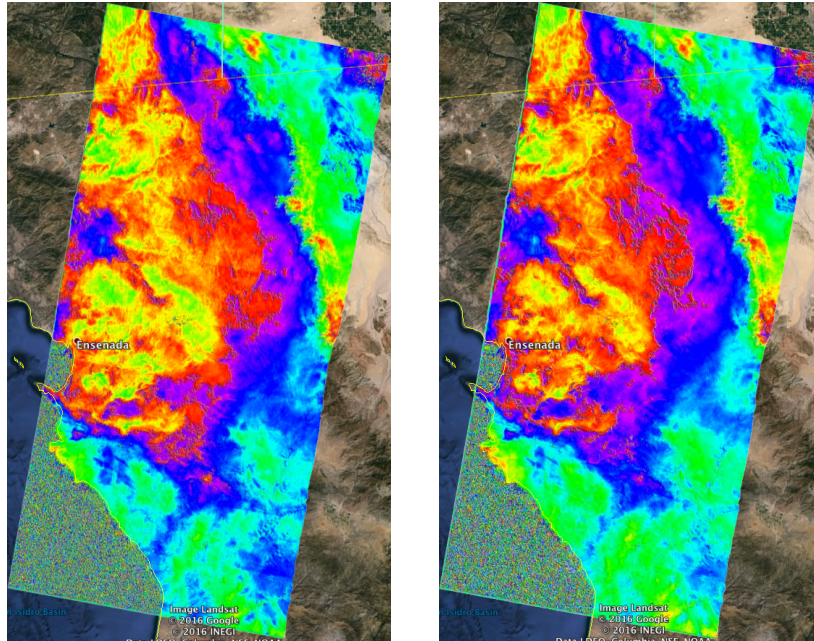


Figure E6: Interferogram without (left) and with(right) enhanced spectral diversity.

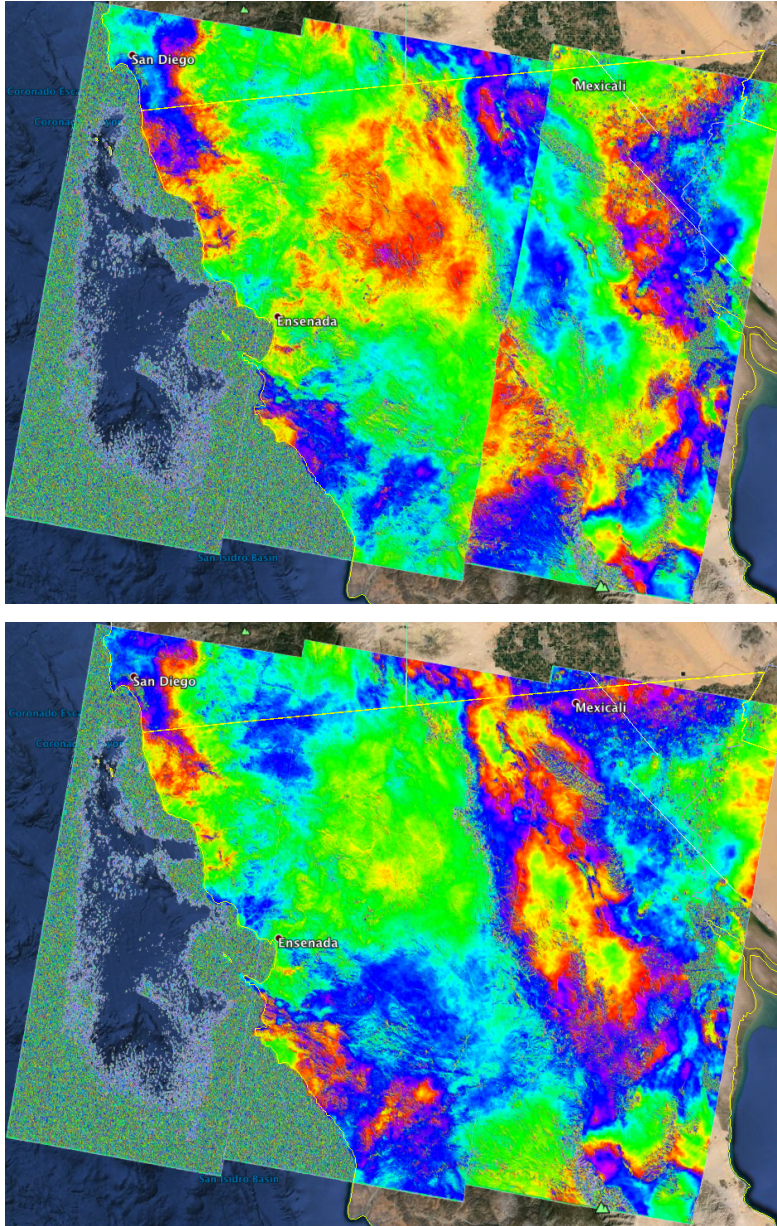


Figure E7: Example of EAP correction (20150226-20150322 over Baja-California). (a) Full 3-subswath interferograms processed without the EAP correction. (b) Full 3 subswath interferograms processed with the EAP correction.

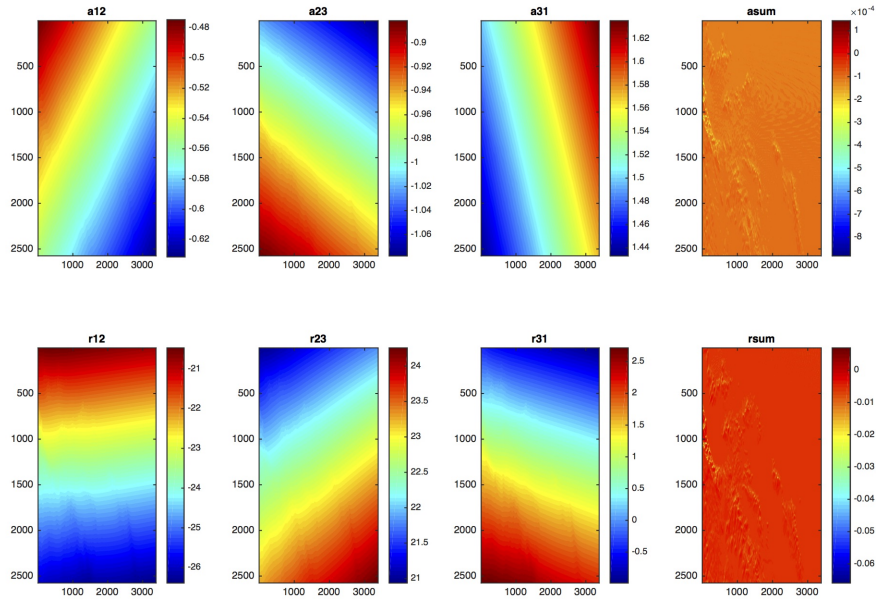


Figure E8: Circuit closure test for point-by-point alignment in the Himalaya area having extreme topography. The figures show the circuit tests for the azimuth grids (upper) and range grids (lower). The grids are very smooth and well approximated by a plane (3 parameters azimuth and 3 parameters range) despite the extreme topography. The sum around the circuit is generally 2–3 orders of magnitude smaller than the original grids. This excellent closure implies that processing large stacks of interferograms will be very efficient because once all slave images are geometrically aligned with the master, well aligned interferograms can be formed between any two images. A time series example is provided below.

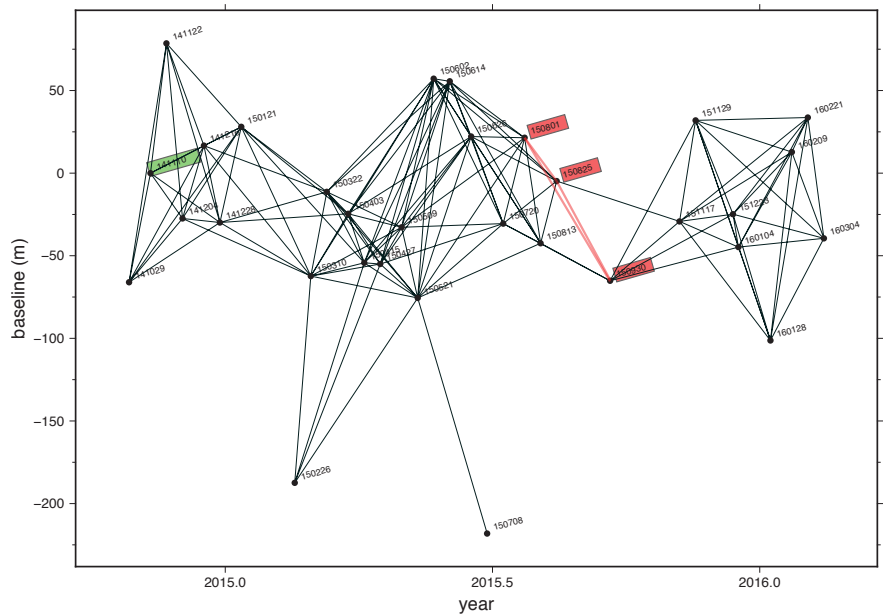


Figure E9: Perpendicular baseline versus time plot for the 32 SAR images over the Cerro Prieto geothermal area. The 31 slave images were all geometrically aligned with the master image (green). After this alignment we formed 138 interferograms without additional alignment. To test circuit closure we selected three interferograms (red).

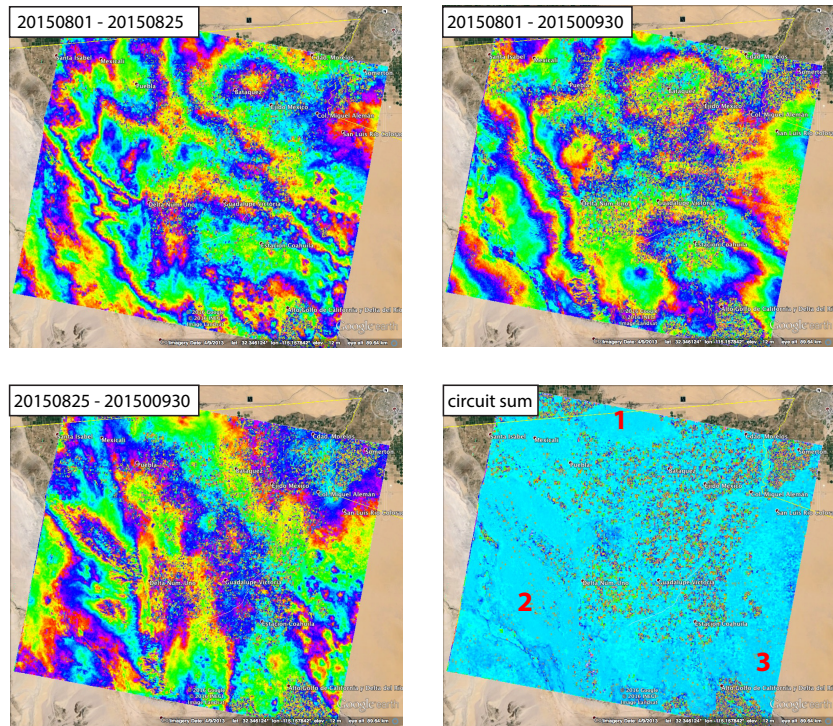


Figure E10: Three of the 138 interferograms were selected to illustrate the accuracy of the circuit closure. Interestingly, the mean value of the closure (sum) is nearly a constant  $-2.49$  mm, but significantly different from zero. The standard deviation of the entire area is  $3.01$  mm but that value is largely affected by decorrelated areas where the phase has considerable noise. By selecting 3 relatively low-noise areas we obtain mean and standard deviations of (1)  $-3.33 \pm 0.51$  mm, (2)  $-3.38 \pm 0.72$  mm, and (3)  $-3.56 \pm 1.00$  mm.

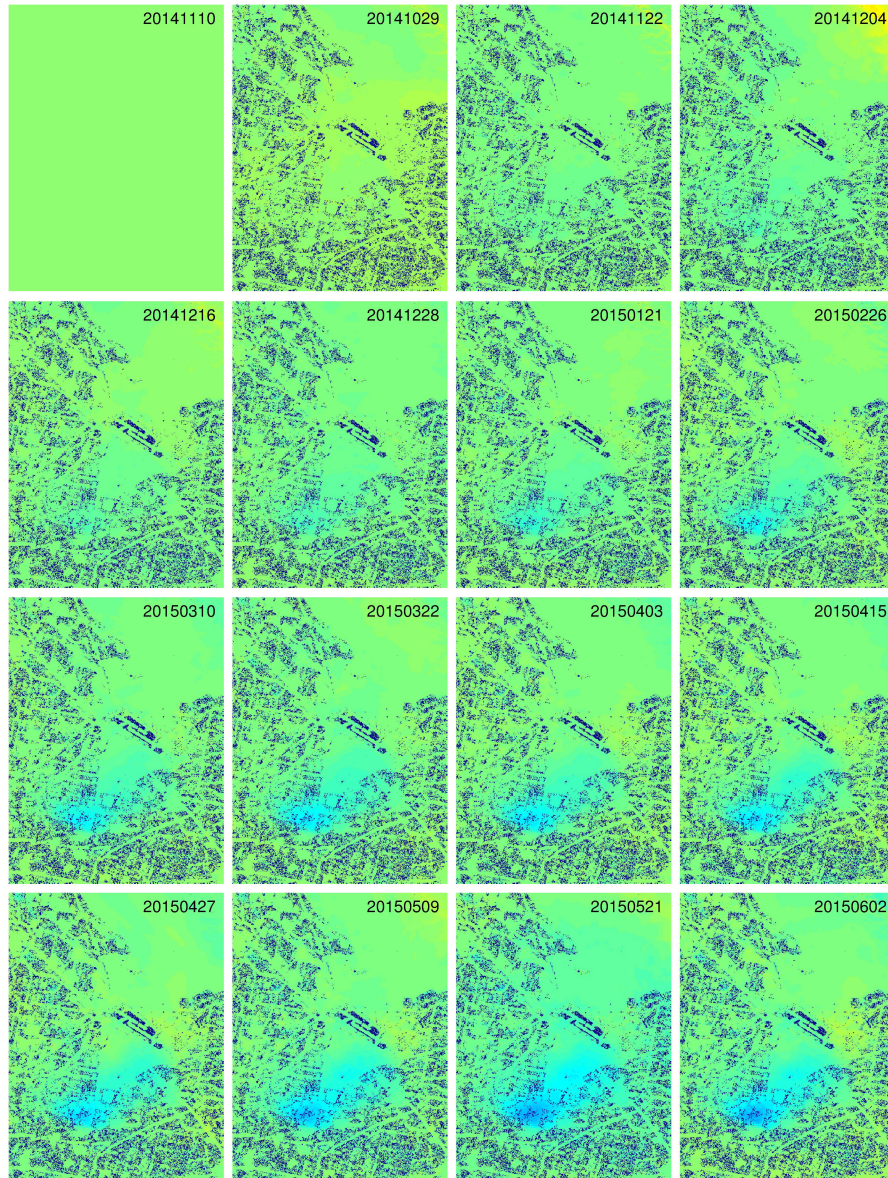


Figure E11: Line of Sight (LOS) time series in radar coordinates. The 32 acquisitions were processed with coherenced-based SBAS method (Tong and Schmidt 2016). Color map is jet  $[-200\ 200]$  mm, with red denoting ground moving toward radar and blue denoting ground moving away from radar (subsiding).

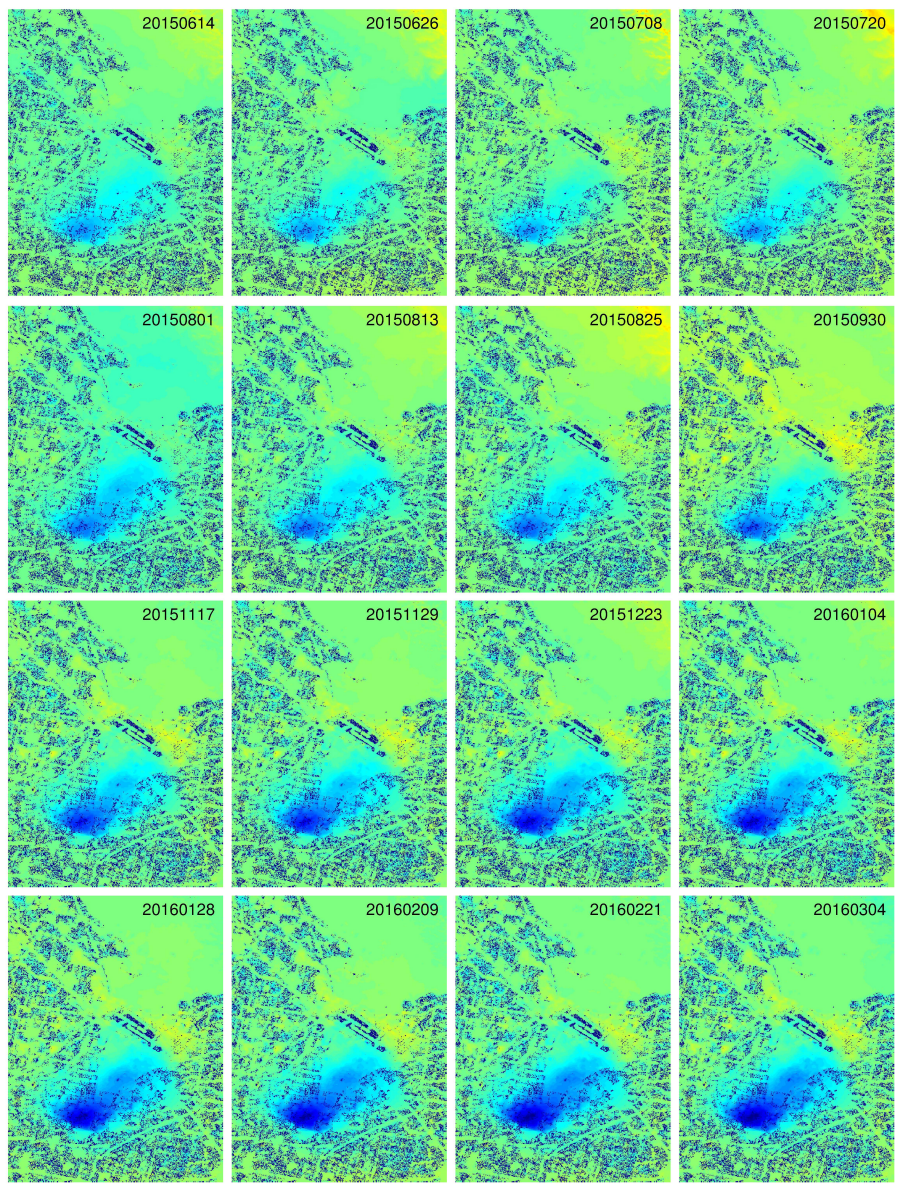


Figure E11: continued.

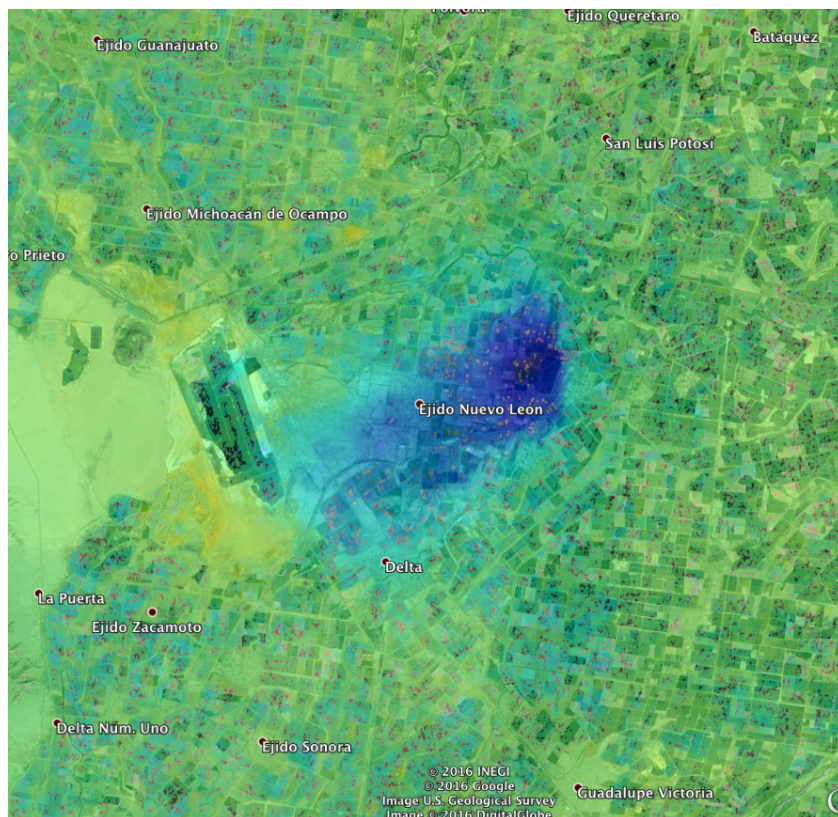


Figure E12: Line of sight velocity (mostly vertical) in geocoordinates. Color scale is  $[-145 \ 145]$  mm.

## E.7 Processing setup and commands:

1. Gather SLC (SAFE) data: Download Sentinel 1 data from the Sentinel Data Hub (<https://scihub.copernicus.eu/dhus/>) or from the Alaska Satellite Facility (<https://vertex.daac.asf.alaska.edu/>). Another option is to search from SARA GUI (<http://web-services.unavco.org/brokered/ssara/gui2.0>), from where your search will be redirected to the ASF data archive.
2. Gather more precise orbits: Precise orbits can be found at ESA ([https://qc.sentinel1.eo.esa.int/aux\\_poeorb/](https://qc.sentinel1.eo.esa.int/aux_poeorb/)) or at UNAVCO ([https://www.unavco.org/data/imaging/sar/lts1/winsar/slqc/aux\\_poeorb/](https://www.unavco.org/data/imaging/sar/lts1/winsar/slqc/aux_poeorb/)).
3. Construct DEM: Digital Elevation Models can be generated with the following link (<http://topex.ucsd.edu/gmtsar/demgen/>).

4. Run `align_tops.csh` (PBP or 6-par) or `preproc_batch_tops.csh` (for time series)
  - (a) Run subswath by subswath. For each subswath, prepare the `*.xml` and `*.tiff` files and put them in the raw folder. Download the required orbit files and also put them in the raw folder.
  - (b) If you intend to correct for Elevation Antenna Pattern (recommended if any interferogram is generated with acquisitions having different IPF version), please concatenate the `manifest.safe`. (It comes with the data, and contains the IPF version.) First line needs to be *deleted!* (Not a typical xml file.) and the `s1a-aux-cal.xml`. (Aux-file needed for computing EAP. Installed with GMTSAR at `preproc/S1A_preproc/src_tops`) to the xml files corresponding to each subswath.
  - (c) Run `align_tops.csh` for patch to patch processing. If Enhanced Spectral Diversity is needed, run `align_tops_esd.csh` instead.
  - (d) For batch processing, link the DEM file from the topo folder to the raw folder and prepare the input file for `preproc_batch_tops.csh`. The format is as follows:
 

```
s1a-DATE1-TIME1...001:s1a-DATE1-TIME2...001:...:orbit.EOF
```

Example:

```
s1a-iw1-slc-vv-20141110t134325-20141110t134351-003220-003b77-001:s1a-iw1-slc-vv-20141110t134350-20141110t134415-003220-003b77-001:s1a-iw1-slc-vv-20141110t134415-20141110t134427-003220-003b77-001:S1A_OPER_AUX_POEORB_OPOD.20141201T123710_V20141109T225944_20141111T005944.EOF
```

```
s1a-iw1-slc-vv-20141204t134325-20141204t134350-003570-004361-001:s1a-iw1-slc-vv-20141204t134349-20141204t134415-003570-004361-001:s1a-iw1-slc-vv-20141204t134414-20141204t134426-003570-004361-001:S1A_OPER_AUX_POEORB_OPOD.20141225T124157_V20141203T225944_20141205T005944.EOF
```

Note for each line, the `TIME1`, `TIME2`,... should be in chronological order.
  - (e) Run `preproc_batch_tops.csh` in mode 1 to get the `baseline_time` plot. Select the super-master and move it to the top of the input file. Then re-run the `preproc_batch_tops.csh` with mode 2 to create PRMs, LEDs and SLCs. If Enhanced Spectral Diversity is needed, run `preproc_batch_tops_esd.csh` instead.
5. Run `p2p_S1A_TOPS.csh` (PBP or 6-par) or `intf_tops.csh` (for time series)
  - (a) For patch to patch processing, prepare the config file (at `/gmtsar/csh`).
  - (b) For batch processing, prepare the `batch_tops.config`. Remember to set the `master_image`. Then create an input file listing all the interferometric pairs. The format is as follows: `master_image_stem:slave_image_stem` Example:
 

```
S1A20150628_ALL_F1:S1A20150720_ALL_F1 S1A20150720_ALL_F1:S1A20150809_ALL_F1
```
  - (c) Run `intf_tops.csh`.
6. To create time series, run `sbas`.

Examples of Sentinel-1 processing setups can be downloaded at <http://topex.ucsd.edu/gmtsar/downloads>

## References

- Fernandez, J. et al. (2015). “Copernicus POD Operations- Orbital Accuracy of Sentinel-1A and Sentinel-2A”. In: *International Symposium on Space Flight Dynamics* 4.2. An optional note, pp. 201–213.
- Meta, A. et al. (2010). “TOPS imaging with TerraSAR-X: Mode design and performance analysis”. In: *Geoscience and Remote Sensing, IEEE Transactions on* 48.2, pp. 759–769.
- Miranda, N. (2015). *Definition of the TOP SSLC deramping function for products generated by the S-1 IPF*. Tech. rep. COPE-GSEG-EOPG-TN-14- 0025. European Space Agency.
- Mittermayer, Josef et al. (2010). “TOPS Sentinel-1 and TerraSAR-X processor comparison based on simulated data.” In: *Synthetic Aperture Radar (EUSAR), 2010 8th European Conference on*. VDE.
- Prats-Iraola, P. et al. (2012). “TOPS interferometry with TerraSAR-X. Geoscience and Remote Sensing”. In: *Geoscience and Remote Sensing, IEEE Transactions on* 50.8, pp. 3179–3188.
- Sansosti, E. et al. (2006). “Geometrical SAR image registration.” In: *IEEE Transactions on Geoscience and Remote Sensing* 44.10, p. 2861.
- Sarychikhina, O. et al. (2011). “Land subsidence in the Cerro Prieto Geothermal Field, Baja California, Mexico, from 1994 to 2005: An integrated analysis of DInSAR, leveling and geological data”. In: *Journal of Volcanology and Geothermal Research* 204.1, pp. 76–90.
- Tong, X. and D. Schmidt (2016). “Active movement of the Cascade Landslide Complex in Washington from a coherence-based InSAR time series method”. In: *Remote Sensing of Environment, in review*.
- Xu, Xiaohua et al. (2017). “Tectonic and Anthropogenic Deformation at the Cerro Prieto Geothermal Step-Over Revealed by Sentinel-1A InSAR”. In: *IEEE Transactions on Geoscience and Remote Sensing*.

## E.8 Problems

1. Derive equation (E1).
2. Give two reasons why the standard cross-correlation imaging matching approach is not adequate for TOPS-mode data?
3. Why must the bursts be deramped prior to sinc interpolation?
4. Why does a 6-parameter affine transformation model work well when the interferometric baseline is small and the topography has low relief?

## F Geolocation accuracy for Pinon corner reflectors

Precise orbital information can be used to map every point on the surface of the earth (lon, lat, topography) into the range and azimuth coordinates of the radar. If the SAR image is focused at zero Doppler then the range coordinate of the mapping is simply the minimum range and the azimuth coordinate is the time of the minimum range. If the radar image was focused at a Doppler centroid other than zero, then equations 4 and 5 of the main document are the two corrections needed to transform from geographic to radar coordinates.

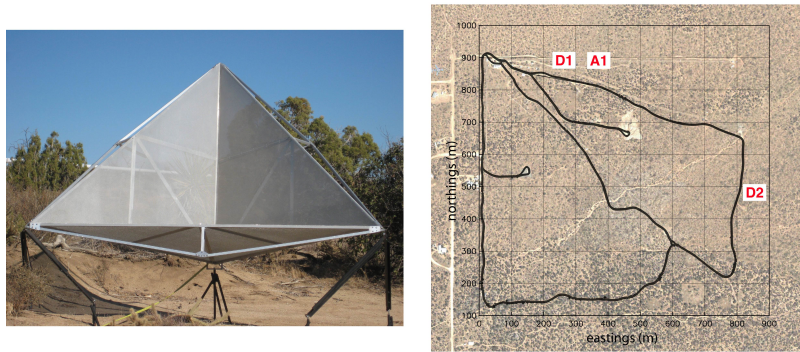


Figure F1: (Left) one of the 2.4 m radar corner reflectors at Pinon Flat Observatory installed in 1998. (Right) Satellite image of the Pinon Flat Observatory. This arid region at an elevation of 1200 m is relatively flat with a surface of decomposed granite sparsely covered by bush and grass. Three radar corner reflectors are oriented to reflect energy from ascending (A1—ALOS) and descending (D1 and D2—ERS2, ENVISAT, ALOS-2 ScanSAR) passes.

	Position			Orientation	
	<i>lat</i>	<i>lon</i>	<i>height</i>	<i>elevation</i>	<i>azimuth</i>
<i>A1</i>	33.612246	-116.456768	1258.990	39°	257.5°
<i>D1</i>	33.612253	-116.457893	1257.544	39°	102.5°
<i>D2</i>	33.607373	-116.451836	1254.537	39°	102.5°

Table F1: Coordinates of Radar Reflectors

Latitude and longitude in decimal degrees and elevation in meters relative to the WGS-84 coordinate system and ellipsoid. The survey point is the apex (lowest corner) of each reflector.

We tested the combined accuracy of the geometric model, the satellite orbits, and the range and Doppler measurements, using 3 radar corner reflectors installed at Pinon Flat Observatory (Figure F1 and Table F1). The positions of the corner reflectors are accurately measured using GPS. The orbits for ERS2, ENVISAT, and ALOS/ALOS-2 are determined to an accuracy of better than 20 cm and perhaps as good as 5 cm. The near range and timing of the satellite are provided with the data and should have sub-meter accuracy. Using this information one can predict the range and azimuth pixel where the bright radar reflection should appear in the image. We then focus each SAR image and locate the position of the radar reflectors as bright spots. ALOS-2 ScanSAR product comes as Single-Look-Complex thus it is directly converted to amplitude images. The measurement is done by eye to an accuracy of about 1 pixel in range and about 2 pixels in azimuth. The difference between the image-based coordinate and the orbital-based coordinate provides an estimate of the overall accuracy of the system.

We performed this analysis on all ERS2 data collected after the radar reflectors were installed having Doppler centroid less than 1/2 the PRF (36 points), as well as all available ENVISAT (10 points), ALOS (27 points) and ALOS-2 ScanSAR (12 points) data. The results for ERS2, ENVISAT, ALOS and ALOS-2 ScanSAR are provided in Tables F2, F3, F4 and F5, respectively. In the case of ERS2, the mean difference and rms deviation in range is  $-1.8$  and  $0.3$  pixels respectively while the mean and rms differences in azimuth are  $3.7$  and  $2.6$  pixels respectively. The mean differences are statistically significant and this bias should eventually be included in the orbital software. ENVISAT has much larger mean differences in range and azimuth of  $8.4$  and  $4$ , respectively but the rms differences are small ( $0.2$  and  $2.2$  respectively) so these biases have been included in the software. The ALOS mean differences are relatively small in both range ( $-1.2 \pm 0.6$ ) and azimuth ( $0.6 \pm 1.1$ ) so no biases have been included in the software. Finally the ALOS-2 ScanSAR mean differences are quite small in range ( $0.97 \pm 0.47$ ) and the azimuth is essentially zero ( $-4E - 07 \pm 0.67$ ) so no biases have been included in the software.

One significant finding of the ALOS-2 ScanSAR analysis is that the images show 7 stacked reflectors instead of one (Table F5). This is caused by a combined effect of lower resolution along azimuth and the diffraction from periodic observation. The multiple bright spots from a single reflector can result in errors in image alignment because the cross-correlation solution may lock on to one of the secondary peaks. To

avoid locking on to the wrong peak, we implemented a filter in the alignment step to band-pass the cross-correlation results ( $\pm 3$  pixels from the major peak). This approach stabilized the image alignment to lock onto the primary peak.

Overall we find that after correcting for a range bias in ENVISAT, the range and azimuth coordinates based only on the orbital information are accurate to better than 1 pixel in range and 2 pixels in azimuth consistent with the uncertainties in picking the bright locations in the images. The ALOS-2 ScanSAR has multi-peak issue that was fixed with a simple filter. Based on these analysis we conclude that ground control is not needed for InSAR processing and orbital-based image alignment should be accurate to better than about 15 m in range and 10 m in azimuth.

Name	Doppler	Ri-Ro	Ai-Ao
e2.22025_2925	58.3	-1.7	3.0
e2.22025_2925	58.3	-1.9	2.9
e2.22526_2925	81.2	-1.5	5.2
e2.22526_2925	81.2	-2.3	5.1
e2.23027_2925	17.1	-0.9	7.2
e2.23027_2925	17.1	-2.0	7.2
e2.23528_2925	78.3	-1.7	-0.1
e2.23528_2925	78.3	-1.9	-0.1
e2.24029_2925	75.4	-2.2	7.6
e2.24029_2925	75.4	-1.9	7.6
e2.24530_2925	141.4	-1.8	2.6
e2.24530_2925	141.4	-1.6	2.6
e2.25532_2925	575.5	-1.5	6.1
e2.25532_2925	575.5	-1.8	2.6
e2.26033_2925	42.4	-2.1	3.3
e2.26033_2925	42.4	-1.9	4.8
e2.27035_2925	-286.5	-1.9	3.5
e2.27035_2925	-286.5	-1.8	3.6
e2.27536_2925	-295.8	-1.9	7.1
e2.27536_2925	-295.8	-2.0	2.2
e2.28037_2925	-75.7	-1.7	4.3
e2.28037_2925	-75.7	-1.5	4.3
e2.28538_2925	-1.7	-1.7	2.2
e2.28538_2925	-1.7	-2.0	2.2
e2.29039_2925	-210.2	-1.8	3.8
e2.29039_2925	-210.2	-1.6	3.3
e2.33047_2925	-625.3	-2.1	-3.6
e2.33047_2925	-625.3	-1.8	-3.5
e2.55592_2925	530.8	-1.9	3.6
e2.55592_2925	530.8	-1.9	3.5
e2.58598_2925	-203.8	2.3	2.4
e2.58598_2925	-203.8	-2.0	1.9
e2.59099_2925	-95.8	-1.2	3.3
e2.59099_2925	-95.8	-2.0	3.3
e2.61103_2925	-83.9	-1.7	4.2
e2.61103_2925	-83.9	-1.4	4.2
<b>mean</b>		<b>- 1.8</b>	<b>3.7</b>
<b>rms</b>		<b>0.3</b>	<b>2.6</b>

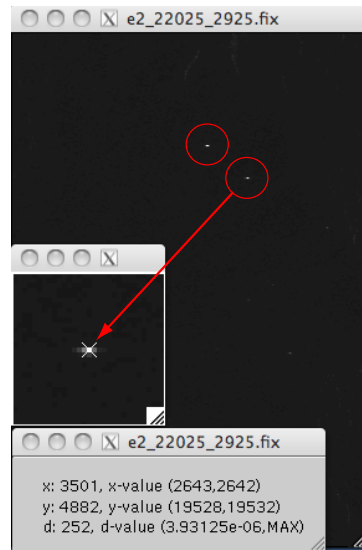
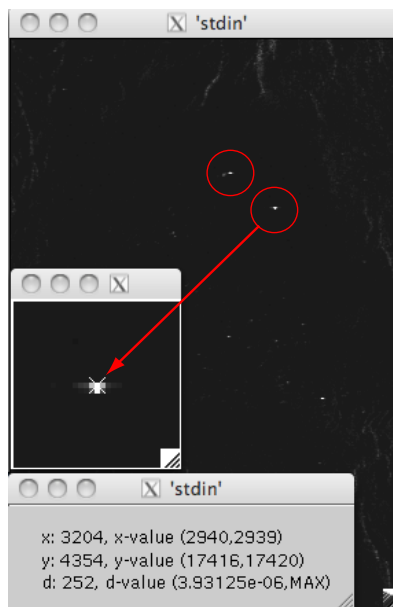


Table F2: Comparison between ERS2 image and orbit for Pinon corner reflectors D1 and D2 (right).

Name	Doppler	Ri-Ro	Ai-Ao
ENV1_2_127_2925_07195	150.8	-0.1	2.7
ENV1_2_127_2925_07195	150.8	0.1	0.7
ENV1_2_127_2925_12706	93.2	0.2	-1.9
ENV1_2_127_2925_12706	93.2	-0.2	-3.9
ENV1_2_127_2925_13207	93.6	0.1	1.3
ENV1_2_127_2925_13207	93.6	0.2	2.3
ENV1_2_127_2925_38758	114.4	0.1	2.5
ENV1_2_127_2925_38758	114.4	-0.2	0.4
ENV1_2_127_2925_44770	114.1	-0.3	2.3
ENV1_2_127_2925_44770	114.1	-0.2	2.3
<b>mean</b>		<b>0.0</b>	<b>0.9</b>
<b>rms</b>		<b>0.2</b>	<b>2.2</b>

Table F3: Comparison between ENVISAT image and orbit for Pinon corner reflectors D1 and D2 (below).

Note a bias of 8.4 in range and 4 in azimuth was added to the orbital range, azimuth coordinates.



Name	Ri-Ro	Ai-Ao
ALPSRP022200660	-2.0	0.0
ALPSRP028910660	-2.1	0.0
ALPSRP035620660	-0.1	0.8
ALPSRP042330660	-2.3	2.2
ALPSRP049040660	-1.7	1.0
ALPSRP055750660	-1.9	0.8
ALPSRP062460660	-1.7	1.0
ALPSRP075880660	-0.7	2.0
ALPSRP082590660	-0.6	0.0
ALPSRP089300660	-0.6	-1.0
ALPSRP096010660	-1.0	1.0
ALPSRP109430660	-0.9	2.0
ALPSRP116140660	-0.5	0.0
ALPSRP122850660	-0.7	2.0
ALPSRP129560660	-1.1	2.0
ALPSRP136270660	-1.1	0.0
ALPSRP142980660	-1.5	0.0
ALPSRP149690660	-1.7	-2.0
ALPSRP156400660	-1.1	-1.0
ALPSRP163110660	-0.9	0.0
ALPSRP183240660	-1.3	1.0
ALPSRP189950660	-1.1	0.0
ALPSRP196660660	-1.1	0.0
ALPSRP210080660	-2.5	1.0
ALPSRP223500660	-1.8	1.0
ALPSRP230210660	-0.3	2.0
ALPSRP236920660	-1.0	0.0
<b>mean</b>	<b>-1.2</b>	<b>0.6</b>
<b>rms</b>	<b>0.6</b>	<b>1.1</b>

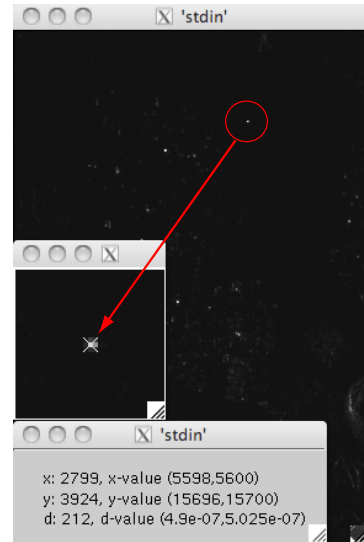
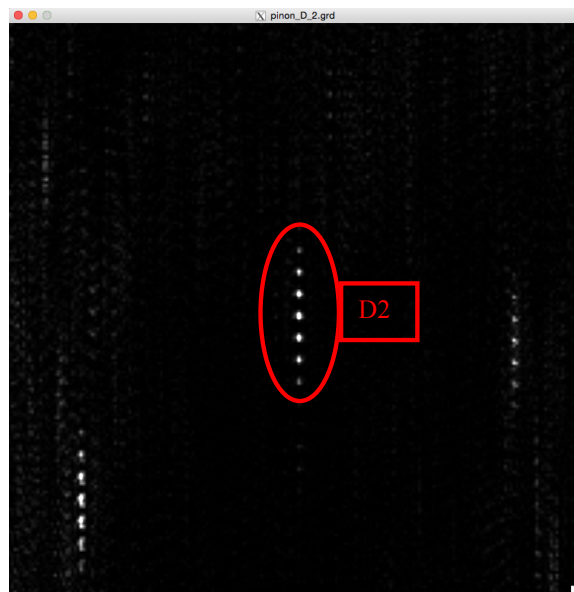


Table F4: Comparison between ALOS image and orbit for Pinon corner reflectors D1 and D2 (right).

Name	CR	Ri-Ro(m)	Ai-Ao(m)
ALOS2053922950-150523-WBDR1.1__D-F5	D1	11.78	-1.24
ALOS2053922950-150523-WBDR1.1__D-F5	D2	12.16	-1.24
ALOS2060132950-150704-WBDR1.1__D-F5	D1	4.02	1.24
ALOS2060132950-150704-WBDR1.1__D-F5	D2	4.43	3.72
ALOS2076692950-151024-WBDR1.1__D-F5	D1	14.43	-1.24
ALOS2076692950-151024-WBDR1.1__D-F5	D2	6.28	-6.20
ALOS2064272950-150801-WBDR1.1__D-F5	D1	6.67	-1.24
ALOS2064272950-150801-WBDR1.1__D-F5	D2	7.05	-1.24
ALOS2070482950-150912-WBDR1.1__D-F5	D1	3.64	1.24
ALOS2070482950-150912-WBDR1.1__D-F5	D2	12.64	1.24
ALOS2060132950-150704-WBDR1.1__D-F5	D1	12.60	1.24
ALOS2060132950-150704-WBDR1.1__D-F5	D2	4.435	3.72
<b>mean</b>		<b>8.348*</b>	<b>-4.13E-07</b>
<b>rms</b>		<b>4.048<sup>†</sup></b>	<b>2.67<sup>‡</sup></b>

Table F5: Comparison Between ALOS-2 ScanSAR image and orbit for Pinon reflectors D1 and D2.

\* 0.97 pxl † 0.47 pxl ‡ 0.67 pxl



## G Installation of GMTSAR

### Instructions

The most up-to-date installations instructions can be found in the GMT5SAR WIKI.

<http://gmt.soest.hawaii.edu/projects/gmt5sar/wiki>

After installing, go back to the original GMTSAR page and download example data sets for testing. One can also construct the dem.grd for your area at this page.

<http://topex.ucsd.edu/gmtsar>

### Prerequisites

- C-compiler or Xcode (Mac)
- TC shell or C shell or bash
- More than 4 GB of memory. The code will run with less memory but could be extremely slow due to paging of memory in *esarp*.

### Feedback

Feedback—*bad* or *good*—is essential for making improvements. Send to:

David Sandwell (dsandwell@ucsd.edu)  
Rob Mellors (mellors1@llnl.gov)  
Xiaopeng Tong (ttxpp84@outlook.com)  
Xiaohua Xu (xix016@ucsd.edu)  
Matt Wei (matt-wei@uri.edu)  
Paul Wessel (pwessel@hawaii.edu)